

INFORMATION TO USERS

This manuscript has been reproduced from the microfilm master. UMI films the text directly from the original or copy submitted. Thus, some thesis and dissertation copies are in typewriter face, while others may be from any type of computer printer.

The quality of this reproduction is dependent upon the quality of the copy submitted. Broken or indistinct print, colored or poor quality illustrations and photographs, print bleedthrough, substandard margins, and improper alignment can adversely affect reproduction.

In the unlikely event that the author did not send UMI a complete manuscript and there are missing pages, these will be noted. Also, if unauthorized copyright material had to be removed, a note will indicate the deletion.

Oversize materials (e.g., maps, drawings, charts) are reproduced by sectioning the original, beginning at the upper left-hand corner and continuing from left to right in equal sections with small overlaps.

Photographs included in the original manuscript have been reproduced xerographically in this copy. Higher quality 6" x 9" black and white photographic prints are available for any photographs or illustrations appearing in this copy for an additional charge. Contact UMI directly to order.

ProQuest Information and Learning
300 North Zeeb Road, Ann Arbor, MI 48106-1346 USA
800-521-0600

UMI[®]

ENTROPICALLY DRIVEN INTERACTION BETWEEN COLLOIDS AND
THEIR SELF-ASSEMBLY

Keng-hui Lin

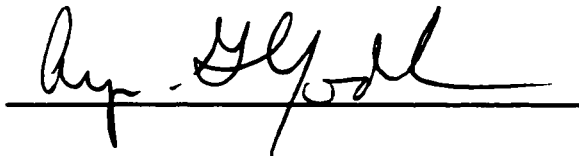
A DISSERTATION

in

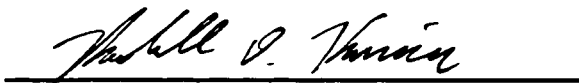
PHYSICS AND ASTRONOMY

Presented to the Faculties of the University of Pennsylvania in Partial Fulfillment of
the Requirements for the Degree of Doctor of Philosophy

2002

A handwritten signature in black ink, appearing to read "A. G. G. G.", written above a solid horizontal line.

Supervisor of Dissertation

A handwritten signature in black ink, appearing to read "Michael S. Thoma", written above a solid horizontal line.

Graduate Group Chairperson

UMI Number: 3054973

**Copyright 2002 by
Lin, Keng-hui**

All rights reserved.

UMI[®]

UMI Microform 3054973

**Copyright 2002 by ProQuest Information and Learning Company.
All rights reserved. This microform edition is protected against
unauthorized copying under Title 17, United States Code.**

**ProQuest Information and Learning Company
300 North Zeeb Road
P.O. Box 1346
Ann Arbor, MI 48106-1346**

COPYRIGHT

Keng-hui Lin

2002

To Ma, Hsiu-lien Chen

ACKNOWLEDGEMENTS

Throughout the course my graduate school, I have benefitted from people around me in various ways.

First and foremost, I can not have a better advisor than Arjun Yodh. He has provided a resourceful environment to carry out research and given me endless support and faith. The discussion on science is always stimulating and challenging. He encouraged me to work on different research projects to be a versatile researcher. He gave me many opportunities to attend various workshops and conferences. He helped me be good at giving talks and writing with unexhausted patience. Most important of all, he makes me believe in myself.

John Crocker, whom I called my underground advisor. has taught me how to think about science the most. He challenged me to have higher standard in research and gave me good leads to start with. Discussion with him is always enlightening and exciting. I shall always remember the night we brainstormed out the grating ideas which has changed the course of my research. His senior experiences provide me invaluable lessons of having a successful scientific career.

I benefitted enormously from Dave Weitz group even after his moving to Harvard. The wide spectrum of exciting research projects broaden my perspective in soft condensed matter physics and help me grasp the basics of light scattering, rheology, emulsions, and etc. The companionship from his group members – Eric Weeks. Sophie

Pautot, Vikram Prasad, Urs Gasser, Megan Velatine, Suliana Manley, Phil Segre... stimulates me to be a better scientist. Eric teaches me cool tricks on computer and gives me valuable advice on how to cope with stressful events. Sophie introduces me to the surfactant and interfacial world. Her strong character teaches me to feel comfortable about being assertive and aggressive. Vikram keeps up with papers well and I often learn something new from him. I have never gotten over the sense of loss after their leaving.

Of course. I got a lot of help and support from the group members – Tony Dinsmore, Ritu Verma, Joe Culver, David Cook, Daniel Chen, Mohammad Islam, Ahmed Sinan, Zvonimir Dogic, Mateusz Bryning, Jian Zhang, Regina Choe, Turgut Durdur, and Hsin-Wen Wang. I thank them for putting up with my inconsiderate habits in the lab and being supportive when I am in need. Mohammad's careful maintenance on microscope room and Dan's patience to deal with computer systems make the research more smoothly. I also thank excellent undergrads – Andrew Levitt, Josh Gruber, Evan Hohlfeld, and Ariel Michaelman whom I had fun to work with. They taught me how to be a supervisor and confirmed my interests to become a professor.

I have learned a great deal of physics “in equations” by talking to Penn theorists – Tom Lubensky, Randy Kamien, Phil Nelson, Alex Levine, Primoz Zihlerl, and Andy Lau. I am especially grateful for Andy who has taught me a lot of of statistical mechanics. We have a great time collaborating, and his help has made the last few

most stressful months of thesis writing go by smoothly.

The experiments would be impossible without good experimental systems. I would not have two wonderful experimental systems without Andrew Schofield and Ana Zeri. Whenever I ask Andrew for help, he replies fast and provide useful information or materials. Ana is patient to teach me basic microbiology lab techniques. I also thank Dr. Opella's group for letting me use his lab resource for fd growth. When I tried out the imprint technique, I received helpful guidance from Deng Tao in George Whitesides group and Larry Zhang in Steve Chou's group. I am also thankful for Ahmed's creative trial on thermoplastic slabs which improved the manufacture of waffle templates.

I am very lucky to have interactions with many research groups who enrich the research experiences. Discussion with Carlos Marques gave me insight in rod interaction measurement. Peter Mach showed me the beauty of liquid crystal and kindly put me as a co-author for his quality work. Charlie Johnson and his group gave me exposure to hard condensed matter physics. George Watson patiently lead me through the e-beam lithography process. Dennis and Bohdana Discher taught me about vesicles. Paul Janmey and his fun and friendly group gave me better grasp of biochemistry vocabulary.

Penn Physics Department has been a friendly environment for graduate studies. I have a wonderful class who helped me through the class homework and the quali-

fication exam. Noam Mohr, Patrick McDonald, Marko Radosavljevic, and Dr. Beth Mark whom I met here are good companies and supportive. The business office is very efficient and take care of the hassle of orders well.

I am appreciative for many good friends from Taiwan – Jih-Chiang Tsai, Shin-Shan Eiko Yu, Chih-hsuan Lin, Ying-Jer Kao, Cheng Chin. Ru-Fang Yeh, Chengshan Chin. Chih-hsiang Cheng, Ching-ling Teng, Ker-Jar Song, Chung-Yu Mou, and so on. The connection between us gives me a strong foundation to establish a career in a foreign country.

Finally I would not make it through without the support from my family. I especially owe it to my mom who teaches me to be passionate and persistent in life. I dedicate the thesis to her.

ABSTRACT

ENTROPICALLY DRIVEN INTERACTION BETWEEN COLLOIDS AND THEIR SELF-ASSEMBLY

Keng-hui Lin

Arjun G. Yodh

We have made the first direct measurements of entropic interactions of colloidal spheres in suspensions of rods (fd virus). We investigate the influence of sphere size, rod concentration, and ionic strength on these interactions. Although the results compare favorably with a recent calculation, small discrepancies reveal entropic effects due to rod flexibility. Fits to the data with a bent rod model were excellent, provided we used the persistence length less than $1\ \mu\text{m}$, smaller than the commonly reported value of $2.2\ \mu\text{m}$ for fd-virus. At high salt concentrations, the potential turned repulsive as a result of viral adsorption on the spheres and viral bridging between the spheres.

We also investigated the self-assembly of colloidal spheres on periodically patterned templates. The surface potentials and the surface phases were produced entropically by the presence of non-adsorbing polymers in suspension. A rich variety of two-dimensional fluid- and solid-like phases were observed to form on template potentials with both one- and two-dimensional symmetry. The same methodology was then used to nucleate an oriented single FCC crystal more than 30 layer thick on a commensurate substrate. We observed surface-induced freezing of the hard sphere

fluid due to the patterned surface of expanding FCC(100) lattice at volume fraction lower than bulk freezing point 54.5%. The bulk osmotic pressure of hard sphere determine the phases above the patterned substrate. The commensurate-incommensurate transitions occurs as the system osmotic pressure increases. At very high osmotic pressure, the system exhibits random hexagonal packed structures despite of underlying square template structures. The template approach provides a new route for directed self-assembly of novel mesoscopic structures.

Contents

1	Introduction	1
2	Theory of Entropic Driven Colloidal Systems	8
2.1	Rod Depletion Interaction between Two Plates	9
2.2	Derjaguin Approximation	14
2.3	Depletion Interaction Due to Spheres and Disks	15
2.4	The YJM Model	18
2.5	Bent Rod Approximation	21
2.6	Equilibrium Phase Behaviors	25
2.7	Hard Sphere System	26
2.8	Sphere/Polymer Mixtures	31
2.9	Charged Sphere Systems	32
2.10	Correlation Function and Structure Function	33
2.11	Bond-Orientational Order	37
2.12	Colloidal Suspensions in Confined Geometries	42

2.13	Surface Freezing On Patterned Substrates	44
2.14	Roughness	48
2.15	Commensurate-Incommensurate Transitions	51
3	Experimental Methods	53
3.1	Polystyrene Spheres	53
3.2	Silica Spheres	55
3.3	Polymethylmethacrylate Spheres	55
3.3.1	Fluorescence Labelled PMMA Particles	56
3.3.2	Solvents for PMMA particles	58
3.4	Template-Directed Colloidal Assembly	63
3.4.1	Imprint with Gratings	65
3.4.2	The Wetting of Particles onto Substrates	71
3.5	Chambers	73
3.6	Optical Microscopy	74
3.7	Optical Tweezers and Interaction Measurements	79
3.7.1	Optical Line Scanned Tweezers	81
3.8	ϕ d Bacteriophage	86
3.8.1	ϕ d Production and Purification	88
3.9	Physical Dimensions of filamentous bacteriophage	91
3.9.1	Electron Microscopy	91

3.9.2	Dynamic Light Scattering	93
3.9.3	Isotropic and Cholesteric Transition	96
3.9.4	Summary on the Physical Dimensions of fd	96
4	Colloidal Interaction in Rod-like Molecule solutions	98
4.1	AO sphere, Derjaguin, and YJM models	99
4.2	Results and Modified YJM models	101
4.2.1	Bent Rod Theory	107
4.3	Salt Concentration in Buffer	114
4.4	Sticky Rods on the Spheres	115
4.5	Measurement at Higher Concentration	117
4.6	Conclusion	118
5	Entropically Driven Colloidal Crystallization on Patterned Surfaces	120
5.1	Depletion Interaction and Surface Structure	121
5.2	Sample Preparation	123
5.3	Line Grating Templates	124
5.4	Crossed Gratings	136
5.5	3D assembly	137
5.6	Expanded FCC(100) Lattice	137
5.7	Conclusion	143

6 Conclusion and Future Work	150
A Wormlike Chain Model	156

List of Figures

2.1 (a) A rod near a hard wall with one end at distance z . The rotation is restricted when $z < L$ and the angle between the rod and the normal to the wall is less than $\cos^{-1} \frac{z}{L}$ is unavailable. (b) A rod between two parallel hard walls with separation h 10

2.2 (a) The number density profile of a dilute rigid rod suspension from a flat wall. The depletion interaction between two plates in rod suspensions. The hatched region with thickness $L/2$ is the depletion zone where a rod loses the rotational degrees of freedom when its center is in the region. (b) Plates separation h is larger than the rod length L . The number density inside plates is the same as outside; therefore, the osmotic pressure on both sides are balanced. (c) when $h < L$: the black region is the overlapped depletion zone. The number density outside plates is larger than inside; therefore the osmotic pressure exerted by rods inducing an attraction between plates. 12

2.3 Schematic illustration that shows how the interaction between spheres may be calculated from the interaction between flat plates 15

2.4 (a) The depletion potentials of sphere (dotted), disks (dashed) and rods (solid) at number density of 1 particle per μm^3 . (b) shows the curvatures of the potentials of spheres, disks and rods after scaling them to the same depth. 16

2.5 (a) Possible rod orientation between two curved surface and flat surface at the same separation. (b) Two different configurations of rod in contact with sphere surface. 19

2.6 (a)The function $K(h/L)$ for several values of L/a . (b)The dotted line is rod depletion scaled to 0.78 of original value in Derjaguin approximation and the dashed line is YJM model with $L/a = 1.5$. The potential form is almost identical. 20

2.7 (a) A semi-flexible rod is approximated by two stiff rods attached at a fixed angle. 22

2.8 The surface tension of bent rod suspensions in the presence of a flat wall as a function of bending angle α 22

2.9	The depletion interaction $V(h)$ [Eq. (2.17)] between two planar walls mediated by a bent rod with (a) $\alpha = \pi/7$ and (b) $\alpha = \pi/7$. The solid curve represents a bent rod depletion interaction which gives stronger attraction when h is small compared with $L \cos \alpha$ straight rod depletion curve (the dashed line) but overall it is smaller than with full contour length L straight rod depletion. This is qualitatively the effect observed in experiment [1].	23
2.10	(a) Equation of state of hard sphere systems. (b) Typical features of sedimentation equilibrium.	28
2.11	(a)-(c) theoretical phase diagram. (g)-(i) experimental data. η_p is the volume fraction of the polymer and ϕ is the volume fraction of the colloids in the sample. The symbols denote the following: circle, fluid; diamond gas plus liquid; cross, gas plus liquid plus crystal; plus sign, liquid plus crystal; square gas plus crystal; triangle, gel or no visible crystallites; star, glass.	30
2.12	(a) A typical Yukawa-like repulsive potential with screen length κ^{-1} . (b) Phase Diagram for particles interacting through a Yukawa potential. a_s is the average interparticle distance. $\Gamma = U(a_s)/k_B T$	33
2.13	(a) shows a group of points of position (x_i, y_i) and (b) shows a surface plot of a two dimensional array with non-zero value at (x_i, y_i)	37

2.14	The scheme of calculating pair correlation function.	38
2.15	A voronoi cell of point i are generated by the bisectors of points i and all other points. If one draws a line between any two points whose voronoi domains touch, a set of triangles is obtained, known as the Delaunay triangulation. The number of edges is the same as the number of triangulation bonds \mathbf{r}_{ij} . We can choose the angle θ_{ij} between the bond \mathbf{r}_{ij} to a reference axis, say x -axis or the angle θ'_{ij} between edge \overline{ab} to the reference axis because $ \theta - \theta' = 90^\circ$	40
2.16	Schematic drawing from [2] of a hard sphere fluid in contact with a patterned wall. It can either just flow around the structure forming an inhomogeneous fluid (a) or form a crystalline layer of thickness ℓ following the structure imprinted on the surface (b).	46
2.17	Roughening transition (a) $T < T_R$ and (b) $T > T_R$	49
2.18	(a) commensurate structure of particles on a square lattice. (b) incommensurate structure. (c) schematic drawing of misfit dislocations. Lines represent lattice planes. Thick lines are for substrate lattice planes and thin lines for the adsorbate ones.	52
3.1	The schematics of thermal imprint.	67
3.2	AFM scan of (a) line grating template and (b) crossed grating template.	68
3.3	The schematics of soft imprint.	70

3.4	AFM scan of a waffle template.	71
3.5	(a) a wide spread colloidal crystal formed on clean glass substrate where colloidal fluid wet the substrate well. (b) A droplet like colloidal crystal formed on a substrate made of optical glue (SK9). (c),(d),(e) and (f) show different surface density of of colloids in the groove made of different optical glue (NOA61, SK9, NOA65 and NOA 72) with the same bulk concentration.	72
3.6	The image formation through a lens.	75
3.7	Two sets of conjugate planes: (a) image planes (b) aperture planes. The figure is reproduced from Introduction to Optics by F. L. Pedrotti and L. S. Pedrotti.	77
3.8	(a) a grating image. (b) The intensity profile of a grating image. (c) the positions of peaks in the intensity profile.	78
3.9	The schematic of an optical line scanned tweezer. A galvo mirror is placed in a conjugate plane of the back focal plane of the microscope. The oscillation of the galvo mirror control the translational scan of a laser tweezer in the image plane which produce a time-average 1D optical potential.	82

3.10 (a) the solid line represents the raw potential measured with fd virus and the open circle represents the raw potential measured in a pure buffer. The dashed line is the parabola fit to the raw buffer potential. (b) shows the fd depletion potential after subtracting the parabolic fit from the measured potential. 84

3.11 Comparing the blurred depletion potential with the subtractions of blurred optical potential from the blurred combined potential. The top lines are with $\sigma = 0.03$ and the bottom ones are with $\sigma = 0.06$. When σ is small, the two cases are almost indistinguishable. 85

3.12 The fd bacteriophage particle. a. The top is an electron micrograph of fd virus. b. The bottom is a schematic representation of the phage particle showing the location of the capsid proteins. The figure is adapted from [3]. 87

3.13 Persistence length vs. End-to-End distance for a semiflexible polymer with contour length $0.88 \mu\text{m}$. When the end-to-end distance becomes close to the contour length, the persistence length increases exponentially. 94

4.1 Comparison of typical data with three different models - Derjaguin rod, AO sphere and YJM models. 100

4.2	Interaction potential between pairs of (a) 1.0 μm and (b) 1.6 μm silica spheres in a suspension of fd virus at varying concentration. The dotted (solid) line is generated by the YJM model with $L = 880$ nm ($L = 825$ nm). The dashed line is generated by YJM model with length distribution. This is essentially indistinguishable from $L = 825$ nm model.	102
4.3	Probability distribution of fd end-to-end distance.	104
4.4	Compare Data with YJM model with different length $L=740, 760$ and 780 nm.	106
4.5	(a) The depletion zone for a bent rod rotating around the center of mass. (b) The depletion zone for a bent rod rotating around the end-to-end axis.	106
4.6	Comparison of a typical data set with three different models.	108
4.7	Compare YJM-L theory of $L = 920$ nm and $R = 780$ nm with data at given concentration.	111
4.8	Compare YJM-L theory of $L = 900$ nm and $R = 740$ nm with data with tunable concentration.	112
4.9	The bent rod approximation. (a) different bending mode of semiflexible rods. (b) With the same R and L the bent rod transverse amplitude W' is larger than the arc shape rod W generally by 10 – 20%.	113

4.10	Depletion Attraction Potentials at Different Ionic Strength	114
4.11	x is derived from samples with 2mM Sodium Borate + 10 mM NaCl, 0.5 mg/ml fd and the two other potentials are derived from samples with 10mM TE + 20 mM NaCl, 0.2 mg/ml fd and (a) Steric repulsion between particles due to the 'rod brush'. (b) Harmonic interaction potential due to bridging of fd between two spheres.	116
4.12	Schematic drawing of spheres in nematic rod suspension: (a) The spheres can be stabilized by one rod separation apart. (b) Strong attraction between spheres due to strong surface tension of rods in parallel.	118
5.1	(a) The hashed region represents the volume excluded to depletants. The dark region is the overlapped excluded volume. In flat wall and corner geometries, the overlapping excluded volumes are bigger than between spheres. (b) Colloids are driven to the grating grooves due to depletion interaction.	122
5.2	(a) typical bulk phase diagram of spheres and polymer [4]. (b) The phases on a flat surface with corresponding the bulk phases [5]. . . .	124

5.3	Phase-contrast micrographs of four representative 2D structures with the schematic reconstruction in the bottom left corner. The $S(k)$ computed from these images is shown in the top right corner. (A) Stripe phase. (B) Triangular phase. (C), (D) Scissor (Centered-Rectangular) phases with different scissor angles as defined in the structure function image of (C). In (C) we circle the mirror line of a twinning defect. (E) Diagram indicating the observed phases as a function of χ	125
5.4	(a) 1D pair correlation function along the groove direction for colloidal spheres in the stripe phase ($2a= 0.86 \mu\text{m}$, $p= 1.21 \mu\text{m}$, see Fig. 5.3a). For curve X , the first peak of $g(r)$ occurs at $r = 0.93\mu\text{m}$. The inset is the approximate bulk phase diagram scaled from [4] for this system as a function of Φ and C_P . (b) The comparison of $g(r)$ (dashed-line) of Z to the exact 1D hard-sphere correlation function (solid-line). . . .	128
5.5	At the bulk same concentration, the structure on the flat surface and on a line grating template.	129
5.6	Bond orientation order of the triangular phases.	130
5.7	The structure function $S(\mathbf{k})$ plotted in the xy plane for three different phases (a) stripe. (b) hexagonal and (c) scissor.	132

5.8 $S(k)$ for the centered rectangular phase shown in Fig. 5.3C. The peak positions are indicated in the inset. The \times 's indicate delta-function Bragg peaks and circles indicate Lorentzian-like peaks. The grooves are aligned parallel to the Y-axis, and plot $S(k)$ vs k_x , at four different values of k_y . The topmost row shows the Bragg-peaks (i.e., at $k_y = 0$) scaled $50 \times$ smaller. For non-zero k_y , the curves are well modeled by Eq. 5.1 (solid curves). 134

5.9 (a), (b) and (d) illustrate 2D colloidal assembly commensurate with the cross grating template Notice that the crystal orientation rotates by 45 degrees for $\chi = 0.71, 1.41$, and that different crystal domains are clearly seen in (c). The domain size in (b) is greater than the microscope field of view which is $60 \mu\text{m} \times 80 \mu\text{m}$. (c) shows the disorder structure when χ is far away from the commensurate value. 135

5.10 (a) fluorescent picture of a crossed grating template. (b), (c) DIC pictures of particles sediments on the template within few hours. (d), (e) and (f) particles sediments with polymer added. 138

- 5.11 (a) The solid lines show a voronoi diagram of square lattice with a void. The shaded pentagon indicates a vononoi cell with a missing lattice point. The dashed lines show Delauney triangulation. In the bottom right it shows that either bond 1 or 2 are allowed because they are the same length. Voronoi diagram gives no ambiguity in the square lattice analysis. (b) and (c) are the voronoi diagram from the fcc crystal data with shaded region as defects identified by Φ_4 139
- 5.12 The comparison of particle spacing between FCC and BCC crystals. 144
- 5.13 Three stages of crystal formation observed: (I) at lower ϕ a crystal commensurate with the template; (II) at intermediate ϕ a crystal with square symmetry with smaller interparticle separation; (III) RHCP structure formed above the template. 145
- 5.14 The positions of all the particles of a crystal at stage I projecting onto xy and xz plane. Particles from different layers are commensurate with each other well. 146
- 5.15 The positins of all particles of a crystal at stage II projecting onto the xy plane and in the xz plane. In (b) the particle positions have slight shift from original lattice because dislocation line in Fig. . The circled region showed the positions off from the commensurate lattice. 147

5.16 (a) silica particles nucleate on a BCC template for the first layer. (b) silica particles packed in hexagonal structure at higher layer.	148
5.17 Experimental data for three different stages.	148
5.18 The correlation function of the BCC-like crystal compared with simulated FCC and BCC crystals.	149
6.1 (a) V-W type of growth (Pb on graphite). (b) SK type of growth (Pb on Ge(111)). (pictures reproduced from [6]) (c) VW type of growth in colloidal solutions on optical glue. (d) FM type of growth in colloidal solution on clean glass.	155
A.1 $\mathbf{r}(s)$ is the position of a point on the curve and $\mathbf{t}(s)$ is a unit tangent vector at point $\mathbf{r}(s)$	157

List of Tables

3.1	Common Chemical Solvents Used for PMMA particles	59
3.2	Swelling Diameters in Different Solvents	60
3.3	Freezing Point of PMMA Particles at Different Solvents	61
3.4	Summary of fd Persistence Length Measurement	97
4.1	Average χ^2 for different R and L with concentration as a adjustable parameter.	109
4.2	Average χ^2 for different R and L with fixed concentration as measured.	109

Chapter 1

Introduction

Colloids consist of solid particles, with diameters ranging from 1 nm to 1 μm , suspended in a fluid. They are useful systems to study for several reasons. Their size scale fall within the realm the nano-technology and also within the realm of cell biology. The colloidal suspensions are commonly encountered in daily life, eg. in surface coatings, paper, paints, cosmetics, and so on. They can modify rheological or optical properties of the carrier fluid. Related industrial applications include chromatography, drug precipitation, oil-drilling, food processing, ion exchange, and electrophoretic deposition. Colloids have also captured the attention of physicists. They behave in many ways like atomic systems but can be studied in real-time and by direct visualization. They form the basis for new classes of materials such as photonic crystals, and the colloidal particles can be used as probes to study complex systems on microscopic scales.

Colloids are influenced by a wide spectrum of physics and chemistry. Generally

we characterize colloidal systems by the constituent size, shape, and interparticle interaction. Among other things, particle size and interaction determine the typical time scale for system evolution. For instance, if there is an attractive interaction between colloidal spheres with radius a , it induces locally bound pairs. The time τ_R required to break up the bound pairs is the relaxation time

$$\tau_R = \frac{6\pi\eta a^3}{k_B T} \exp\left(-\frac{U_{\min}}{k_B T}\right). \quad (1.1)$$

Here η is the viscosity, U_{\min} is the minimum of the interparticle potential, k_B is the Boltzmann constant and T is the temperature. This time scale is important to determine whether a system undergoes the equilibrium or non-equilibrium process. For the equilibrium process, the observation time must be sufficiently long so that the particles rapidly access all the possible configurational thermodynamic phase space by strong Brownian motion. τ_R is about 4 seconds for $2a = 1 \mu\text{m}$ and $|U_{\min}|/k_B T = 2$. Thus it is often possible to study crystallization, nucleation, melting phenomena by the direct visualization with video microscopy.

The most commonly studied colloidal particles are spherical. Other shapes include random coils, spheroids, rods (eg. actin filament), and disks (eg. clays). The particles can exhibit different flexibilities and the different steric structures have unique *excluded volume* effects related to the possible configurations of the particles. All of these properties contribute to the system entropy. One aspect of this thesis explores the entropic interactions between particles and examines the role of shape and

flexibility in colloidal suspensions.

The interparticle interaction determines the suspension stability. When there is a strong attractive potential between particles, they aggregate irreversibly. Two important interactions between colloidal particles which compete to determine suspension stability are the van der Waals attractions and the electrostatic repulsions. Derjaguin and Landau [7] and Verwey and Landau [8] (DLVO) developed the theories about colloidal stability taking into account both interactions. There are also steric, hydrodynamic and solvation interactions in colloidal suspensions. The interplay between these interactions and entropy gives rise to the complicated behaviors of colloidal suspensions. They exhibit fascinating equilibrium phases which provide a testbed for investigation of classical many-body statistical physics.

Thermodynamics tells us the equilibrium phases are determined by its Helmholtz free energy $F = E - TS$, where E is the internal energy of the system, T is the temperature and S is the entropy. The system evolves to minimize its Helmholtz free energy. Conventional phase transitions from fluid to crystalline phase takes place if the loss in entropy upon freezing is compensated by a decrease in internal energy; i.e. the ordering transition is “energy driven”, not “entropy” driven. Therefore in order to observe “pure” entropic phase transitions, the system with hard-core potential is the ideal candidate. The internal energy is zero when the particles are not in contact. When the system has a fixed number density, it can only evolve to increase its entropy

or have the same entropy [9].

Ludwig Boltzmann gave the statistical mechanical foundation of entropy

$$S = k_B \ln \Omega. \quad (1.2)$$

Here Ω is the number of states accessible to the system given the constraints of particle compositions N , volume V and energy E . The Boltzmann constant k_B is introduced here, a prefactor determining the scale of S in agreement with the Kelvin scale of temperature. The usual interpretation of entropy is that it is a measure of the “disorder”¹ of the system. Intuitively we consider crystalline solids as “ordered” and isotropic fluids as “disordered” because in the crystalline phase the particles are confined to periodic position but in the fluid phase particles can move with no obvious positional constraints.

Many remarkably surprising phases driven by entropy are observed. There exists the first order fluid-solid transition in the simple hard sphere systems. The hard rod system exhibits isotropic, nematic, and smectic phases. Mixing suspensions of different sizes or shapes further complicates the phase behaviors. For example, the addition of non-adsorbing polymer coils to a suspension of hard spheres lead to lower freezing points or phase separations between sphere-rich and sphere-poor regions. The mixtures of rods and spheres exhibit fascinating phases beyond isotropic, nematic and smectic phases [10]. The detailed statistical mechanical theories of the mixtures of

¹C. E. Shannon’s interpretation for the framework of information theory

suspensions are complicated. However, a simple and useful model for the fundamental mechanism was first proposed by Asakura and Oosawa [11] and later developed independently by Vrij [12]. They proved that the entropy gained by the depletants (eg. polymers) introduce an the effective attraction between spheres. As a result, the added polymers can be regarded as “inverse temperature” in the density-temperature phase diagrams as atomic systems. Both colloidal and atomic systems share similar phase behaviors in nature.

The phase behaviors and the dynamical properties of systems can be modified by interfaces or confined dimensions. The study of physics in confined geometries has yielded surprising results. For example, the melting/freezing transition in 2D is fundamentally different from its counterparts in 3D which is characterized by a first order transition. The theories of Kosterlitz-Thouless-Halperin-Nelson-Young (KTHNY) tell us that 2D solids can melt via two sequential phase transitions [13, 14, 15, 16]. Colloidal systems have been used to test the theory successfully. The behaviors of colloidal suspensions have been observed quite differently in geometric confinements such as patterned surfaces or periodic optical potentials in contrast to the bulk properties. The confinement changes the fluctuations of colloidal particles and thus change the nature of phase transitions. The presence of a surface induces a rich scenario of interfacial phase transitions sometimes connected with wetting or surface reconstruction. Surface freezing is a peculiar type of wetting transition, where a liquid surface builds

up spontaneously several crystalline layers above the bulk freezing temperature. It has been proved theoretically that a hard sphere suspension exhibit surface-induced freezing at lower freezing point near a patterned substrate [17]. Our preliminary data may show this kind of transition.

In this thesis we investigate hard-sphere-like systems with the entropic interactions. We focus especially on the depletion interaction which arises in mixtures of colloidal suspensions. In chapter 2 we will calculate the depletion interactions, review entropy-driven phase transition phenomena, and discuss phase transitions in confining geometries. In chapter 3 we describe the experimental techniques needed for the measurements including handling colloidal systems, imprinting with gratings, optical microscopy, line-scanned optical tweezers, and the production of fd virus. In chapter 4 we discuss the measurements of depletion interactions between two spheres in a suspension of rod-like molecules, fd virus. We test existing theories based on rigid rods and in the process discover subtle, but non-negligible changes in the interaction potentials from rod flexibility. The interaction measurement thus provides an independent measurement for the persistence length of semi-flexible rods. We found that persistence length of fd is 2-3 times smaller than the literature value. In chapter 5 we then show a rich variety of 2D phases of colloid/polymer mixtures on patterned surfaces. The analysis of their structure functions shows the dependence of fluid- or solid-like structures on commensurability with patterned substrates. Our pre-

liminary studies on hard sphere crystal growth on templates of expanding lattices suggest a key parameter, osmotic pressure Π . Three phases are observed: commensurate crystals, incommensurate crystals and hexagonal packed crystals. The depletion interaction increases the crystal growth rate but may also change the structure of crystals. In chapter 6 we conclude with a summary of our findings and explore many new possibilities we can study in the future.

Chapter 2

Theory of Entropic Driven Colloidal Systems

A quantitative analysis of suspension stability and phase behavior requires an accurate modeling of the basic interactions between colloids. Important interactions in colloidal systems include entropic, electrostatic, van der Waals and hydrodynamic interactions. In this chapter we derive entropic interactions which are crucial in the mixtures of suspensions. After understanding the nature of the entropic interactions in colloidal suspensions, we review a few well-studied colloidal systems and their equilibrium phases driven by entropy without going into theoretical detail. We pay attention to the freezing/melting transitions in confined geometries and discuss useful order parameters used in this type of phase transition phenomena. Understanding the behavior of the model systems may shed light on our systems of colloidal suspensions on patterned surfaces. At the end we review a recent theory [2] about precrystallization on patterned surfaces which has direct implication on our experiments. We extend the discussion to related concepts such as roughness and the commensurate-

incommensurate transition in surface science, which we may investigate systematically in our systems in future experiments.

2.1 Rod Depletion Interaction between Two Plates

The depletion interactions between two parallel plates immersed in a solution of hard spheres or rigid rods were first considered by Asakura and Oosawa [11]. In their pioneering work they have commented that depletion interactions due to different geometric particles may give rise to interesting phenomena. For example, latex particles can aggregate by adding fibrous proteins or linear polyelectrolyte molecules; however, no aggregation of latex particles was observed early on by adding rigid spherical macromolecules [18].

In 1981 Auvray calculated the depletion interaction between two spheres in dilute rigid rod solution using the Derjaguin approximation. The calculation was conceptually correct, but missed a factor of 2 [19]. The correct expression was reported in [20] wherein the calculation was also extended to the third order in rod concentration. More recently, Yaman, Jeppesen and Marques (YJM) accounted for sphere curvature beyond the Derjaguin approximation [21]. Other calculations have been performed for rod-like shape depletion interactions [22, 23, 24]. The effects of such interactions have been explored theoretically in the phase diagrams of rod-sphere mixtures [25, 26].

We first consider the rotational degrees of freedom of an infinite, thin rigid rod

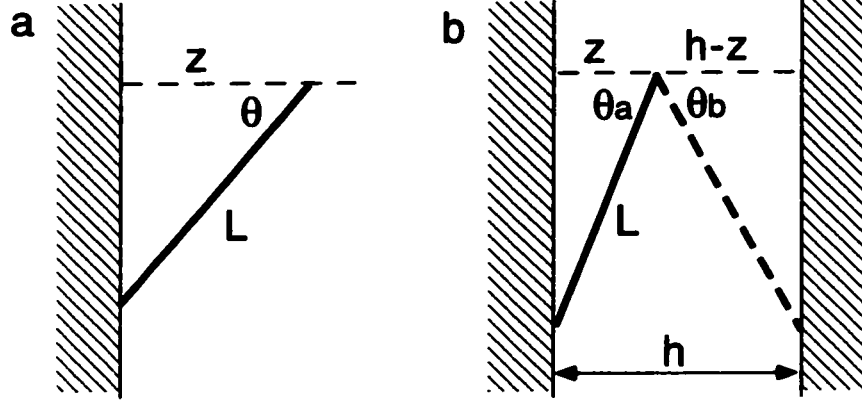


Figure 2.1: (a) A rod near a hard wall with one end at distance z . The rotation is restricted when $z < L$ and the angle between the rod and the normal to the wall is less than $\cos^{-1} \frac{z}{L}$ is unavailable. (b) A rod between two parallel hard walls with separation h .

in the presence of a repulsive wall (see Fig. 2.1a). The probability of finding one of the end of the rod at a distance \mathbf{r} with orientation characterized by the angle θ is given by the Boltzmann factor: $f(\mathbf{r}, \theta) \sim \exp[-U_e(\mathbf{r}, \theta)/k_B T]$, where k_B is the Boltzmann constant, and T is the temperature and the normalization requires $\int d^3\mathbf{r} \int d\theta \sin \theta f(\mathbf{r}, \theta) = 1$. The hard wall potential is

$$U_e(\mathbf{r}, \theta) = \begin{cases} \infty, & \text{if any part of the rod touches the wall} \\ 0, & \text{otherwise.} \end{cases} \quad (2.1)$$

The corresponding grand-canonical potential of a dilute rod suspensions is given by

$$\Omega = -\frac{Nk_B T}{2} \int d^3\mathbf{r} \int d\theta \sin \theta f(\mathbf{r}, \theta), \quad (2.2)$$

where N is the total number of rods in solutions.

The surface tension between the plate and rod solution $\Delta\gamma$ is the difference be-

tween the grand potential with and without a wall divided by the surface area, A :

$$\begin{aligned}\frac{\Delta\gamma}{k_B T} &= \frac{\Omega - \Omega_0}{A} \\ &= \frac{n k_B T}{2} \int \frac{d^3\mathbf{r}}{A} \int d\theta \sin\theta \left[1 - e^{-U_e(\mathbf{r},\theta)}\right].\end{aligned}\quad (2.3)$$

where n is bulk number density. In the simple one wall case the surface tension can be calculated easily

$$\frac{\Delta\gamma}{n k_B T} = \int_0^L dz \left[1 - \frac{1}{2} \int_{\cos^{-1} z/L}^{\pi} d\theta \sin\theta\right] = \frac{L}{4}.\quad (2.4)$$

The positive surface tension tells us that it takes energy to create the interface of a hard wall in a rod solution; and therefore when there are two walls, it is energetically favorable to have two walls in contact. This is the origin of the entropic driven attraction - depletion force. In the two wall case the surface tension is a function of separation,

$$\frac{\Delta\gamma(h)}{n k_B T} = \frac{2}{A} \int_0^{h/2} dz \left[1 - \frac{1}{2} \int_{\theta_a}^{\theta_b} d\theta \sin\theta\right] = \frac{h}{A} \left(1 - \frac{h}{2L}\right).\quad (2.5)$$

where $\theta_a(z) = \cos^{-1} z/L$ and $\theta_b(z) = \pi - \cos^{-1}(h - z)/L$. Therefore, the depletion interaction per unit area between two walls is the surface tension difference for separations h and ∞ :

$$U(h) = -\frac{1}{2} n k_B T L (1 - h/L)^2\quad (2.6)$$

We can also understand the depletion interaction from other points of view. The attractive potential between two plates is the work done as a result of the rods exerting

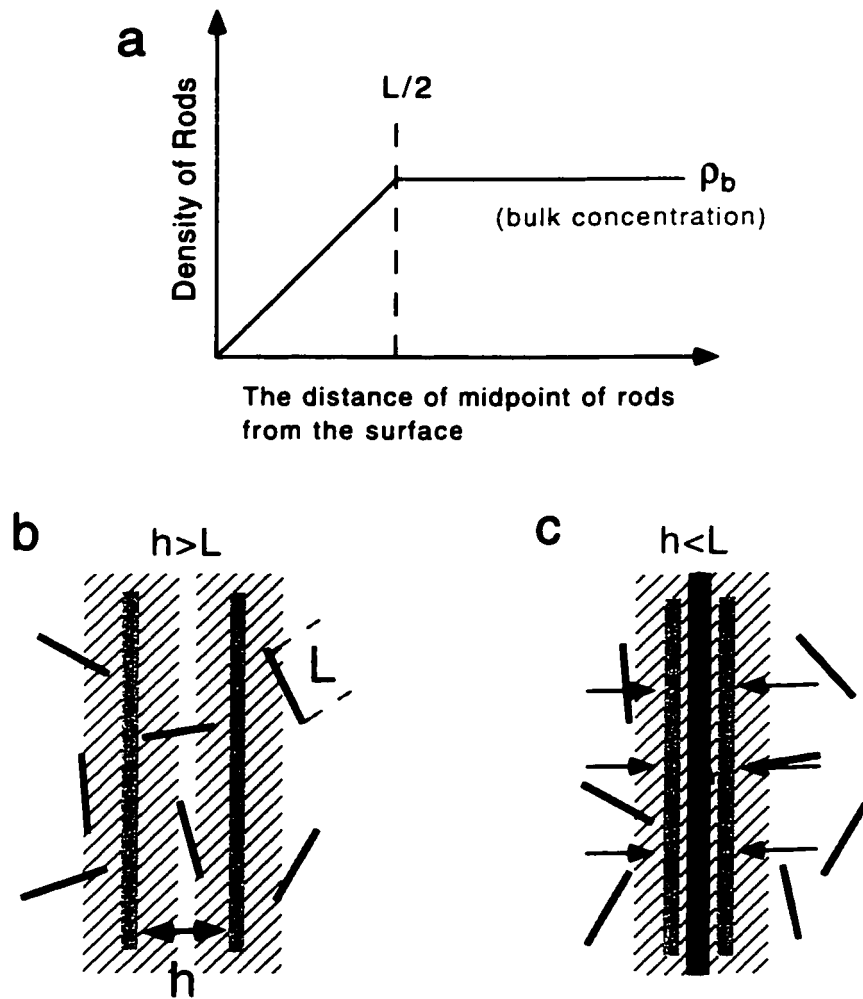


Figure 2.2: (a) The number density profile of a dilute rigid rod suspension from a flat wall. The depletion interaction between two plates in rod suspensions. The hatched region with thickness $L/2$ is the depletion zone where a rod loses the rotational degrees of freedom when its center is in the region. (b) Plates separation h is larger than the rod length L . The number density inside plates is the same as outside; therefore, the osmotic pressure on both sides are balanced. (c) when $h < L$: the black region is the overlapped depletion zone. The number density outside plates is larger than inside; therefore the osmotic pressure exerted by rods inducing an attraction between plates.

osmotic pressure onto the large plate. The force per unit area on a plate is simply the differential pressure on its two sides $\Pi(h) = k_B T [n(\infty) - n(h)]$. $n(h)$ is the number density of rods between plates with separation h . The rod chemical potential $\mu = \partial \ln \Omega / \partial N$ (from Eq. 2.2) is proportional to the accessible volume for a rod's rotational and translational degrees of freedom. Therefore, the rod number density is *depleted* close to the wall (see Fig. 2.2a). The depletion zone or excluded volume is shown by hatched region in Fig. 2.2. When two plates are separated by less than L , the osmotic pressure from outside pushes two plates together (Fig.2.2c). The amount of work done per unit area by the rods is $W(h) = \int dh' \Pi(h')$ where the integration range is the overlapped volume (dark shading).

The interaction may be best illustrated as an entropic effect by considering the free energy $F = -T\Delta S$, which is the entropy difference between two plates with separation $h > L$ (b) and $h < L$ (c). Rods lose rotational degrees of freedom (and thus entropy) when their center lies in the depletion region (hashed regions) whose thickness extends $L/2$ beyond the surface of the large plates. When the large plates approach each other, these depletion zones overlap and the volume V_{overlap} becomes accessible to the rods and thus increases rod entropy.

In the calculation of rod entropy, we may also take Onsager's approach by considering rod of different orientation as different "species". Rods of orientation θ with respect to the normal of the wall cannot access the volume (thus lose entropy) as

their midpoint lie within $L \cos \theta/2$ from the wall. All these views are equivalent and have different advantages in more complicated depletion interaction calculation.

2.2 Derjaguin Approximation

The interactions between flat plates can be calculated accurately without much labor, but often they give only qualitative physics for colloidal systems. The colloidal stability is determined by the potential per sphere compared with $k_B T$ [27]. Derjaguin first proposed the potential between two spheres can be integrated from the potential of two flat surfaces

$$U_s(h) = \pi a \int_h^\infty U_{\text{plate}}(z) dz. \quad (2.7)$$

The Derjaguin approximation (Eq. 2.7) is valid when the interaction range ξ is much smaller than the sphere radius a . Fig. 2.3 illustrates the spirits of this approximation. The curved surface of a ball is divided into rings and the total energy is the sum over all the interaction between annuli of area $2\pi r dr$ over the range of distances between spheres, i.e.

$$U_s(h) = 2\pi \int_0^\infty U_{\text{plate}}(z) r dr \quad (2.8)$$

where U_{plate} is the interaction energy per unit area between two flat plates as a function of separation. The separation between annuli and the size of annuli are related as

$$r^2 = (a + z/2)^2 - a^2 = az + z^2/4. \quad (2.9)$$

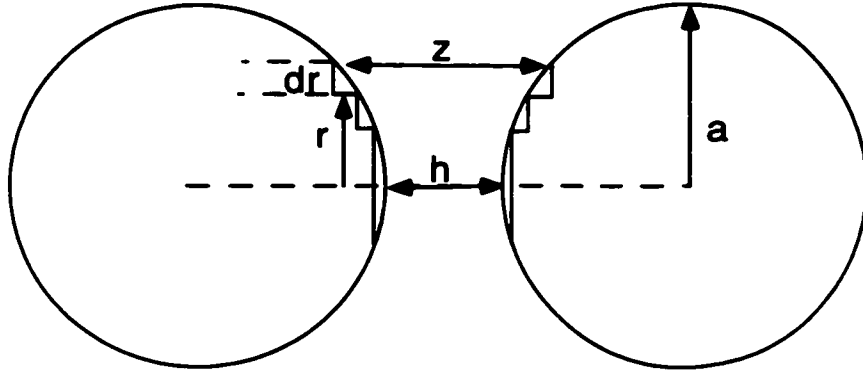


Figure 2.3: Schematic illustration that shows how the interaction between spheres may be calculated from the interaction between flat plates

Only the first term of Eq. 2.9 is important when $z < \xi \ll a$. Eq. 2.7 is obtained by using the derivative of Eq. 2.9, $2rdr = adz$. This simple geometric relationship of Derjaguin approximation Eq. 2.7 shows that sphere interaction should scale like $\xi a U_{\text{plate}}$.

By utilizing Eq. 2.6 in the Derjaguin approximation, Eq. 2.7, the rod depletion interaction between spheres is

$$U_{\text{rod}}(h) = -\frac{\pi}{6} k_B T n a L^2 (1 - h/L)^3. \quad (2.10)$$

2.3 Depletion Interaction Due to Spheres and Disks

Before we proceed to the non-Derjaguin regime of $L \sim a$, we compare depletion interaction between spheres due to depletants of different geometric shape. The depletion interaction between two big spheres in the suspension of small spheres of diameter σ

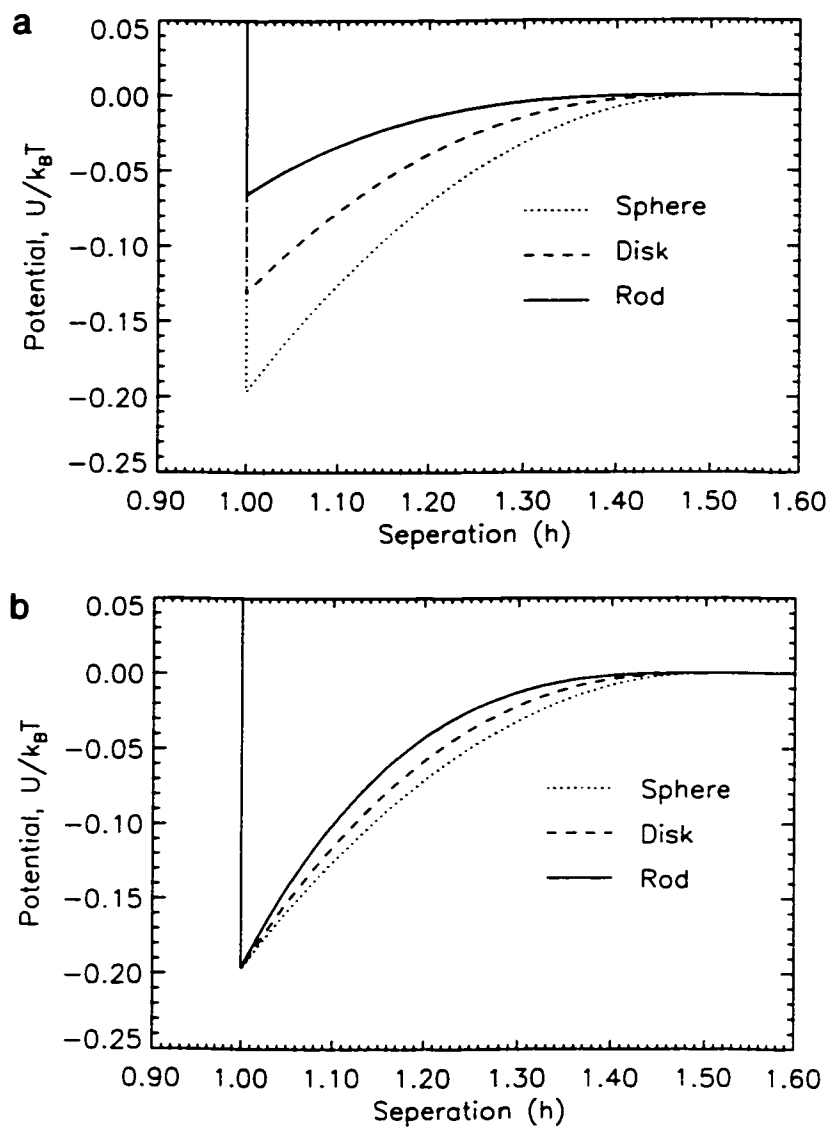


Figure 2.4: (a) The depletion potentials of sphere (dotted), disks (dashed) and rods (solid) at number density of 1 particle per μm^3 . (b) shows the curvatures of the potentials of spheres, disks and rods after scaling them to the same depth.

is

$$U_{\text{sphere}}(h) = -\frac{\pi}{2} k_B T n a \sigma^2 (1 - h/\sigma)^2, \quad (2.11)$$

and the depletion interaction in the suspension of disks of diameter D is [23]

$$U_{\text{disk}}(h) = -\frac{\pi}{2} k_B T n a D^2 \left[\frac{1}{3} \left(2 + \frac{h^2}{D^2} \right) \sqrt{1 - \frac{h^2}{D^2}} - \frac{h}{D} \left(\frac{\pi}{2} - \sin^{-1} \frac{h}{D} \right) \right]. \quad (2.12)$$

Fig. 2.4a compares three depletion potentials due to spheres (dotted curve), disks (dashed curve) and rods (solid curve) at the same number concentration with the same size length $L = D = \sigma$. Clearly, sphere depletion interaction gives the strongest attraction than disk and rod depletion interaction. The minima for different potentials, $U_{\text{sphere}}(0) = 3/2 U_{\text{disk}}(0) = 3 U_{\text{rod}}(0)$, are related the objects' allowed degrees of freedom. The other more subtle difference is the shape of interaction potentials. Fig. 2.4b shows the potential curves are scaled by the contact value ratio. Rod depletion interaction is highly curved as $U_{\text{rod}} \sim (1 - h/L)^3$ and sphere depletion is least curved $U_{\text{sphere}} \sim h^2$. This comparison shows that the depletion interaction can probe geometric shape of depletants.

The other interesting effect is the volume fraction. The relationships between volume fraction and number density for different geometric objects are:

$$\phi_{\text{sphere}} = 1/6 \pi \sigma^3 n, \quad (2.13)$$

$$\phi_{\text{disk}} = 1/4 \pi D^2 L_d n, \quad (2.14)$$

$$\phi_{\text{rod}} = 1/4 \pi D_r^2 L n, \quad (2.15)$$

where we have assumed the disk is of thickness $L_d \ll D$ and the rod is of diameter $D_r \ll L$. Of the same number density, the volume fraction ratio of spheres, disks and rods of the same size ξ is $\xi^2 : \xi L_p : D_r^2$. In other words, rods of aspect ratio $L/D_r = 100$ can induce the depletion interaction at the same order of magnitude as spheres while its volume fraction is 10^{-4} to the sphere volume fraction.

2.4 The YJM Model

Recent experiments are generally carried out with the mixtures of rods and spheres of comparable size where the Derjaguin approximation is violated [28, 10]. The Derjaguin approximation gives rise to quantitatively incorrect estimate for the depletion interaction. In the experiments of Tracy *et al.* [28], the authors did not observe the phase separation which Derjaguin model predicts. In 1998, Yaman, Jeppesen, and Marques calculated the exact depletion potentials for arbitrary size ratio a/L . They took into account a rod near a curved surface. When the curvature of the surface is considered, there are fewer excluded orientations when the rod is near a sphere (see Fig.2.5a). Also there are two different ways for the rod to contact the wall. When the center of rod $z > \sqrt{(L/2)^2 + a^2} - a$, the tip touches the wall; when $z < \sqrt{(L/2)^2 + a^2} - a$, the rod is tangent to the sphere on its side. This makes the calculation of phase space available to rods between two spheres complicated. There is no single analytic solution for arbitrary a/L . The authors expressed the potential

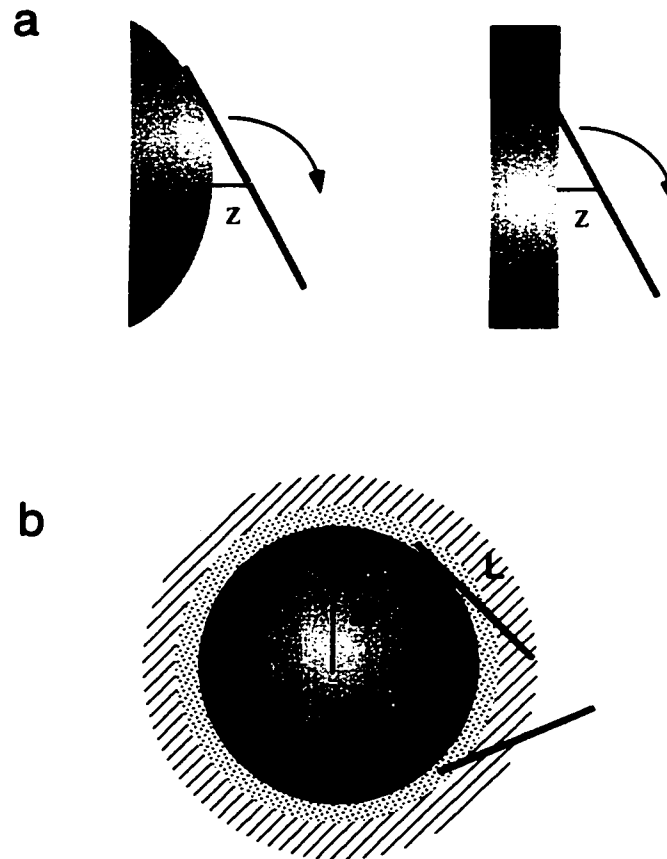


Figure 2.5: (a) Possible rod orientation between two curved surface and flat surface at the same separation. (b) Two different configurations of rod in contact with sphere surface.

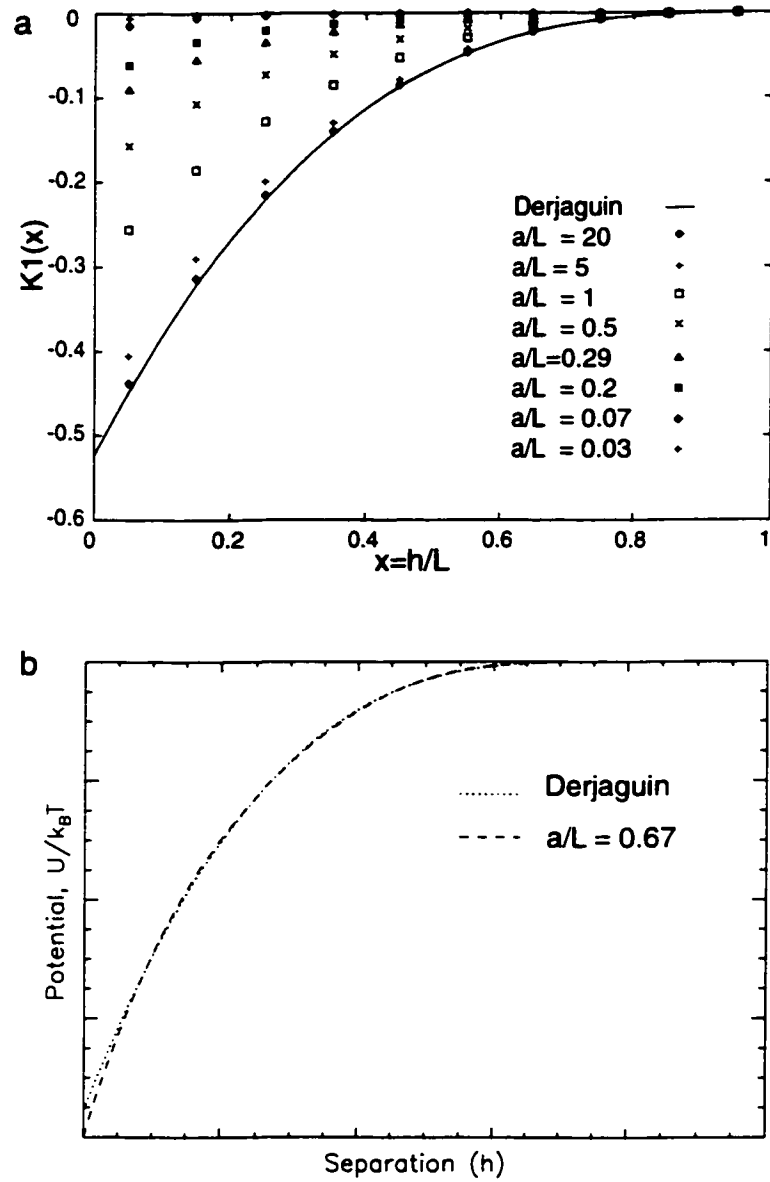


Figure 2.6: (a) The function $K(h/L)$ for several values of L/a . (b) The dotted line is rod depletion scaled to 0.78 of original value in Derjaguin approximation and the dashed line is YJM model with $L/a = 1.5$. The potential form is almost identical.

in the following form

$$U_{YJM}(h/L; a/L) = -k_B T n_r a L^2 K(h/L; a/L). \quad (2.16)$$

where $K(h/L; a/L)$ is calculated numerically. Fig. 2.6a shows $K(h/L; a/L)$ at different values of L/a . When $L \sim a$, the potential deviates about 50% from Derjaguin approximation. The shapes of potentials of small a/L do not differ much from Derjaguin model (Fig. 2.6b). The most important modification on rod depletion interaction between two spheres in non-Derjaguin regime is the decrease of attractive potential because the entropy gain from overlapped excluded volume is overestimated in Derjaguin approximation.

2.5 Bent Rod Approximation

In our experiments to be discussed in Chapter 4 the rods are not perfectly rigid. They are flexibly bent. Inspired by the experimental results [1], Lau [29] approximated a bent rod as two stiff rods attached together at a fixed angle. Fig. 2.7 shows that the angle is determined by the end-to-end distance and contour length, $\alpha = \cos^{-1} R/L$. The probability of finding one end of a bent rod at a distance \mathbf{r} with orientation characterized by $(\hat{\mathbf{u}}, \phi)$ is given by the Boltzmann factor: $f(\mathbf{r}, \hat{\mathbf{u}}, \phi) \sim \exp[-U_{ext}(\mathbf{r}, \hat{\mathbf{u}}, \phi)/k_B T]$. The surface tension of a flat wall in the bent rod suspension can be calculated by similar approach in Section 2.1 (see Fig.2.8). The bigger the bent angle α the rod has, the smaller the surface tension is. Thus the depletion interaction

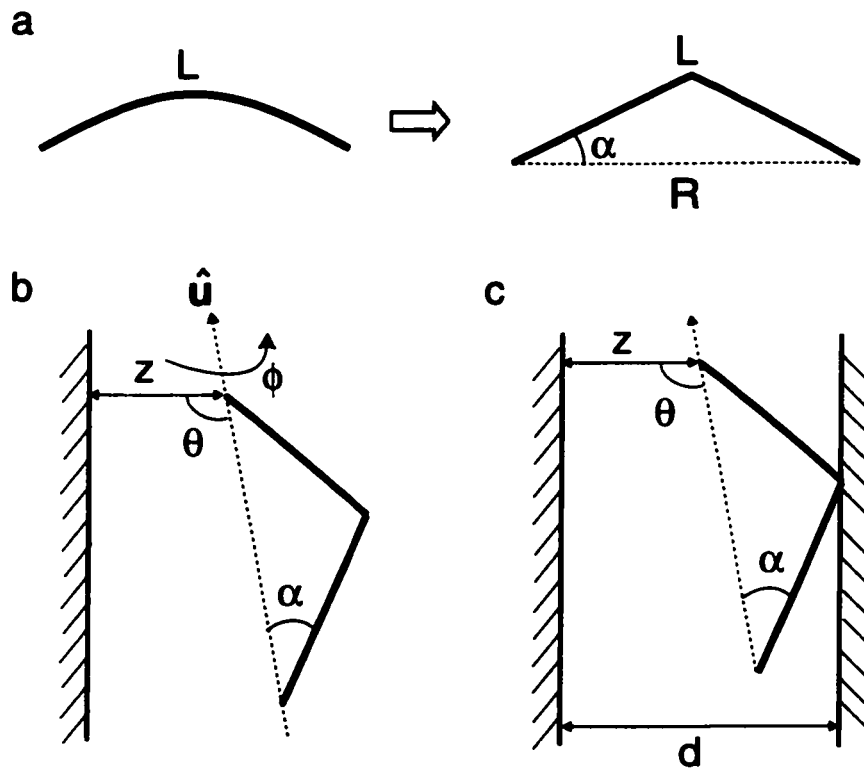


Figure 2.7: (a) A semi-flexible rod is approximated by two stiff rods attached at a fixed angle.

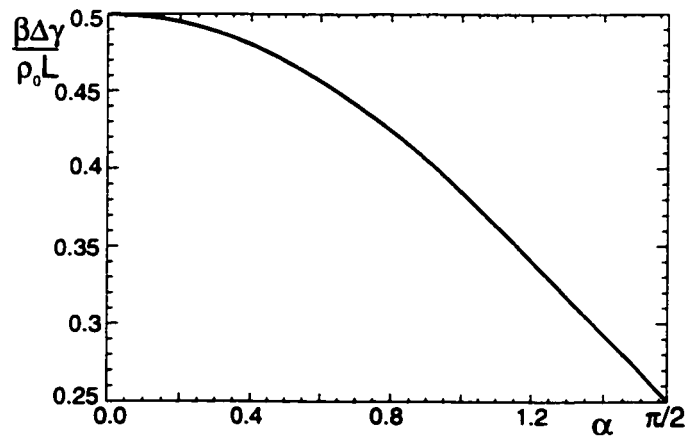


Figure 2.8: The surface tension of bent rod suspensions in the presence of a flat wall as a function of bending angle α .

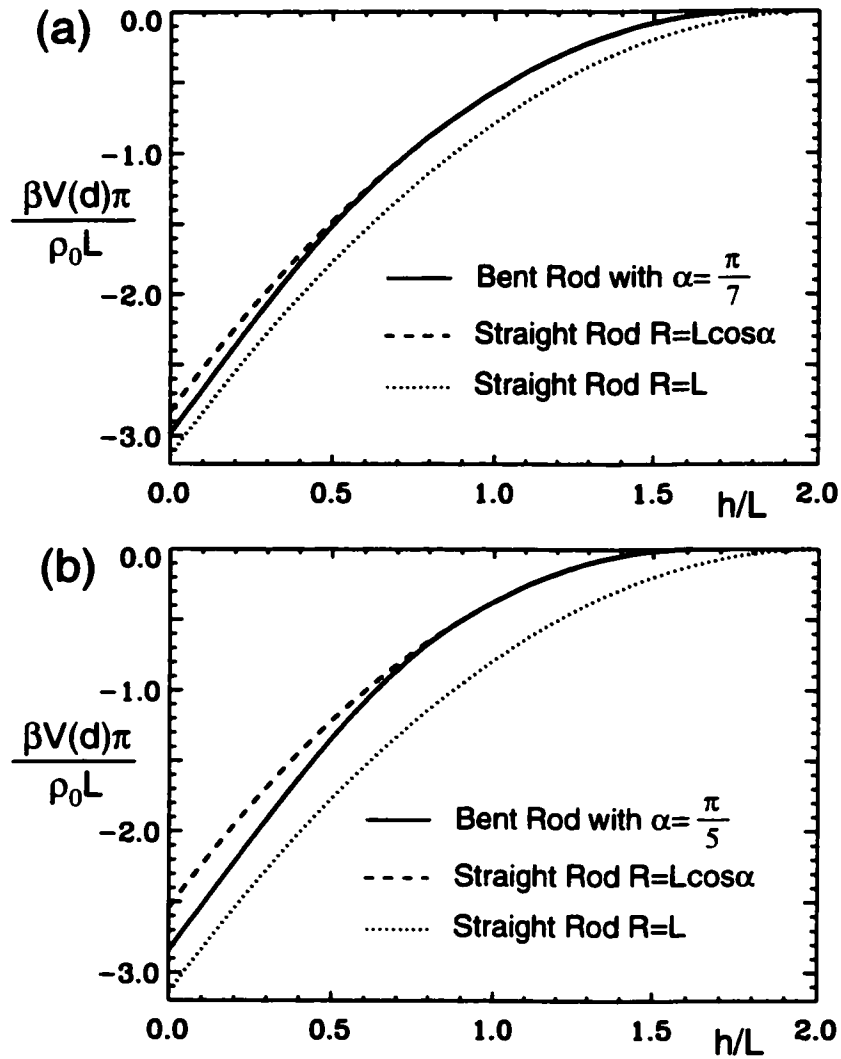


Figure 2.9: The depletion interaction $V(h)$ [Eq. (2.17)] between two planar walls mediated by a bent rod with (a) $\alpha = \pi/7$ and (b) $\alpha = \pi/5$. The solid curve represents a bent rod depletion interaction which gives stronger attraction when h is small compared with $L \cos \alpha$ straight rod depletion curve (the dashed line) but overall it is smaller than with full contour length L straight rod depletion. This is qualitatively the effect observed in experiment [1].

between two flat plates is smaller for bigger α . The depletion attraction potential between two parallel plates has the following form

$$V(h) = -n_0 k_B T \left[\frac{L \cos \alpha}{2} \left(1 - \frac{h}{L \cos \alpha} \right)^2 + \Gamma(h, \alpha) \right]. \quad (2.17)$$

The first term is the the depletion potential due suspension of straight rods with $R = L \cos \alpha$ which rotate around the midpoint of a rod and $\Gamma(h, \alpha)$ is the contribution from the rotational degree of freedom around the end-to-end axis of the bent rod. The two independent movements of rods contribute to two decoupled term in the interaction. Fig. 2.9 compares the bent-rod depletion interaction between two plates with two different angles along with the straight rod depletion interaction. The larger bent angles gives smaller attraction at contact but larger deviation from the straight rod potential. This is qualitatively similar to our experimental data. For the interaction between two spheres, the Derjaguin approximation is applied on the contribution from rotation around axis $\pi a \int dh' \Gamma(h', \alpha)$ because the interaction range is $L \sin \alpha$ which is smaller than a . The rods in the experiment is rather stiff. The contribution from straight rod of $L \cos \alpha$ is replaced by YJM model. In Chapter 4 We will compare the experimental data with the YJM-L model

$$U(h) = -k_B T n a R^2 \left[K \left(\frac{h}{R}; \frac{a}{R} \right) + \frac{\pi}{R^2} \int_h^\infty dh' \Gamma(h', \alpha) \right]. \quad (2.18)$$

2.6 Equilibrium Phase Behaviors

We have discussed the entropic interaction between colloids and now we will review equilibrium phase behaviors of a few model colloidal systems and introduce the correlation function and bond order parameters which are useful in investigating phase transitions. The phase transitions observed in colloidal systems can be divided into two classes [30]:

(i) disorder-order transitions driven by entropic effects in systems dominated by the repulsive interparticle potentials such as hard sphere or electrostatic interaction.

(ii) fluid-fluid or fluid-solid transitions caused by weak attractions.

The first class corresponds to the freezing transitions in molecular systems. There are small density differences between two existing phases. The second class corresponds to the gas-liquid, gas-solid transitions in molecular systems. There is distinct density difference between two phases. The basic features of the phenomena can often be understood qualitatively with simple models for the interparticle potentials. Detailed calculations of phase diagrams can be achieved by virial expansions, perturbation theories, Monte Carlo and molecular dynamics simulations with specific potentials. The theoretical efforts have been tested and motivated by experiments with a variety of model colloidal systems.

2.7 Hard Sphere System

Hard sphere systems are interesting for various reasons. They are useful models such as simple liquids [31] and glasses [32]. Often they are also excellent approximation for dense-particles systems with more complicated potentials because the short-range interparticle repulsion is the major effect in determining the structure. The existence of a first-order order-disorder phase transition was surprising and greatly debated in 1950's. Intuitively, the freezing arises because the attractive energy between particles overcomes entropy loss of the systems and hard spheres lack these attractive interactions. The early analytical work and computer simulations [33, 34, 35] predicted the fluid-solid phase transition. It was not until 1980's that these ideas were tested experimentally thanks to major developments in colloidal science [36, 37].

The hard sphere system has two length scales: the average interparticle spacing, commonly expressed in terms of the number density n and the particle radius a . These two parameters lead to the only relevant dimensionless parameter, the volume fraction of the spheres,

$$\phi = \frac{4}{3}\pi a^3 n. \quad (2.19)$$

ϕ determines the pressure equation of state and thermodynamically stable phases for hard sphere systems (see Fig. 2.10a). A hard-sphere system is athermal, i.e. there is no temperature dependence to its grand potential, thermodynamic properties and phase diagram because the Boltzmann factor $e^{-U/k_B T}$ is either 0 or 1. At very high

volume fraction, the spheres are forced to touch and the pressure diverges. The volume fraction of random close packed spheres in three dimensions is 63.8% while the maximum packing can be reached at 74.05% for FCC or HCP. There exists a coexistence phase between a fluid ($\phi = 49.4\%$) and a crystal ($\phi = 54.5\%$). During the transition the individual spheres give up the long range positional degree of freedom by arranging periodically to relieve the crowding locally. This process maximizes the system entropy. A very useful expression for the equation of state for the fluid phase was derived by Carnahan and Starling [38],

$$Z(\phi) = \frac{\Pi}{nk_B T} = \frac{1 + \phi + \phi^2 - \phi^3}{(1 - \phi)^3} \quad (2.20)$$

where $Z(\phi)$ is known as compressibility factor describing the deviation from the ideal gas law. For solid phase the equation of state has the expression

$$Z(\phi) = \frac{2.22}{0.74 - \phi}. \quad (2.21)$$

Experimentally the direct measurements of colloidal suspension's thermodynamic quantities such as osmotic pressure are non-trivial. Measurements of equation of state are used to test the "hardness" of colloids [39, 40]. At low volume fraction it is measured by extrapolating the static structure function to zero wave vector [41, 39]. If there is density difference $\Delta\rho$ between ρ_{particle} and the solvent density ρ_{solvent} , the equilibrium sedimentation can be reached in few days to few weeks and used to determine the equation of state [42, 40]. The Nobel laureate J. Perrin first noted that

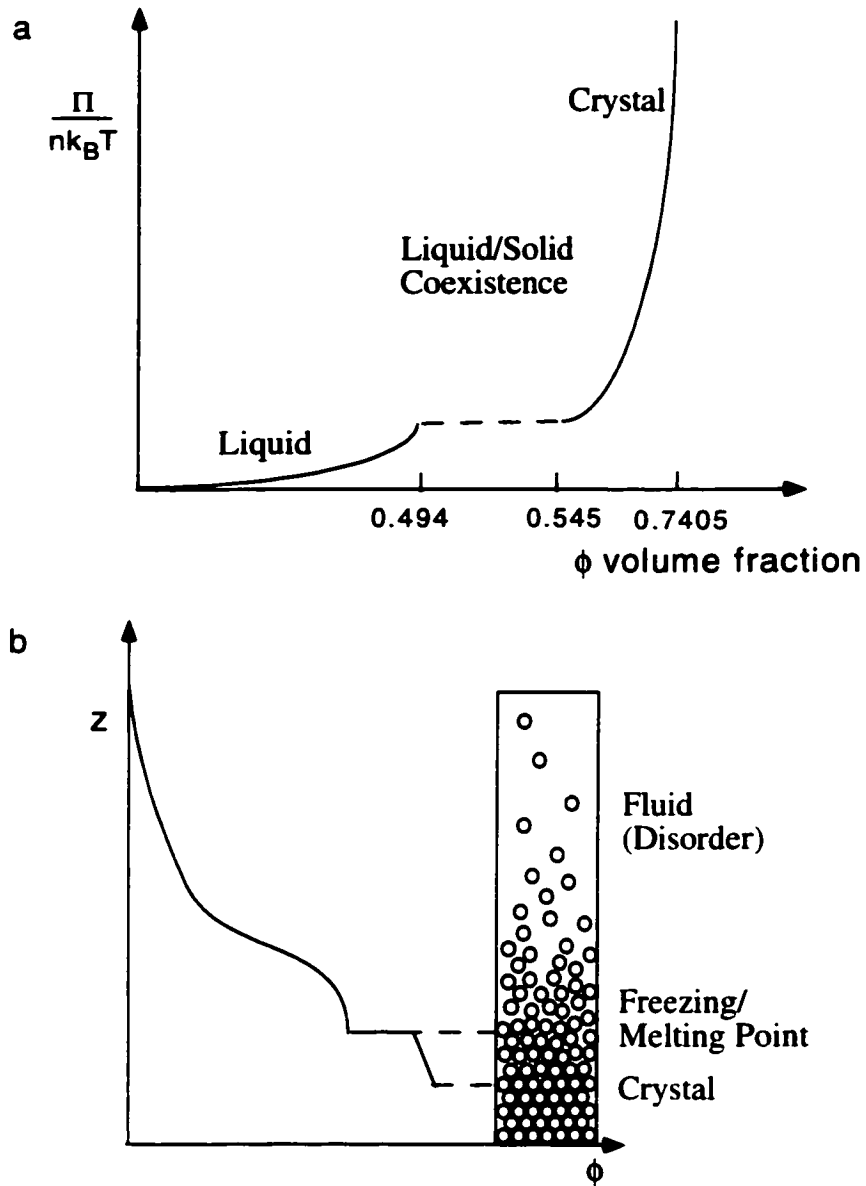


Figure 2.10: (a) Equation of state of hard sphere systems. (b) Typical features of sedimentation equilibrium.

one can measure the osmotic pressure of pollen particles by observing their sediments. In equilibrium the sedimented particle flux due to gravity is canceled by the upward diffusive flux from more concentrated particles in the bottom. The osmotic pressure Π at any height z must support the sum of the weight of the overlaying particles with buoyant particle mass $m_B = 4/3\pi a^3(\rho_{\text{particle}} - \rho_{\text{solvent}})$,

$$\Pi(z) = m_B g \int_z^\infty dz' n(z'). \quad (2.22)$$

The density $n(z)$ can be obtained by scattering or absorption. The variation of concentration over height is characterized by $\ell_g = k_B T / m_B g$ which is called the gravitational length ($\ell_g = 0.81 \mu\text{m}$ for particles of radius $a = 0.5 \mu\text{m}$, $\Delta\rho = 1 \text{ g/cc.}$) It takes months for particles with $a = 0.5 \mu\text{m}$ to reach equilibrium [43]. In the dilute regime where $\Pi(z) = n(z)k_B T$, we obtain the usual barometric law $n(z) \propto \exp(-z/\ell_g)$ by Eq. 2.22.

It is useful to understand the hard sphere system. In the following few sections we give a qualitative description of other concentrated colloidal systems largely based on our understanding of hard sphere systems. Expanding the hard sphere limit by perturbation methods is often appropriate for colloidal particles with short-ranged electrostatic and entropic interactions compared to the particle diameter.

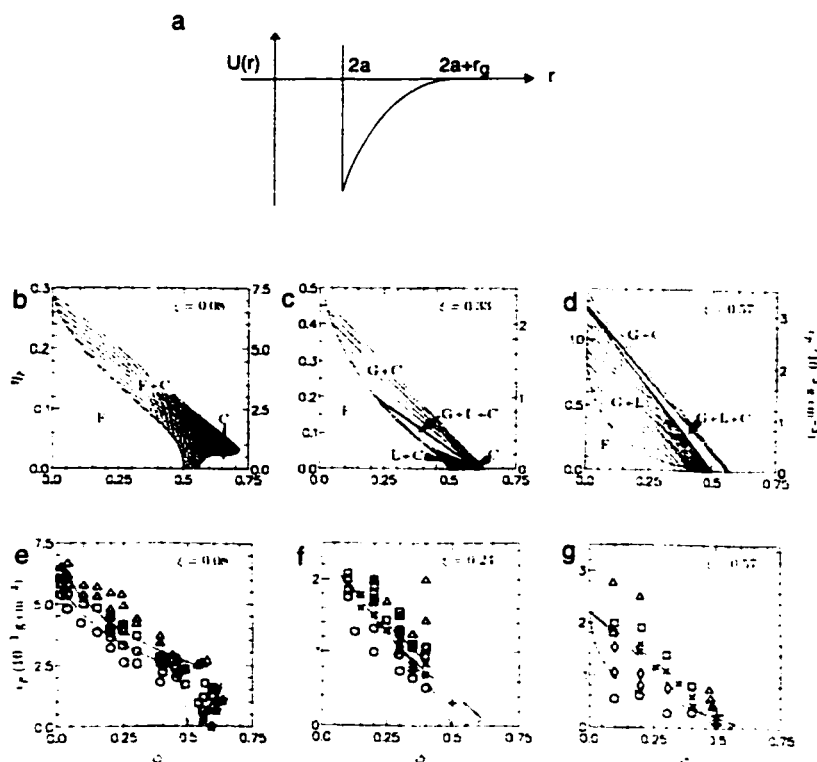


Figure 2.11: (a)-(c) theoretical phase diagram. (g)-(i) experimental data. η_p is the volume fraction of the polymer and ϕ is the volume fraction of the colloids in the sample. The symbols denote the following: circle, fluid; diamond gas plus liquid; cross, gas plus liquid plus crystal; plus sign, liquid plus crystal; square gas plus crystal; triangle, gel or no visible crystallites; star, glass.

2.8 Sphere/Polymer Mixtures

Phase separation in colloidal suspensions, induced by the addition of nonadsorbing polymer, is a phenomenon of fundamental interest and important technological application. The depletion of polymer molecules from the region between closely spaced particles leads to an effective interparticle attraction, as described in Sections 2.1-2.3. The typical depletion potential is shown in Fig. 2.11a and its range is determined by the polymer radius of gyration r_g . There are numerous experiments to show that the addition of enough non-adsorbing polymers to a suspension of colloidal particles causes phase separation (eg. [44, 45, 46, 47, 48, 4, 49]). There are also theoretical studies [50, 51] and simulations [52, 53]. The kinetics connected with these phase separations have been observed: nucleation and growth, spinodal decomposition, aggregation and (transient) gelation [54, 55, 56, 57]. The structure of the final state of the system depends on these kinetic pathways [58, 59].

The topology of phase diagrams is mainly determined by the size ratio $\xi = r_g/a$ of the radius of gyration r_g of polymer over the sphere radius a . When the size ratio is small which means shorter interaction range, there are three phases – fluid, solid and coexistence, the same as hard-sphere systems but with larger fluid-crystal coexistence region. For larger value of ξ , however, a three-phase coexistence of colloidal glass, liquid and crystal phase is observed. The crossover between these two topologies is found at $\xi \sim 0.25$. The phase diagrams shown in Fig. 2.11 is plotted as η_p , the vol-

ume fraction of polymer and ϕ , the volume fraction of colloids. The volume fraction of polymer ¹ can be considered as an inverse temperature so the diagram becomes effectively density-temperature phase diagram. Thus, variation of the effective polymer volume fraction is a way to control the “temperature” of hard sphere/polymer mixture systems.

2.9 Charged Sphere Systems

The other extensively investigated colloidal systems are the charged polystyrene spheres. The interaction between spheres is a screened-Coulomb (or Yukawa) repulsion which is derived through the linearized Poisson-Boltzmann equation describing the distribution of screening charges around a charged sphere. Fig. 2.12a shows a typical potential. The interaction range is determined by the screening length κ^{-1} . When κ^{-1} is very small compared with the sphere radius a , the spheres are hard sphere like. At low ionic strength, κ^{-1} is long compared with a . The long-range electrostatic repulsion can induce a phase transition at volume fraction as low as 10^{-3} . The other key parameter to describe the phase behavior is the correlation parameter $\Gamma = U(a_s)/k_B T$ where $a_s = (1/n)^{1/3}$ is the average interparticle distance. This measure the ratio between a particle interactions with its neighbors and its mean kinetic energy. The typical 3D phase diagram is shown in figure 2.12. BCC crystal structures

¹More correctly, we should use the effective volume fraction of polymer η_p^R which only consider the free volume left by the hard spheres instead of system total volume fraction.

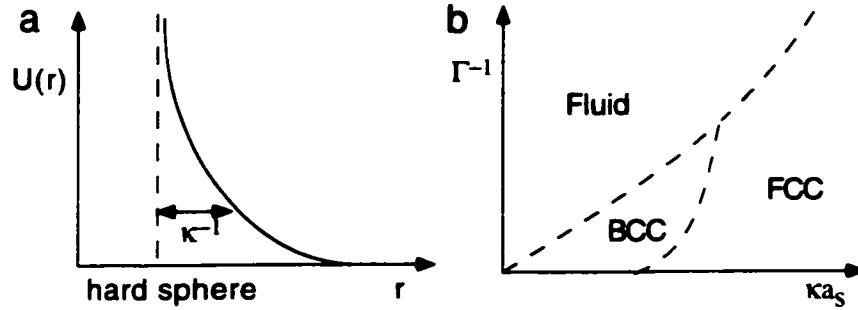


Figure 2.12: (a) A typical Yukawa-like repulsive potential with screen length κ^{-1} . (b) Phase Diagram for particles interacting through a Yukawa potential. a_s is the average interparticle distance. $\Gamma = U(a_s)/k_B T$

are found when the repulsion is “softer” ($\Gamma > 5$ and $\kappa a < 4$.)

2.10 Correlation Function and Structure Function

It is worthwhile to review the physical meaning of the structure function and the correlation functions which contain information about the average relative positions of particles within an ensemble. We will also show how we calculated and analyzed these quantities using David Grier’s IDL programs [60].

The density function which specifies individual particle positions of a system is written as

$$n(\mathbf{r}) = \sum_i \delta(\mathbf{r} - \mathbf{r}_i). \quad (2.23)$$

Features extracted from a micrograph are stored into an array of two column position coordinates (x_i, y_i) . The coordinates can be transformed into a 2 dimensional array of density function by creating a 2D matrix where the value of index $(x_i/\Delta x, y_i/\Delta y)$

is non-zero (2.13) where Δx and Δy are the grid sizes with respect to x and y coordinates. If the point does not fall exactly on a grid point in the image, the value is distributed among the neighboring grid points in a manner proportional to the mismatch. The grid size can be adjusted to smaller value in order to increase resolution but this costs the memory requirement and computation time.

Perhaps the most important ensemble averaged function is the pair correlation function:

$$\begin{aligned} \langle n \rangle^2 g(\mathbf{r}_1, \mathbf{r}_2) &= \langle n(\mathbf{r}_1) n(\mathbf{r}_2) \rangle, \text{ with } \mathbf{r}_1 \neq \mathbf{r}_2 \\ &= \sum_{i \neq i'} \delta(\mathbf{r}_1 - \mathbf{r}_i) \delta(\mathbf{r}_2 - \mathbf{r}_{i'}). \end{aligned} \quad (2.24)$$

If the system is isotropic and homogeneous, the pair distribution function is a function of relative separation $g(\mathbf{r}_1, \mathbf{r}_2) = g(|\mathbf{r}_1 - \mathbf{r}_2|)$; it is usually called the radial distribution function. $g(r)dr$ is the “probability” of observing another particle between \mathbf{r} and $\mathbf{r} + d\mathbf{r}$ given a particle at the origin. Clearly $g = 0$ when $r < 2a$ ($2a$ is the hard sphere diameter), and $g \rightarrow 1$ as $r \rightarrow \infty$ because the influence of the particle at the origin diminishes to zero as r becomes large. $g(r)$ can be calculated directly by computing histogram of all the pair separations \mathbf{r}_{ij} with $i \neq j$ of the systems, i.e., counting the number n of particle between $r \rightarrow r + \Delta r$. However, because of the finite system size, there are less particles with larger separations sampled. Therefore, we need to normalize the number n by the area r^2 or volume r^3 (Fig. 2.14). The radial distribution function is essential in the theory of liquids. All the thermodynamic functions of the

system can be written in terms of $g(r)$ [61]. The total energy E is

$$\frac{E}{Nk_B T} = \frac{3}{2} + \frac{n}{2k_B T} \int_0^\infty d\mathbf{r} u(r) g(r, n, T) \quad (2.25)$$

where $u(r)$ is particle pair potential. The equation of a fluid state is

$$\frac{\Pi}{k_B T} = n - \frac{n^2}{6k_B T} \int_0^\infty d\mathbf{r} r u'(r) g(r) \quad (2.26)$$

where $u'(r) = \partial u(r) / \partial r$. This equation is often called the pressure equation. Besides E and Π we need μ , the chemical potential, in order to get all of the other thermodynamic functions. The chemical potential is the energy difference when adding one extra particle into the system. A coupling variable ξ is introduced. A particle is in and out of the system by $\xi = 1$ or 0 respectively. The chemical potential μ is linked to $g(r)$ by

$$\frac{\mu}{k_B T} = \ln n\Lambda^3 + \frac{n}{k_B T} \int_0^1 d\xi \int_0^\infty d\mathbf{r} u(r) g(r; \xi) \quad (2.27)$$

where $\Lambda = (2\pi\hbar/m k_B T)^{1/2}$ is called the thermal wavelength with \hbar is Planck's constant and m is the mass of particle. For coexisting phases, the chemical potential and pressure are equal for thermodynamic and mechanical equilibrium. μ and Π are functions of $u(r)$, the interparticle potential. Often a phase diagram is represented as functions of volume fraction ϕ and dimensionless temperature $-k_B T/u_{\min}$. Theoretically $g(r)$ can be computed from $u(r)$ by virial expansions, integral equations, molecular dynamics simulations, and perturbation methods. The most common first-

order integral equation for short-range potentials is Percus-Yevick (PY) equation [31].

$$e^{u(\mathbf{r})/k_B T} g(\mathbf{r}) = 1 + n \int d\mathbf{r}' g(\mathbf{r}') [g(\mathbf{r} - \mathbf{r}') - 1] [1 - e^{u(\mathbf{r})/k_B T}] \quad (2.28)$$

In a very dilute limit ($n \rightarrow 0$), $g(r)$ and $u(r)$ have simple relationship

$$g(r) = e^{-u(r)/k_B T}. \quad (2.29)$$

Experimentally one often measures the scattering function of the system, instead of the correlation function. These two functions are Fourier transform (FT) of each other. In the weak scattering limit (Born approximation), the static scattered intensity is given by the following expression:

$$\begin{aligned} I(\mathbf{q}) &= \int d\mathbf{r}_1 d\mathbf{r}_2 e^{-i\mathbf{q}\cdot(\mathbf{r}_1 - \mathbf{r}_2)} \langle n(\mathbf{r}_1) n(\mathbf{r}_2) \rangle \\ &= \int d\mathbf{r}_1 e^{-i\mathbf{q}\cdot\mathbf{r}_1} n(\mathbf{r}_1) \int d\mathbf{r}_2 e^{i\mathbf{q}\cdot\mathbf{r}_2} n(\mathbf{r}_2) \\ &= \langle n(\mathbf{q}) n(-\mathbf{q}) \rangle \end{aligned} \quad (2.30)$$

where $n(\mathbf{q}) = \int d\mathbf{r} e^{-i\mathbf{q}\cdot\mathbf{r}} n(\mathbf{r}) = \sum_j e^{-i\mathbf{q}\cdot\mathbf{r}_j}$ is the Fourier transform the density function. The scattering measures the density-density correlation function. There are several commonly used functions related to density-density correlation function. The structure function $S(\mathbf{q})$ measures the density fluctuation $\delta n(\mathbf{r}) = n(\mathbf{r}) - \langle n \rangle$.

$$S(\mathbf{q}) = \frac{1}{V} \left[\int d\mathbf{r}_1 d\mathbf{r}_2 e^{-i\mathbf{q}\cdot(\mathbf{r}_1 - \mathbf{r}_2)} \langle \delta n(\mathbf{r}_1) \delta n(\mathbf{r}_2) \rangle + \left| \int d\mathbf{r} e^{-i\mathbf{q}\cdot\mathbf{r}} \langle n(\mathbf{r}) \rangle \right|^2 \right] \quad (2.31)$$

For isotropic, homogeneous fluids $S(\mathbf{q})$ and $g(\mathbf{r})$ is directly related as

$$S(\mathbf{q}) = \langle n \rangle \left[1 + \langle n \rangle \int d\mathbf{r} e^{-i\mathbf{q}\cdot\mathbf{r}} g(\mathbf{r}) \right]. \quad (2.32)$$

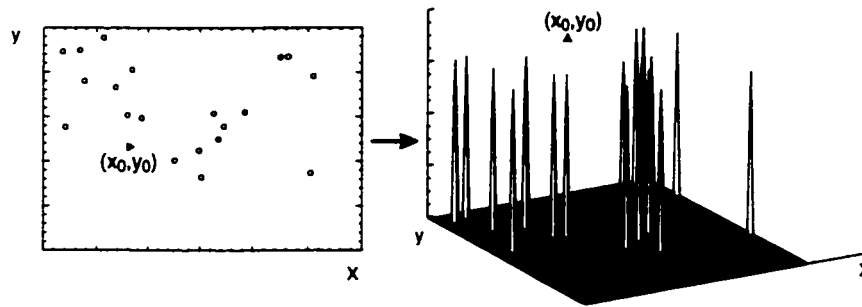


Figure 2.13: (a) shows a group of points of position (x_i, y_i) and (b) shows a surface plot of a two dimensional array with non-zero value at (x_i, y_i) .

They are Fourier transforms with respect to each other with the scaling and offset related to the average density $\langle n \rangle$.

It is convenient and fast to compute the Fourier transform of an image by built-in FFT function in the program. To reduce the artifacts due to finite size computation, it is important to have large number of data points in the system. Details in the discussion of computational FFT can be found in [62].

2.11 Bond-Orientational Order

Exotic phases have been discovered which lie between isotropic fluids and periodic crystals. More parameters are needed to distinguish different structures. The translational symmetry is measured by the correlation function or the structure function of particle positions \mathbf{r} as discussed above. A broken rotational symmetry can be measured by the correlations in the orientations of locally-defined crystallographic axis [63]. In contrast to conventional liquid crystals, the orientational anisotropy refers to

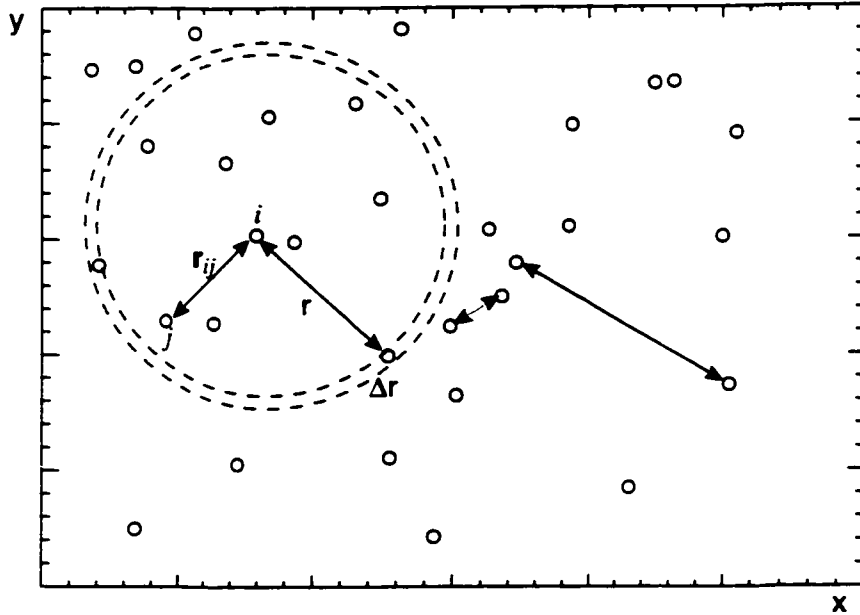


Figure 2.14: The scheme of calculating pair correlation function.

the “bonds” joining near-neighbor atoms, rather than an anisotropy in the constituent particles.

Bond-orientational order is an integral part of the two-dimensional melting theories. It is convenient to define a bond-orientational order parameter by designating $\theta(\mathbf{r})$ to be the angle between the local bond direction at position \mathbf{r} and some arbitrary reference axis. In a two-dimensional crystal with n -fold rotational symmetry, the bond-orientational order parameter is defined as

$$\Phi_n(\mathbf{r}_i) = \frac{1}{N_i} \sum_{j=1}^{N_i} e^{in\theta_{ij}(\mathbf{r})} \quad (2.33)$$

where the sum is over all neighbors j of particle i divided by the number of neighbors

N_i . $\Phi_n(\mathbf{r})$ is invariant under C_n rotation. $\Phi_n(\mathbf{r})$ has two parts: a magnitude, which is not related to the symmetry, but which is a measure of the degree of order, and a phase. The phase is the symmetry breaking parameter. The bond-orientational correlation function can be calculated as

$$g_n(r) = \langle \Phi_n(r) \Phi_n^*(0) \rangle. \quad (2.34)$$

Given a density distribution function $n(\mathbf{r})$, Φ_n can be computed through different schemes. First is to identify the neighbors. We can also use “metric neighbors” by finding all the particles within certain separation from one particles. We employ the Delaunay triangulation to find “geometric neighbors” and thus $\theta_{ij}(r)$. It has generally been found that the global properties of Φ_n are insensitive to the definition of “neighbors”. We can also use the edges of the Voronoi cell as “bonds”. The Voronoi diagram is the dual of the Delaunay triangulation. The results of these two methods come out identical. Fig. 2.15 illustrates two approaches. It saves programming and computation time to find the neighbors by Delaunay triangulation or Voronoi diagram because they are well-solved problems in computational geometry. For 2D analysis there are built-in programs in IDL. For 3D analysis, there is freeware *qhull* available².

In two dimensions, the most used global bond-orientational order parameter Φ_6 is

$$\Phi_6 = \left| \frac{1}{N_{\text{bond}}} \sum_i \sum_j e^{i6\theta_{ij}} \right|. \quad (2.35)$$

²Download and instruction website <http://www.geom.umn.edu/~bradb>.

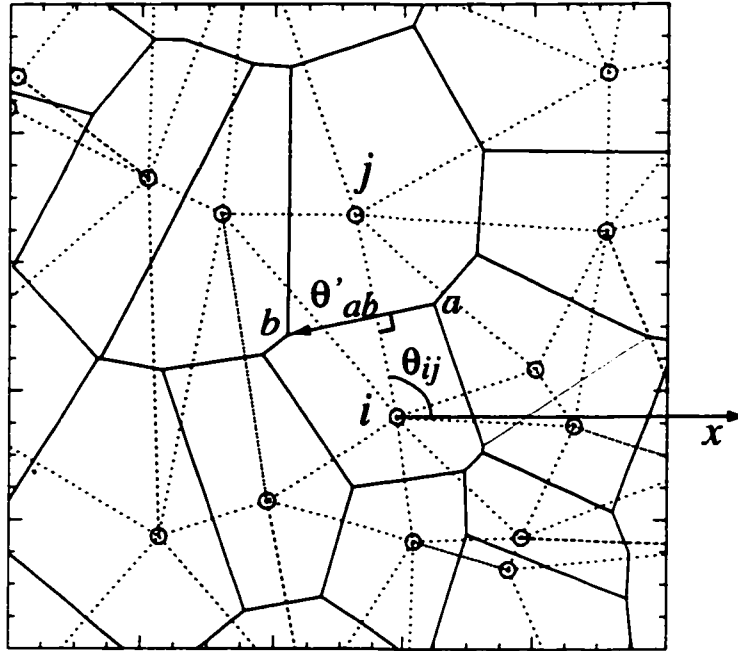


Figure 2.15: A voronoi cell of point i are generated by the bisectors of points i and all other points. If one draws a line between any two points whose voronoi domains touch, a set of triangles is obtained, known as the Delaunay triangulation. The number of edges is the same as the number of triangulation bonds r_{ij} . We can choose the angle θ_{ij} between the bond r_{ij} to a reference axis, say x -axis or the angle θ'_{ij} between edge \overline{ab} to the reference axis because $|\theta - \theta'| = 90^\circ$.

where i runs over all the particles in the systems and j runs over all neighbors of the particle i and N_{bond} is total number of the bonds between i and j . Φ_6 measures the coherence of sixfold symmetry in the system, which is characteristic of hexagonal closed-packed state (HCP) in two dimensions. For a perfect HCP lattice $\Phi_6 = 1$ while $\Phi_6 \sim N_{\text{bond}}^{-1/2}$ for an ideal gas [64].

In three dimensions, the orientational order parameters are generalization of the two-dimensional order parameter [63]. The analysis first associates a set of spherical harmonics with every bond joining the particle i to its neighbors.

$$Q_{lm}(i) = \frac{1}{N_i} \sum_{j=1}^{N_i} Y_{lm}(\theta(\mathbf{r}_{ij}), \phi(\mathbf{r}_{ij})) \quad (2.36)$$

where $Y_{lm}(\theta, \phi)$ are spherical harmonics, \mathbf{r}_{ij} is the direction of the bond with $\theta(\mathbf{r}_{ij})$, $\phi(\mathbf{r}_{ij})$ with respect to a reference coordinate system and N_i is the total number of neighbors of particle i . In Steinhardt *et. al.* analysis they found important parameters which should be orientationally invariant to identify the crystalline symmetry as “shape spectroscopy” [63]. For example Q_4 is the “finger print” for crystals with cubic symmetry and Q_6 for icosahedral oriented systems where the second order invariant Q_n is defined as

$$Q_l = \left[\frac{4\pi}{2l+1} \sum_{m=-l}^{m=l} |\bar{Q}_{lm}^2| \right]^{1/2} \quad (2.37)$$

where \bar{Q}_{lm} is the global average quantity. The third-order invariant W_l is defined as

$$W_l = \sum_{\substack{m_1, m_2, m_3 \\ m_1 + m_2 + m_3 = 0}} \begin{pmatrix} l & l & l \\ m_1 & m_2 & m_3 \end{pmatrix} \times \bar{Q}_{lm_1} \bar{Q}_{lm_2} \bar{Q}_{lm_3} \quad (2.38)$$

where $(:::)$ stands for a Wigner $3j$ symbol. W_4 is sensitive to distinguish bcc structure from fcc and hcp. In the recent experiment by Gasser *et. al.* [65] they used Q_4 , Q_6 and W_6 to identify the nucleation cluster in the weakly charged sphere systems.

2.12 Colloidal Suspensions in Confined Geometries

The nature of the melting transition in two-dimensional systems has been a matter of great interest and often hot controversy since nearly 30 years ago. As the dimensionality of space is reduced, the fluctuations around mean-field behavior become more pronounced and destroy the long-range periodicity of a two-dimensional lattice at finite temperatures. 2D solids exhibit quasi-long-range translational order, characterized by a power law decay of the positional correlation function and long-range bond orientational order while 2D liquids exhibit short-range order where the order parameter correlation functions decay exponentially. The melting transition is through an intermediate hexatic phase with short-range translational order and quasi-long-range bond orientational order. The two-dimensional melting mechanism is summarized by Kosterlitz, Thouless, Halperin, Nelson and Young (KTHNY) [13, 14, 15, 16]. Accord-

ing to KTHNY theory, 2D solids melt via 2 sequential continuous phase transitions mediated by topological defects. The first transition from a 2D solid to a hexatic phase is driven by the dissociation of topological defects, i.e., bound dislocation pairs in the solid. The second transition from hexatic phase to 2D liquid is caused by dissociation of individual dislocations to form disclinations.

Enclosing a colloidal suspension between two smooth parallel walls that repel colloidal particles in the spacings of a few particle diameters is a straightforward method for creating a two-dimensional layer of colloids. The systems have been proven convenient model systems for experimental and theoretical studies [66, 67, 68]. Recently there are exciting developments in both experiments on 2D freezing/melting by the presence of a 1D periodic potential [69, 70]. It is denoted as laser-induced freezing by subjecting a 2D colloidal suspension to a one-dimensional potential made by the standing wave pattern of two interfering laser beams. When the periodicity of the light pattern is commensurate with the mean particle separation, the colloidal liquid freezes into a solid at certain light intensity strength. Theoretical models find novel phases such as “modulated liquids”, “floating-solid”, “locked-floating-solid” and 2D smectic phases [71, 72, 73, 74, 75]. The topology of phase diagram depends on the relative orientation of 2D crystal to the periodic potential troughs which selects a set of Bragg planes running parallel to the troughs and the commensurability ratio $p = a'/d$ of the spacing a' between these Bragg planes to the period d of the periodic

potential [74, 75]. The 2D-melting scenario proposed by KTHNY is affected by the presence of a periodic 1D potential. As the strength of the potential increases, a 2D liquid first crystallizes in hexagonal order and then melts again to a modulated liquid. This shows that the particle fluctuations suppressed by optical potentials are essential to the nature of phase transitions.

2.13 Surface Freezing On Patterned Substrates

Recently Heni and Löwen considered the phases of a hard sphere suspensions near topologically patterned walls corresponding to FCC lattice cut along the (111), (100) or (110) orientation, a HCP (100) orientation and a rhombic lattice distorted with respect to the triangular one. They derived the scaling relations for thickness of crystal based on the phenomenological theory of the hard sphere fluid in contact with wall; the fluid may “condense” into “droplet of crystals” on the patterned walls. They confirmed their phenomenological theoretical results by computer simulations. The theoretical substrate was composed of fixed hard spheres forming a periodic two dimensional array and the fluid was composed as hard spheres of the same diameter as the fixed wall spheres. By computer simulation, they found that a pattern which is commensurate with the bulk crystal can initiate complete precrystallization with an onset far away from the bulk freezing transitions and the complete and incomplete wetting depends on the type of the surface patterns. For instance, fcc(111) produced

complete wetting while fcc(100) and (110) gave incomplete wetting. When there are distortions of lattice mismatch between bulk phases and the substrate, the wetting can be either incomplete or prevented.

The phenomenological theory is similar to the theory of wetting. They computed the difference Σ of the grand canonical free energies per unit area for a wetting and a non-wetting situation. This quantity is discussed as a function of system parameters and a crystalline sheet of thickness ℓ (see Fig.2.16). Σ is contributed from bulk/surface thermodynamics, and effective interface interactions and elastic distortions of the solid [76]

$$\Sigma = \Sigma_1 + \Sigma_2 + \Sigma_3. \quad (2.39)$$

The first term is the surface tensions γ_{ws} , γ_{wf} and γ_{sf} of three interfaces wall-solid, solid-fluid, and patterned wall-fluid

$$\Sigma_1 = \gamma_{ws} + \gamma_{sf} - \gamma_{wf} \quad (2.40)$$

which determines the wetting of the phases. A necessary condition for wetting to occur is $\Sigma_1 \leq 0$. γ_{ws} and γ_{sf} depend on the wall pattern. γ_{sf} depends on the relative orientation of the planar solid phase with respect to the fluid and have been calculated for hard spheres by computer simulation in different orientations [77].

The second term describes the energy of the bulk crystalline layers. The adjacent crystalline layers are taken to have exactly the same structures as the wall patterns and exhibit no spontaneous shearing. The coexistence bulk crystal favors the square

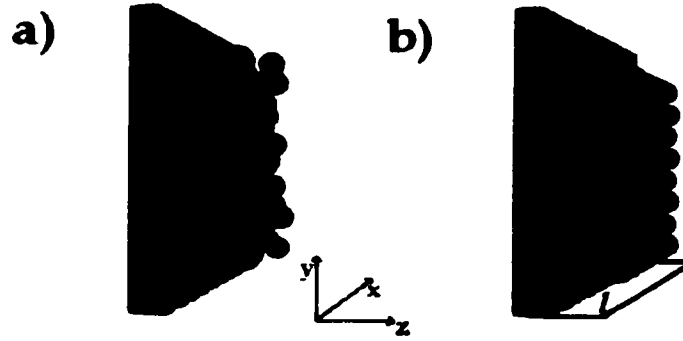


Figure 2.16: Schematic drawing from [2] of a hard sphere fluid in contact with a patterned wall. It can either just flow around the structure forming an inhomogeneous fluid (a) or form a crystalline layer of thickness ℓ following the structure imprinted on the surface (b).

lattice constant $a_{\square} \equiv 1.1075\sigma$ (σ is the hard sphere diameter). If the square wall pattern of lattice spacing $a \neq a_{\square}$ is incommensurate with the coexistent bulk crystal, it causes a strain ϵ

$$\epsilon = \sqrt{2} \frac{a - a_{\square}}{a_{\square}}. \quad (2.41)$$

which describes the relative distortion. The free energy penalty $\Sigma_2(\ell)$ from small distortion ϵ can be calculated as an expansion of the energy around the coexisting bulk crystal by harmonic elasticity theory [78], i.e.,

$$\Sigma_2(\ell) = \beta\epsilon^2\ell \quad (2.42)$$

β can be expressed in terms of the elastic constants of crystals C_{ij} . For an FCC crystal of hard spheres, C_{ij} has been calculated at different densities including melting point [79]. The elastic energy can be re-expressed as

$$\Sigma_2(\ell) = \alpha\Delta\Pi\ell \quad (2.43)$$

where $\alpha = (\phi_s - \phi_f)/\phi_f = 0.103$ is the relative density jump between solid and fluid at the bulk freezing point and $\Delta\Pi = \Pi_c - \Pi$ is the difference between the bulk equilibrium fluid pressure P and the bulk pressure P_c at coexistence.

The third term is the effective interface interaction Σ_3 which can be from long range interaction such as the van der Waals interaction or the gravitational force between wall and fluid between the wall-solid and the solid-fluid interface as a function of their average distance ℓ [80].

$$\Sigma_3 = \gamma_0 e^{-\ell/\ell_0} \quad (2.44)$$

where γ_0 is a prefactor and ℓ_0 is the correlation length in the bulk solid at fluid coexistence.

Putting 2.40-2.44 to 2.39, we have

$$\Sigma(\ell) = \gamma_{ws} + \gamma_{sf} - \gamma_{wf} + \alpha\Delta P\ell + \gamma_0 \exp(-\ell/\ell_0). \quad (2.45)$$

Minimizing Σ with respect to ℓ yields the equilibrium profile and the authors found the following scaling relations which no longer depend on interfacial free energies near the coexistence: (i) when $\epsilon \rightarrow 0$ and there is complete wetting, the thickness ℓ diverges logarithmically with ΔP . (ii) For $\epsilon \neq 0$, there is incomplete wetting and the maximal thickness which is achieved at $\Delta P = 0$ varies logarithmically with ϵ^2 . (iii) For a stretched or shrunken lattice, the lowest possible prefreezing pressure can be calculated. They will have a *lower* prefreezing pressure at slightly expanded lattice.

In their simulations, they use bond order parameters (Φ_2 , Φ_4 and Φ_6) to detect layerwise precrystallization. For the triangular patterns, Φ_6 is used and for square patterns Φ_4 is used. For FCC(110) and HCP(110) patterns Φ_2 is applied. The density profile $n(z)$ is defined as

$$n(z) = \int_{-\infty}^{\infty} \int_{-\infty}^{\infty} dx dy n(x, y, z) \quad (2.46)$$

where $n(x, y, z)$ is the density function. The minima of $n(z)$ define the spacing of the n th layers in the z -direction. The analysis of an order parameter in the n th layer is performed for all the particles of a chosen layer.

Based on theoretical prediction on hard sphere fluid near FCC(100) wall, the growth of the wetting layer saturates at 3.9σ as the volume fraction approaches to 54.5% and the lowest prefreezing volume fraction is 42% in the expanded lattice. When ϵ is larger than the critical distortion $\epsilon_c = 0.09$, the large free energy cost of elastic distortion prevents the system from surface freezing.

2.14 Roughness

In the Heni and Löwen simulations, they do not address the roughness of the solids and the commensurate-incommensurate transition. Both are important issues in crystal growth. The roughness is important to determine the growth rate, growth sites and surface relaxation. Kinetic roughening is still an on-going fascinating research subject which describes the stochastic surface growth. The real-time investigation

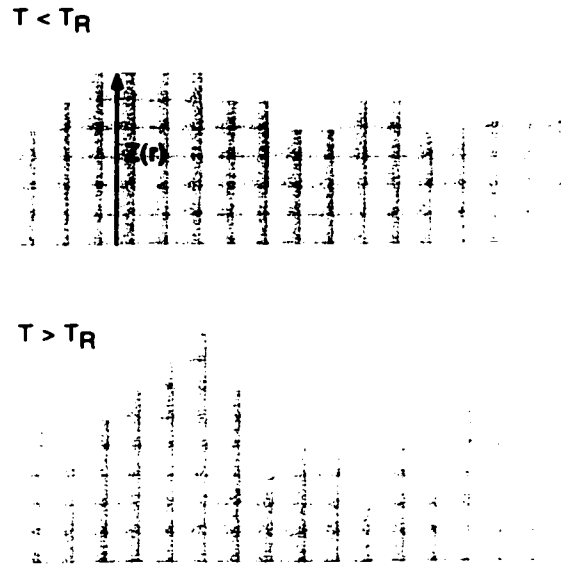


Figure 2.17: Roughening transition (a) $T < T_R$ and (b) $T > T_R$

in colloidal systems makes the measurement of scaling exponents of roughness possible. In a recent experiment [81] investigating the dynamic scaling of roughness of crystals by sedimenting SiO_2 nanospheres and concluded the interface growth close to equilibrium.

The roughness can be characterized by height-height correlation function

$$G(\mathbf{R}) = \langle |z(\mathbf{r}) - z(\mathbf{r} + \mathbf{R})|^2 \rangle \quad (2.47)$$

where $\mathbf{R} = (x, y)$ is a point of the two-dimensional (x, y) space and z is the height as a function of (x, y) . There is a roughening transition. At low temperature the surface would like to be smooth. At high temperature there are more and more fluctuation of surface. The nature of this transition can be understood from two competition term in free energy $F = U - TS$. A step cost some finite energy W but a step is also

favorable to increase the system's entropy. Thus below the roughening temperature T_R it takes work to introduce a step into the surface while above T_R it takes work to remove steps from the surface. The interest of this function is that qualitatively different behaviors occurs above and below T_R

$$\begin{aligned} \lim_{R \rightarrow \infty} G(R) &\sim 2K(T) \ln \xi, \quad T < T_R \\ &\sim 2K(T) \ln R, \quad T > T_R \end{aligned} \quad (2.48)$$

where ξ is the correlation length for $G(R)$. It is finite below T_R and divergent above T_R . The coefficient $K(T)$ behaves in a characteristic way for Korsterlitz-Thouless (KT) transition [82]. Above T_R the discreteness of crystal lattice become negligible, the surface free energy is proportional to the surface area. If we include the effect of gravity, the free energy \mathcal{F} associated with surface shape fluctuation is

$$\mathcal{F} = -\frac{1}{2} \int \int dx dy \left[\Delta d g z^2 + \gamma(z_x^2 + z_y^2) \right] \quad (2.49)$$

where γ is surface tension, Δd is the density difference between the particle and the solution and $z_\alpha = \partial z / \partial x_\alpha$. From equipartition theorem, the correlation function $G(R)$ can be expressed as

$$G(R) \approx \int_{1/R}^{1/a} dq 2\pi q \frac{2k_B T}{\Delta d g + \gamma q^2} \quad (2.50)$$

where a is the lattice spacing of the crystal. From Eq. 2.50, gravity can kill the roughening transition. If the length $1/q$ is shorter than the capillary length λ

$$\lambda = \sqrt{\gamma / \Delta d g}, \quad (2.51)$$

the role of gravity is negligible. In colloidal systems γ is of order $k_B T$ per particle. The resulting value of λ is of microns. The roughness of an equilibrium surface between fluid/solid interface is more significant under microgravity.

2.15 Commensurate-Incommensurate Transitions

When particles nucleates into a crystal on a foreign substrate at equilibrium, there are two competing effects. There is a favored bulk interparticle separation a determined by interparticle interaction. The particle-substrate interaction forces the particles to the lattice parameter of the substrate b . For a given lattice misfit, if the particle-substrate interaction is strong, the commensurate structure ($a = b$) is stable while the incommensurate structure ($a \neq b$) is stabilized by strong interparticle interaction (See Fig. 2.18a and b).

It is also possible that the first monolayer is commensurate and become incommensurate when the number h of layer become larger. When h becomes large, the structure becomes incommensurate at equilibrium. The energy gain from the structure into preferred distance a is proportional to the layer volume and eventually overcomes the energy loss due to giving up commensuration. The appearance of the incommensurate structure requires the introduction of *misfit dislocations* (See Fig. 2.18c).

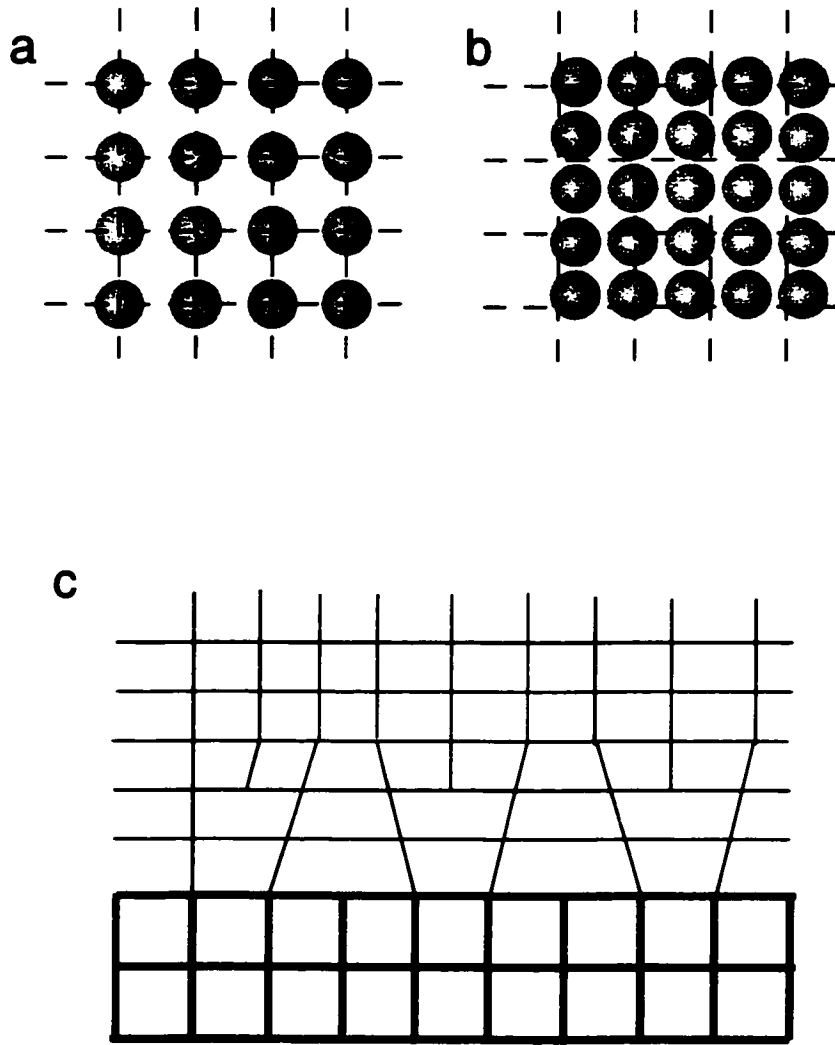


Figure 2.18: (a) commensurate structure of particles on a square lattice. (b) incommensurate structure. (c) schematic drawing of misfit dislocations. Lines represent lattice planes. Thick lines are for substrate lattice planes and thin lines for the adsorbate ones.

Chapter 3

Experimental Methods

In this Chapter we discuss experimental procedures relevant to all the experiments. We discuss (i) the suspensions of colloidal spheres commonly used in the lab [83]; (ii) how to manufacture grating-assisted imprints and sample chambers for template-directed colloidal crystallization experiments; (iii) video optical microscopy and laser tweezers which are our main measurement tools; and (iv) fd virus preparation and properties.

3.1 Polystyrene Spheres

The most common commercially available model colloidal system is an aqueous suspension of polystyrene spheres. Polystyrene spheres are accurately spherical and generally monodisperse. They are also available in a large range of sizes and they can be made to fluoresce. The density of polystyrene spheres is 1.05 g/cc and the index of refraction is 1.59. It is easy to density match polystyrene particles with heavy water; however, its high index of refraction makes it extremely difficult to observe bulk struc-

ture of suspensions at high number density. So far we have not found a reliable way to stabilize polystyrene particles in organic solvents. The particles are composed of a large number of linear polystyrene molecules associated with hydrophilic groups such as sulphate groups ($-\text{SO}_4$), carboxylate group ($-\text{COOH}$) or amine group ($-\text{NH}_4$). These end groups ionize in water (or other polar liquids), releasing counterions, usually H^+ and the particles become negatively charged and stabilized. The electrostatic interaction between these particles can be controlled by the solution's ionic strength, which determines the inverse Debye length $1/\kappa$. It is possible to have extremely long screening length by adding the ion exchange resins, which scavenge excess ions. By adding extra electrolyte, it is possible to decrease the screening length to a few nm so that the particles act as hard spheres. The practical way to calculate the screening length is through the relationship

$$\frac{1}{\kappa} = \frac{0.43}{\sqrt{\sum z_i^2 [\text{Salt}]}} \text{ nm} \quad (3.1)$$

where z_i is the charge valence and $[\text{Salt}]$ is salt concentration in M. Thus for 10 mM NaCl the screening length $1/\kappa$ is 3 nm. The proteins can be attached onto polystyrene spheres through standard biochemistry technique which can be useful for probing bio-microsystems.

3.2 Silica Spheres

Colloidal silica particles are charge stabilized, but can be dispersed in a variety of organic solvents. The density of silica spheres is high, ranging from 1.5 to 1.9 g/cc and the refractive index ranges from 1.45 to 1.49. The variety is attributed to particle porosity. The particles can be well index matched in aqueous solution by adding glycerin. There are no commercially available fluorescent silica particles but there are core-shell fluorescence silica particles developed by the Netherland group [84]. The silica spheres can endure more chemical processing. Very often the silica colloidal crystals are used as a template for imbibing different materials to manufacture photonic crystals. In our lab, the most common use for silica spheres is as probing particles in the interaction measurement in the line tweezers. The lower index of refraction makes it favored to stay in the line scanned optical tweezers while the polystyrene particles are often kicked out probably due to the distortions of the trapping beam.

3.3 Polymethylmethacrylate Spheres

We have used polymethylmethacrylate (PMMA) spheres stabilized by a grafted layer of poly-12-hydroxystearic acid (PHSA) [85, 86] for our colloidal assembly studies. Because they can be index matched by choosing appropriate solvents, these particles facilitates optical microscopy in order to look deep into the sample, even at high concentrations. These particles are not commercially available. They were synthesized

and provided by Andrew Schofield (abs@ph.ed.ac.uk). The particle density was about 1.19 g/cc, and the index of refraction was about 1.49. The colloids come in dodecane, and sometimes have yellowish impurity. To clean the particles, Andrew suggested filtration through glass wool to remove the impurity. Normally we redispersed them in the desired solvent, centrifuge them few times and then extract the clean beads from the top. These PMMA particles have been studied extensively as a colloidal model system of nearly hard spheres [83]. However, some solvents may alter the properties of the colloids, e.g. by charging the particles.

3.3.1 Fluorescence Labelled PMMA Particles

In order to be observed in the confocal microscope, the PMMA particles were fluorescence labelled with rhodamine 590 ($C_{28}H_{30}N_2O_3$, Aldrich No. R4127). This recipe was first developed by Andrew Levitt. The PMMA particles were first swollen in the solvents (cyclohexanone and ethanol¹) with fluorescence dissolved. The fluorescence dye is a hydrophobic molecule which can be adsorbed onto PMMA. The particles were redispersed into the solvent which fluorescence dye is insoluble to. Thus the fluorescence dye is “trapped” inside PMMA core and increases the size and density of particles by few percent.

We start with clean colloids in dodecane at 10- 20% in volume fraction and add the fluorescence solution by the half amount of original colloidal solution volume. The

¹Acetone in the original protocol.

fluorescence solution is prepared by dissolving rhodamine 590 in 25% ethanol/75% cyclohexanone mixture at the concentration of 1-1.5 mg/ml. Initially the dyed mixtures look purple but turn orangish after shaking it for 5 - 10 minutes which indicates the inclusion of fluorescence molecules to the core of particles. We also double check the complete dye incorporation into colloids by fluorescence microscopy. The fluorescent solvent is removed after centrifuging the suspensions for 10 minutes at 2000 RPM. Afterwards, the colloids are washed by repeatedly dispersing colloids in fresh decalin and centrifuging them. In the first few runs it is difficult to redisperse the particles in decalin. We need to vortex the solution very hard for a long time in order to break the large lump of colloidal aggregation. The repeated decalin wash is to ensure no excess fluorescence and no other solvents (dodecane, cyclohexanone, ..etc.) stayed in the colloids. After this stage, we can start index-matching or density-matching with the desired solvent. The resulting spheres can be seen using FITC and rhodamine. The fluorescence particles are less stabilized however. For example, they aggregate into gel-like structure in dodecane where the non-fluorescence particles are stable. At higher concentration of added polymers the particles aggregate irreversibly easily compared with the non-fluorescing particles. The swelling process may destroy some steric PHSA layer and weaken the stabilization between particles. They are not exactly hard sphere like. The particles may act like charged particles under some conditions.

3.3.2 Solvents for PMMA particles

A variety of mixtures of organic solvents have been used for density matching and index matching the particles. In order to have density 1.19 g/cc, the organic compounds usually contain halogen molecules, amine or carboxylate groups. But amine or carboxyl groups usually gives higher index refraction (> 1.55). Solvents may change the physical properties of colloids significantly. The complication from the chemistry due to solvents make the systems hard to control. This is still under the investigation of various groups. The solvents used in the literature are decalin ($C_{10}H_{18}$), tetralin ($C_{10}H_{12}$), carbon disulfide (CS_2), cycloheptyl bromide ($C_7H_{13}Br$), and carbon tetrachloride (CCl_4). We also tried cyclohepxyl bromide ($C_6H_{11}Br$), tetrachloroethylen (C_2Cl_4) and few other organic solvents. Table 3.1 summarizes the density d and the index of refraction n of different solvents. It was first reported that CS_2 penetrates the PMMA core [87] resulting in a slight increase ($\sim 3\%$) in the radii. We observe similar phenomena with various solvents. The penetration is usually complete within a few hours to a few days after being dispersed in the new solvent and it can be accelerated by heating at $50 - 70^\circ C^2$. The imbibing also changes particle's density and index refraction slightly. We observed the swelling effect by sedimenting particles into crystals at different solvents (the density mismatch > 0.1 g/cc). After a few days, the sedimented crystals should have volume fraction close to 74% for hard-sphere like

²Private communication with Russel group at Princeton

Chemical Formula	Density (d)	Index of Refraction (n)
$C_{10}H_{18}$	0.896	1.475
$C_{10}H_{12}$	0.973	1.541
CS_2	1.266	1.627
$C_7H_{13}Br$	1.289	1.505
CCl_4	1.594	1.46
C_2Cl_4	1.623	1.504
$C_6H_{11}Br$	1.324	1.495

Table 3.1: Common Chemical Solvents Used for PMMA particles

particles. We calculate the hard-sphere diameter from the interparticle separation shown in Table 3.2.

A more serious effect on the particles from the solvents is the possible charging effect which renders the particles not hard-sphere-like. The surface of PMMA beads contains PHSA which contains carboxylate group, it may ionize in the polar solvents. This may also explain why rhodamine-dyed particles are more likely to be charged from $-Cl$. Originally we used cycloheptyl bromide (CHB) and cyclohexyl bromide (CXB). But both swelling and charging effects are quite prominent in the dyed particle systems. Molecules with high symmetry are more desirable because they are less polar. CS_2 and CCl_4 are highly toxic and volatile. tetrachloroethylene (TTC)

Particles	Solvents	Particle Diameter (μm)
NF	dodecane	1.30
NF	dec & TTC	1.32
NF	dec & CHB	1.38
NF	dec & CXB	1.39
F	dec	1.39
F	dec & TTC	1.40
F	dec & CHB	1.46
F	dec & CXB	1.484

Table 3.2: Swelling Diameters in Different Solvents

Particle	Solvents	Freezing Point
NF	decalin, tetralin & TTC	45-50 %
F	decalin, tetralin & TTC	45-50 %
F	decalin & CHB	30-40 %
F	decalin & CXB	30-40 %

Table 3.3: Freezing Point of PMMA Particles at Different Solvents

which is commonly used in dry clean industry appears suitable. We measured the freezing transition points between fluorescence (F) and non-fluorescence (NF) PMMA particles at different solvents to determine the charging effect. The electrostatic repulsion between particles lowers the freezing-melting transition point. The result is summarized in Table 3.3.2. The phase behaviors of fluorescence particles with added polymer in decalin/tetralin/TTC is more similar to non-fluorescence particles than fluorescence particles in dec/CHB and dec/CXB.

Tetrachloroethylene (TTC) may dissolve epoxies which are used to seal the chambers and the optical glue for templates. The problem becomes more serious in the thick chambers. The colloids aggregate throughout the whole sample. There should be no contact between the epoxy and solvents before it is fully cured. All the templates should be left overnight after its first cure.

Overall the mixture of decalin, tetralin and tetrachloroethylene gives more consistent results. Sometimes the chemistry also depends on the original batch in dodecane. We found some non-fluorescence particles with strong electrostatic repulsion in dodecane. Moreover, even within the same sample the electrostatic repulsion between different pairs can be quite different. de Hoog completed a thorough investigation of fluorescent PMMA particles suspended in various solvent for use in CSLM [88]. They found that water moisture contained in the solvents affects the charging of particles. They applied an electric field to PMMA particles in 96% CHB and found out the particles were positive charged. Their explanation is that halogen-carbon bonding can dissociate in the presence of water which will lead to a substitution of the halogen with a hydroxyl group and the formation of a proton and halogen ion. The proton can protonate ester groups of PMMA particles which give positively charged PMMA-particles. In the control sample with distilled and purified CHB, the obvious repulsive interaction between particles disappear. This may account for the poor reproducibility of the systems and the inconsistent phase behaviors from one batch to another. To produce more reliable results, we must develop better understanding of the chemical issues.

Throughout the sample preparations for experimental studies, the weights of various components (particles, solvents, polymer etc.) are accurately measured. However, the quantity of interest in analyzing experiments is the volume fraction ϕ . The

imbibed solvents can change the density of PMMA particles. We determine the density of particles by centrifuging the particles in different solvent density. In the dec/tetra/TTC fluorescent PMMA particle density is between 1.245 – 1.25 g/cc. After measuring the particle density, we lower the density of solvent slightly, centrifuge down the particles and remove excess solvent by placing the vial upside down about 1 minute. At this stage, the particles are randomly close packed with volume fraction $\phi = 0.66$ of amorphous sediment formed by centrifuging samples [83]. A more precise way to determine the volume fraction may be to perform viscosity measurement of dilute suspensions through Einstein relation:

$$\eta = \eta_0 (1 + 2.5 \phi + \dots) \quad (3.2)$$

where η_0 is the viscosity of the suspension medium. However, reliable extrapolation to high concentrations requires extremely accurate measurements with temperature control and also it assumes that particles are hard-sphere like. Most samples of our interests are prepared in high concentration ($\phi = 40\%$) and through drying process and other modification of the systems, the particles may not be hard-sphere like.

3.4 Template-Directed Colloidal Assembly

Colloids can self-assemble into a wide range of highly ordered phases [60, 89, 90, 37, 91]. Experimentally it is known that hard-sphere-like colloids generally crystallize with a random stacking of close packed planes [92, 93, 94]. Theoretically the free

energy difference between fcc, hcp or rhcp are of the order of $10^{-3} k_B T$ per particle [95]. Colloidal crystals can also be induced by external force such as gravitational [96], convective [97, 98, 99, 100, 101], and electrohydrodynamic [102] forces. However, many schemes with external force involve layer by layer growth. Naturally in 2D the most close packed patterns are hexagonal structure which allow two possible nucleation sites. Thus there is no single crystal formed.

The pioneering work by van Blaaderen, Ruel and Wiltzius [96] apply the idea from molecular beam epitaxy by growing single crystalline on an oriented crystal facet. They construct a pattern of holes commensurate with the 100 plane of fcc crystals by e-beam lithography. They found a pure fcc single crystals formed. The crystal extended to hundreds of layer thick and as large as the template size. The combination of patterned surface with external field induced crystallization has become a new paradigm in the field of colloidal assembly.

E-beam lithography advanced the microelectronic industry. The resolution can achieve as small as 50 nm. However, there are many practical factors to limit e-beam assisted templates widely available. First e-beam lithography machine is very costly. Second writing large areas of patterns takes a long time. Third to generate the patterns with large holes in small separation the proximity effect becomes serious. With the SEM at Johnson's lab, we were not able to produce the same patterns in van Blaaderen's work.

3.4.1 Imprint with Gratings

Imprint or stamping techniques provide a simple way to make replicas of surface structures [103]. It has also been demonstrated to produce features as small as 10 nm, [104] but one still needs a mold made by photolithography or e-beam lithography. We use commercially available optical gratings as molds to avoid the difficulties of generating closely spacing features ($< 1 \mu\text{m}$) by conventional lithography. We have therefore employed the imprint technique with an optical diffraction grating to create a geometrical template. We choose a ruled grating with big blaze angle. There are also holographic gratings with shapes like sinusoidal profiles. The smallest pitch on commercial catalog is $0.2 \mu\text{m}$. Few companies take order for custom-made ruled gratings³. The commercially bought gratings are actually replica gratings whose grooves are formed in a very thin layer of resin adhering strongly to the surface of substrate material. For reflection replica the surface is usually coated with aluminum, gold or platinum. The grating making process itself is an imprint process. The master gratings are ruled on well-annealed substrate like BK-7 optical glass, fused silica, or aluminum with optical flatness of $\lambda/10$. The ruling process is a long, slow and grueling process which takes up to a week. Special attention is paid to the change in temperature, pressure and the isolation from vibrations. After the master grating is done, the replication process starts with submaster grating which is directly repli-

³Diffraction Products, (815)338-6768. Optometrics USA (978)772-1700.

cated from the master grating. A parting agent which helps the separation of replica gratings is added onto the submaster grating and then a layer of reflective coating is applied. A thin layer of liquid resin is sandwiched between the the submaster groove and the substrate and cured fully to harden the resin with the groove profile replicated faithfully. After separation the replica grating is identical to the original master grating. Because these are industrial process, we are not able to find the recipe of applying parting agents which is very useful in developing imprint technique.

There are mainly two ways of making imprint and we used both schemes for different kinds of template. The first method we employed was developed by Chou *et al.* [104]. We called it thermal imprint. The idea is to replicate structure on a thermoplastic. Thermoplastic is linear polymer and when it is heated above glass temperature, it becomes liquid like and readily deformed. A mold is pushed onto thermoplastic with some pressure. The plastic is removed from the mold after cooling down and it becomes the replica of the mold (Fig. 3.1). In the first generation of template, we used PMMA spin-coated on a glass substrate as the themoplastic. The thickness of PMMA can be controlled by the PMMA solution concentration and the molecular weight and spin speed ⁴. A trace amount of pyrromethene 580 is sometimes added into PMMA solution to inspect the template by fluorescence microscopy. Heat PMMA above its glass temperature of $\approx 100^{\circ}\text{C}$, creates a replica of the grating in

⁴PMMA solution is purchased from Microchem Corp. 617-965-5511

Imprint Scheme

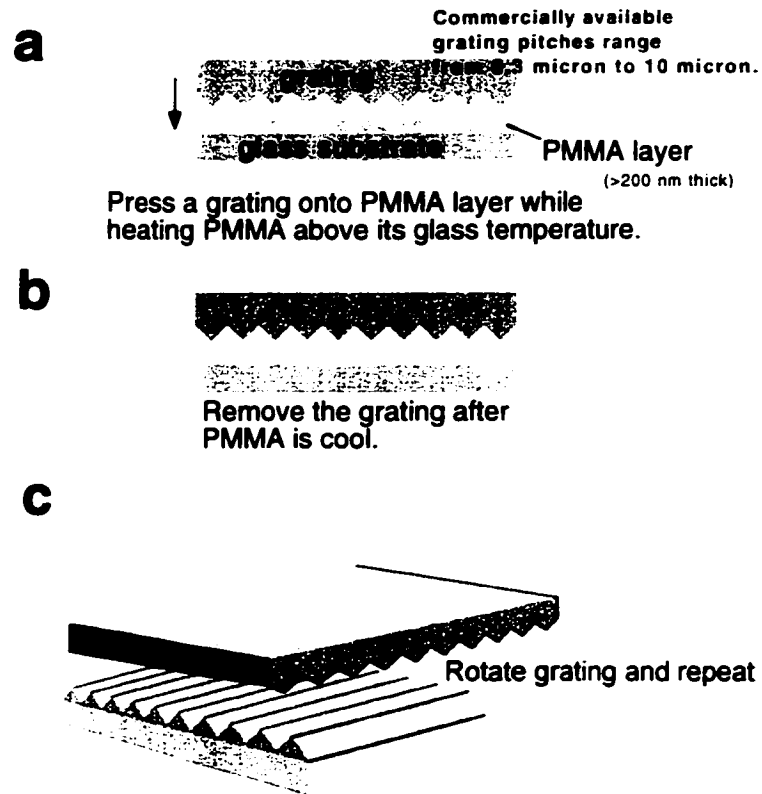


Figure 3.1: The schematics of thermal imprint.

the film (Fig. 3.2A). By rotating the substrate 90° and imprinting a second time, we create two-dimensional periodic structures, resembling an array of square pyramids (Fig. 3.2B). One problem of thermal imprint is that the heat destroys grating which is made out of epoxy. The epoxy starts to degrade above 70 degree. On the average an original optical grating can be used 10 – 20 times.

The second method of imprint was developed by Whitesides' group [103]. The basic idea is to crosslink liquid monomer or polymer on the mold. Once it is crosslinked,

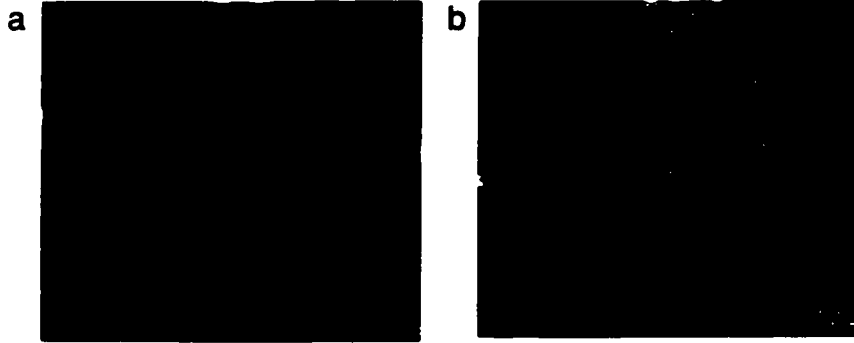


Figure 3.2: AFM scan of (a) line grating template and (b) crossed grating template.

it becomes solid like. The drawback of this technique is that we cannot imprint twice at different direction. The advantage is that it has higher fidelity to the mold and it does not destroy the mold. But separating the mold from the crosslinked polymer can be tricky. I have tried few polymers. The elastomeric PDMS (polydimethylsiloxane) is the most popular materials for imprint. We use the two component Sylgard 184 developed by Dow Corning ⁵. Silanizing the mold with hexamethyldisilazane (HDMS) or fluorosilane will help the release of the mold. This treatment turns active $-OH$ group on the mold into inert $-CH_3$ or $-CF_3$ so that the cast polymer does not adhere to the mold. However, PDMS is swollen by hydrocarbons so it can not be used for the organic PMMA systems. Also it is very hydrophobic: thus in order to use it for aqueous systems, the surface must be oxidized by oxygen plasma. The surface polymer with $-Si-$ becomes hydrophilic $-SiO_2$. However, excess oxidization process can destroy the surface pattern. The surface treatment can also be achieved by

⁵From the distributor Essex 1-800-805-4636.

sputtering a thin layer of metal like gold or reacted with halogen acid [105].

We also used optical glue as cast polymer. Two advantages to use optical glue: first, curing by UV is fast. Usually it is set within few seconds radiated by UV and fully cured after a day; second, our molds are usually made out of thermoplastic and they can be destroyed by high temperature. But the huge drawback of optical glue is, of course, its stickiness to the mold. There are mainly two kinds of optical glue - one is MMA (SK-9) and the other is polyurethane (Norland optical glue). After many trials by Ahmed Alsayed, we found it is least sticking to polyethylene. Thus we make a crossed grating on polyethylene slab (HDPE or LDPE) and use a crossed grating as a mold to imprint onto a layer of optical glue a cover glass and crosslink the monomer UV. Polyethylene is a very soft polymer with low glass temperature ($60 - 80^\circ$). The HDPE slab from McMaster Carr is actually full of tiny scratches and thus it takes high temperature or longer time to anneal the scratched surface during the imprint. A possible route to solve this problem is to dissolve high molecular weight polyethylene in some volatile solvent such as chlorobenzene and spin coat the polymer layer onto glass substrate like PMMA mold making. Fig. 3.4 shows a replica imprint from a crossed grating mold. The template has patterns of pyramidal holes which look like waffle and thus we call this a waffle template.

Soft Imprint Scheme

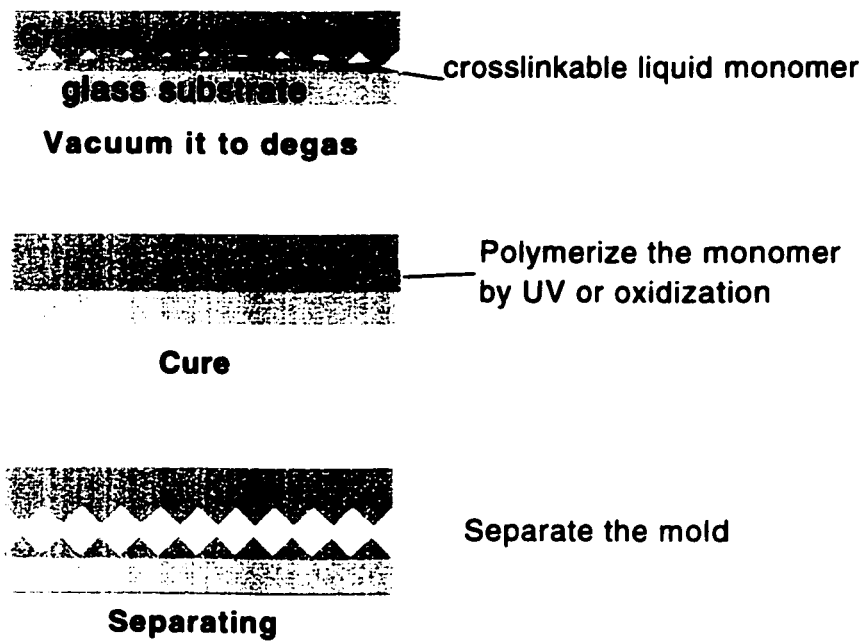


Figure 3.3: The schematics of soft imprint.

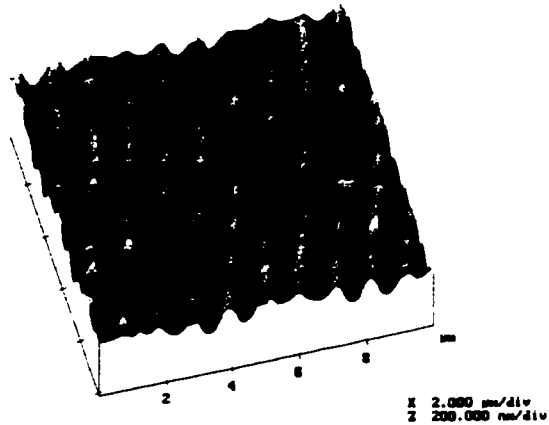


Figure 3.4: AFM scan of a waffle template.

3.4.2 The Wetting of Particles onto Substrates

Most of our analysis of the system has assume particle/substrate interactions are hard-core potential. However, it is actually important in colloidal assembly. Fig. 3.5 (a) and (b) show different colloidal crystal structures on different substrates at the same bulk concentrations of colloids/polymer mixtures. (a) is a clean glass surface where colloids wet the substrate and therefore the colloidal crystal spread out on the substrate. (b) is the optical glue where the colloids do not wet the substrate and the crystal tend to form in the bulk instead of wide spread on the substrate. (c),(d),(e) and (f) exhibit different surface densities of the colloids in the groove templates made with different optical glues (NOA61, SK9, NOA65 and NOA 72) under the same bulk conditions.

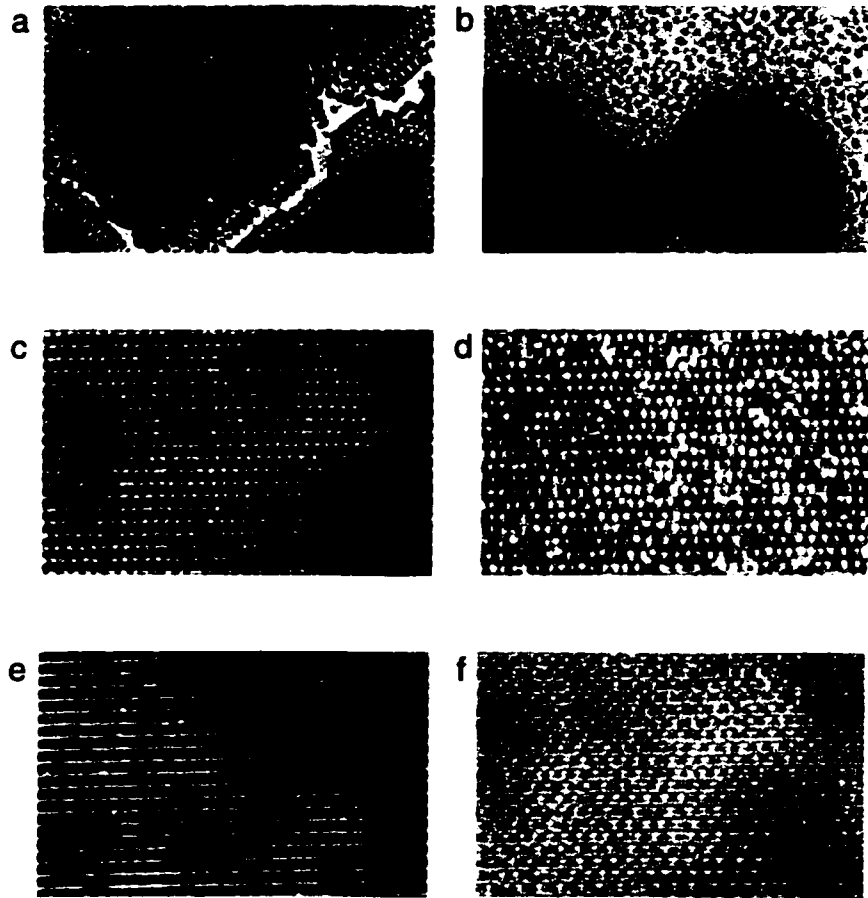


Figure 3.5: (a) a wide spread colloidal crystal formed on clean glass substrate where colloidal fluid wet the substrate well. (b) A droplet like colloidal crystal formed on a substrate made of optical glue (SK9). (c),(d),(e) and (f) show different surface density of of colloids in the groove made of different optical glue (NOA61, SK9, NOA65 and NOA 72) with the same bulk concentration.

3.5 Chambers

There are many ways to make sample chambers that can be viewed under the microscope. The most common one is the parafilm chambers. The learning of parafilm chamber making is one important syllabus of Yodh lab 101. The coverslips are attached to the microscope slide by Parafilm strips cut into a 'L' shape, and arranged so that they form a square with two channels left open for sample loading. The volume of the cavity is controlled by changing the width of the L's. A heating plate was used to melt the Parafilm sealing the coverslip to the microscope slide. After injecting the solution, the chamber is sealed with vacuum grease. When the chamber is made properly, the sample inside can last for months. Parafilm chambers are good for aqueous samples but dissolve in organic solvents.

For organic sample "thin chambers", I cut stripes of No. 2 coverglass as spacers (~ 0.2 mm) and glued them between coverglass and slides by optical glue. The chamber were then sealed with 5 minute epoxy. 5 minute epoxy may dissolve in some solvent, like tetrachloroethylene and cause gelation of the colloidal suspensions. It is necessary not to have any contact between uncured epoxy and organic solvents. The current chamber is made of a raschig ring (Fisher Scientific. part no.10-462-44, inner diameter 10 mm) glued on coverglass. The chamber is sealed by a plastic testtube cover and teflon septum insert.

3.6 Optical Microscopy

The advance of optical microscopy has pushed forward the investigation at the micron and submicron level in a wide variety of disciplines. Rapid development of new fluorescent labels has accelerated the expansion of fluorescence microscopy in laboratory application and research. Digital image processing with video has also enabled quantitative measurements in real time. In this section, we discuss concepts in optical microscopy that are the essential instrument in our research. The main ideas are crucial for the optical setup such as optical tweezers, and the confocal microscope.

In the simplest form of an optical microscope, it consists of two positive lenses, an objective lens of small focal length that image the object and a magnifier functioning as an eyepiece. In the most modern design of microscopes the manufacturers move to infinity-corrected optics, i.e., the objective forms the intermediate image at infinity. It requires another tube lens to form the real intermediate image before the eyepiece. The advantage of this design is that when extra optical components such as prisms and polarizers are introduced into the system, there will be little distortion because all the light from the specimen passing through the component is parallel.

The important concept in image formation was pointed by Ernest Abbe in 1870 – “a microscopic image are the consequence of interference of the direct light from the light source with the diffracted light from the specimen structure.” This idea is illustrated in Fig. 3.6. Suppose the light source is point-like at infinity and is

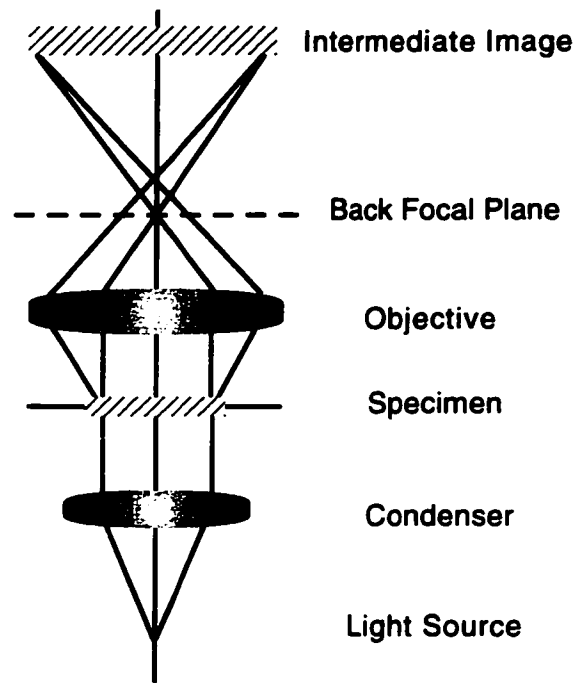


Figure 3.6: The image formation through a lens.

collimated by condenser a plane wave travels through the specimen. Some light is diffracted by the sample and some is not. In the back focal plane (BFP), the so-called primary image of light source is formed in the center of light path. The diffracted and undiffracted light keep travelling and interfere to form the intermediate image. The image formed in a microscope have interfered twice. Light in the BFP is the spatial Fourier transform of the front focal plane of the lens. Modulation of the light on this Fourier plane enable contrast enhancing of the images. It facilitates the invention of phase contrast microscopy which won F. Zernike the Nobel prize in 1953. Usually an object which differs slightly from the surrounding in index of refraction is hard to observe due to low absorption contrast. In phase contrast microscopy, a quarter wave

phase ring is placed in the back focal plane to increase the phase of undiffracted light by $\pi/2$. As a result, the interference between the zeroth order light and diffracted light is enhanced. A visible amplitude image has been produced. Moreover, changing the incident light angle in the BFP enables the manipulation of output light position in the image plane. This is useful in designing scanning optical instruments – such as scanning optical tweezers and the confocal microscope.

In optics two planes are called conjugate planes when points on one plane are focused onto the other plane through lens and vice versa. In the proper alignment of an optical microscope there are two most important sets of conjugate planes - image and aperture planes, as shown in Figure 3.7. The image planes include field diaphragm, specimen plane, intermediate image plane and retina. Eric Weeks. In this section, we review the method of calibration.

Because a lot of our measurements are directly from the images, it is essential to calibrate the pixel size carefully. For a precise calibration of x and y, I use optical grating as a calibration standard. It is shown in Fig. 3.8 Image 3.8 a is taken by confocal microscope without excitation filter. The effect of scratches and roughening is evened out by averaging over the intensity along y axis. The average intensity profile is shown in Fig. 3.8b and the positions of the peak are located. In Fig. 3.8c shows the fitting of positions of peaks to the index number of peaks and the slope gives the corresponding pixels to the grating pitch. Generally there are 40-60 peaks

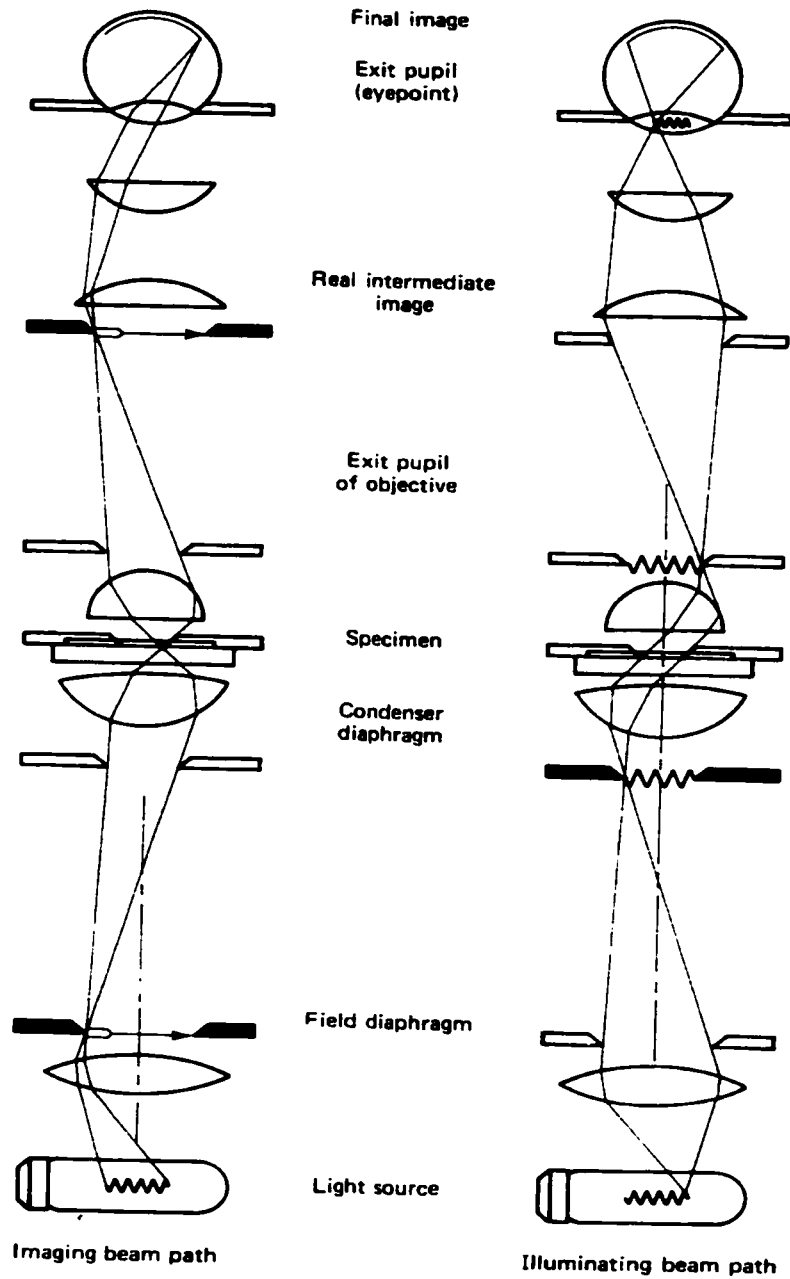


Figure 3.7: Two sets of conjugate planes: (a) image planes (b) aperture planes. The figure is reproduced from Introduction to Optics by F. L. Pedrotti and L. S. Pedrotti.

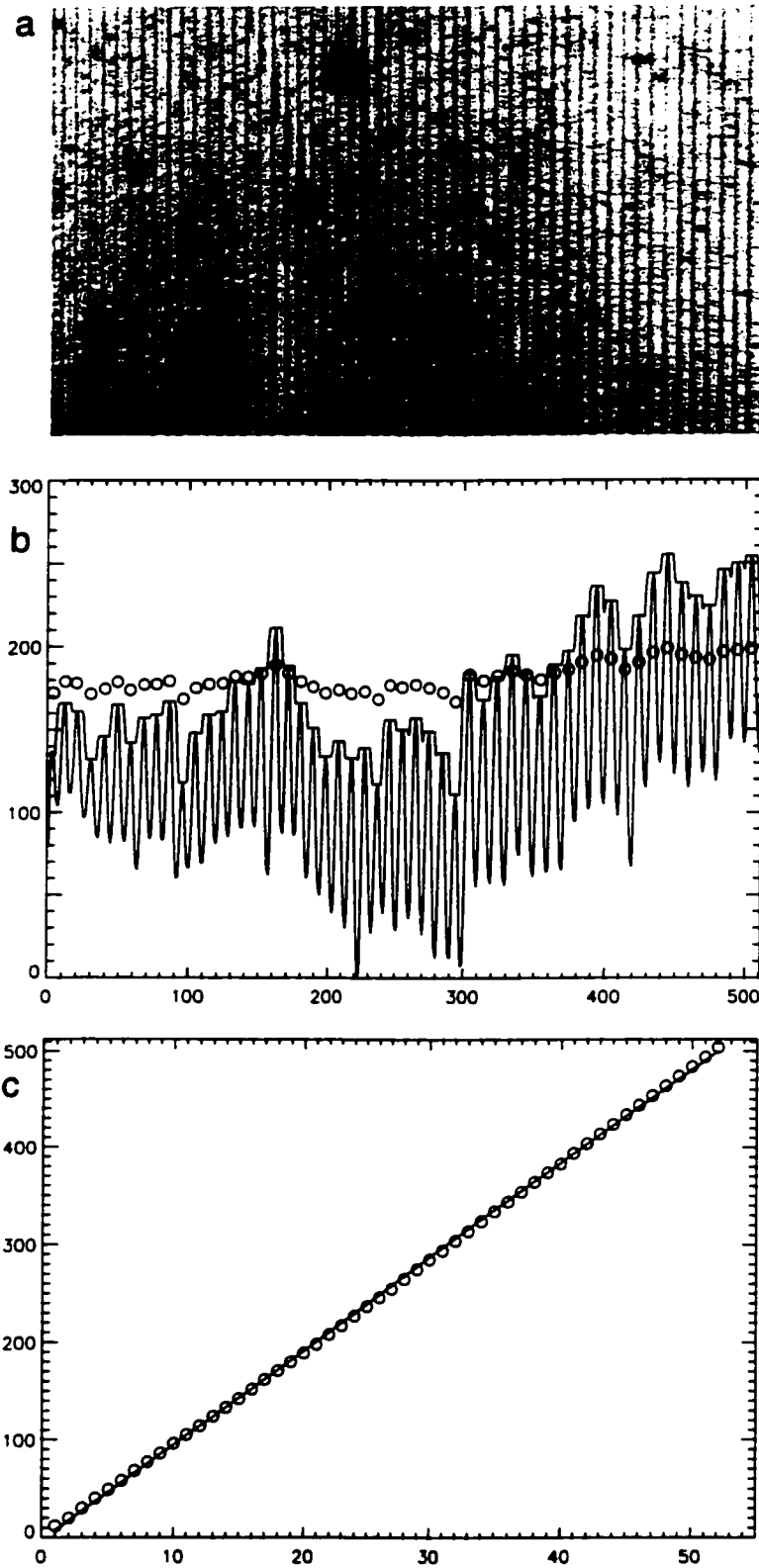


Figure 3.8: (a) a grating image. (b) The intensity profile of a grating image. (c) the positions of peaks in the intensity profile.

and therefore the precision of measurement can be improved by $\sim 50\times$. Repeat the same procedure in the y direction. It is often that there is 1 – 2% difference in x and y spacing. It is interesting to note that the image is not flat in the confocal calibration image as there is slight nonlinearity in the peak spacing shown in Fig. 3.8c.

For z scale, the piezo-stage should be well calibrated from the company. The index of refraction of solvent will change the z scale by 1.518 (immersion oil)/ n_{solvent} to the first order approximation. We performed z calibration. Our strategy is by measuring the spacing of colloidal crystals. We used the colloidal crystals of charged PMMA fluorescent particles dispersed in known index solvent and almost density matched. The charged colloids form nice hexagonal close packed crystals from glass substrate. We take crystal image cube of 10-20 layers deep with $0.15\ \mu\text{m}$ spacing in z . The interparticle separation d in xy plane can be measured precisely. The layer spacing along in z axis should be $\sqrt{2/3}d$. From our measurement, the z spacing value is within 5% error from the factory piezo calibration value. It may be desirable to sacrifice the spacing in z between different planes in order to have more layers taken.

3.7 Optical Tweezers and Interaction Measurements

In 1986 Ashkin showed that a highly focused laser light can be used to trap a dielectric particle by the optical gradient force [106]. This optical force trap is called laser tweezers and is widely used in colloidal science to manipulate particles. One important

application of tweezers has for measurement of interactions between colloidal particles [107, 108, 109]. The optical tweezers can confine particle in space and allow fast feedback control.

There are several kinds of interaction measurements. One conceptually simple approach employs the direct visualization by determining the equilibrium pair correlation function $g(r)$ of spheres in a dilute suspension and infers the pair interaction potential from Eq. 2.29 [110, 111, 112]. It is however difficult to determine out-of-focus particle positions and to have good statistics in dilute concentration. Digital video microscopy has been advanced to determine the centroids of the particles with sub-pixel resolution [113]. There are a few other detection techniques which achieves nanometer resolutions such as total internal reflection applied in interaction measurement [114, 115]. There are also more traditional routes to measure the interaction by force measurement instruments such as surface force apparatus and atomic force microscope [116, 117].

Besides using optical force, magnetic force is another common way to manipulate colloidal particles with high magnetic susceptibility. There has been magnetic tweezers built to measure the elasticity of a DNA molecules [118] or to use the knowledge on magnetic force interaction [119, 120].

3.7.1 Optical Line Scanned Tweezers

A detailed and extensive discussion on optical line scanned tweezers can be found in in Ritu Verma's thesis [121]. Here we will summarize the basic idea of the measurements and gives some supplementary discussion on line tweezers.

Our measurements were performed with a line-scanned optical tweezer (50 mW, $\lambda = 1053$ nm, NA=1.3)[122]. Fig. 3.9 shows the schematic of the setup. Briefly, the two silica spheres were trapped in a one-dimensional optical potential generated by scanning a tightly focused laser beam back and forth along a line at 180Hz. The line trap was focused more than $4 \mu\text{m}$ away from the sample chamber's coverglass to minimize possible wall effects. The two spheres in the trap shared a roughly harmonic potential along the scan direction and were strongly confined in the other two dimensions. For each potential measurement, the spheres' thermal motion was followed by bright-field video microscopy and recorded on a S-VHS deck for an hour: subsequent digitization yielded 2×10^5 images. Center-to-center separations were estimated by the in-plane distance between the sphere images' brightness-weighted centroids [113]. We employ an algorithm which largely corrects for overlap of the spheres' diffraction blurred images [122].

The interparticle potential $U(h)$ was calculated from the measured probability distribution of sphere contact separations, $P(h)$, using the Boltzmann relation $P(h) \sim \exp(-U(h)/k_B T)$. We made one measurement with rods and another without rods

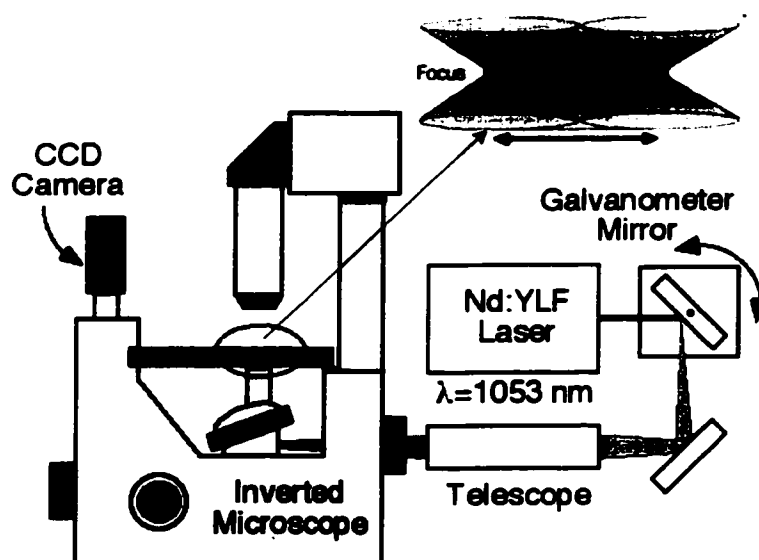


Figure 3.9: The schematic of an optical line scanned tweezer. A galvo mirror is placed in a conjugate plane of the back focal plane of the microscope. The oscillation of the galvo mirror control the translational scan of a laser tweezer in the image plane which produce a time-average 1D optical potential.

under the same optical and chemical conditions; this enabled us to isolate the potential due to the rods from other contributions. To quantitatively compare the observed data with a model potential, we first convert the model to a probability distribution, $P(h)$, numerically convolve it with a Gaussian kernel to simulate our instrumental resolution, and then convert it back to a potential by taking the logarithm. The $P(h)$ distributions for hard sphere-like control measurements were well fit by a step edge convolved by a Gaussian with a 30 nm half-width. We use that value for the blurring kernel in all model comparisons. The energy resolution of $0.05 k_B T$ is set by counting statistics.

The shape optical potential is controlled by the scanning of galvo and is in the

quadratic forms. The harmonic optical potential increases the probability of particles in the close contact of interaction range. Also a quadratic potential between two particles can be expressed in the new variables, the relative separation between particles and the sum of two positions. The depletion potential measurement is a differential measurement. There is potential between particles contributed by the optical tweezers.

$$U_{\text{buffer}}(x_1, x_2) = \frac{1}{2} k x_1^2 + \frac{1}{2} k x_2^2 \quad (3.3)$$

where $|x_1 - x_2| > 2a$. The total potential with the depletants such as fd solutions is

$$U_{\text{fd}}(x_1, x_2) = \frac{1}{2} k x_1^2 + \frac{1}{2} k x_2^2 + U_{\text{entropic}}(h) \quad (3.4)$$

where $h = |x_1 - x_2 - 2a| > 0$. The entropic interaction only depends on the relative separation of two particles and is the difference between Eq. 3.3 and Eq. 3.4. It is sufficient to extract relative particle distance $r = |x_1 - x_2| = h + 2a$ from the data because $U_{\text{buffer}}(x_1, x_2)$ can be rewritten as

$$U_{\text{buffer}} = \frac{1}{4} k R^2 + \frac{1}{4} k (h + 2a)^2 \quad (3.5)$$

where $R = x_1 + x_2$. Thus the measurement in “buffer” gives the second term in Eq. 3.5. We can remove that term contributed by the optical potential from 3.4 by fitting the buffer measurement with a parabolic with the minimum at $h = 2a$ and derive U_{fd} as shown in Fig. 3.10.

The potential is measured from the histogram of particle separation and there is

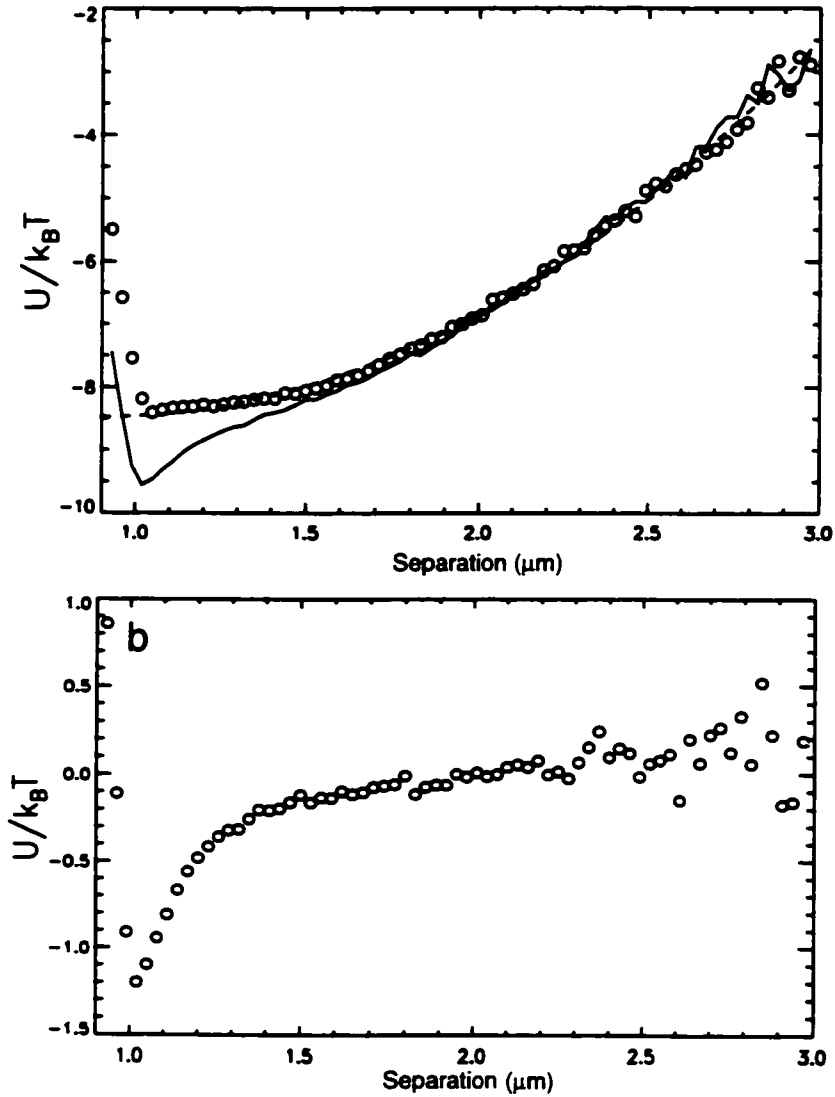


Figure 3.10: (a) the solid line represents the raw potential measured with fd virus and the open circle represents the raw potential measured in a pure buffer. The dashed line is the parabola fit to the raw buffer potential. (b) shows the fd depletion potential after subtracting the parabolic fit from the measured potential.

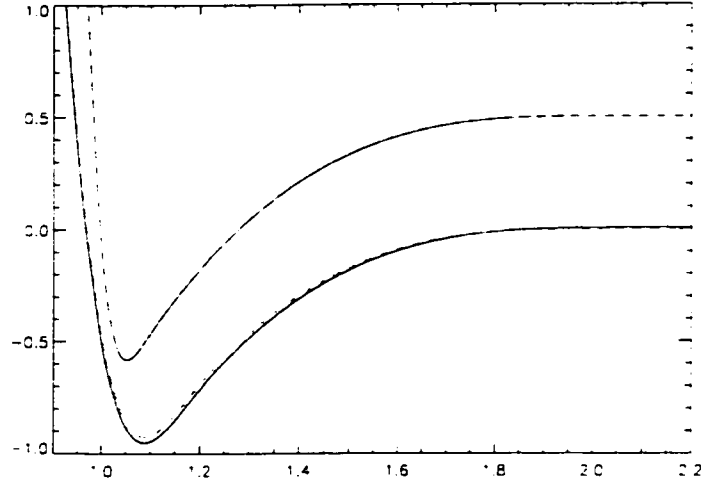


Figure 3.11: Comparing the blurred depletion potential with the subtractions of blurred optical potential from the blurred combined potential. The top lines are with $\sigma = 0.03$ and the bottom ones are with $\sigma = 0.06$. When σ is small, the two cases are almost indistinguishable.

a limit in spatial resolution. The hard sphere repulsion potential appears “softened”. This effect would make the decoupling of two independent potentials difficult if the spatial resolution is low. The distribution function of separation is,

$$P(h) = \int_{-\infty}^{\infty} dh' \exp - \left[\frac{U_{\text{optical}}(h') + U_{\text{entropic}}(h')}{k_B T} \right] \exp - \left[\frac{(h - h')^2}{2\sigma^2} \right]. \quad (3.6)$$

Only when $\sigma \rightarrow 0$, the blur function $(2\pi/\sigma^2)^{1/2} e^{-\frac{(h-h')^2}{2\sigma^2}} \rightarrow \delta(h - h')$, the logarithm of probability distribution function is truly a linear combination of two different potentials. When σ is small, it is still quite a good approximation but there will affect the potential a little as shown in Fig. 3.11. The effect causes bigger error in the potential near contact.

There is other effect due to the optical tweezers through scanning. When the

laser beam scans through the particle, it brings particle back to the focus point but also drags the particle along the scanning direction as if the laser tweezers “kick” the particle. A laser trap exerts force $k\Delta x$ on a particle where k is the optical spring constant depending on the strength of the trap and Δx is the deviation of the center of particle from the center of the trap. Typically for 50 mW laser, 1 micron beads, k is 0.1 pN/nm and thus the tweezers exerts at maximum 50 pN on the particle. The viscous force from water is actually big. $F = 6\pi\eta 2av$. At the scanning rate – 20 micron amplitude at 180 Hz, it requires about 160 pN for particle to follow the trap. Therefore, the force not strong enough to move particles significantly. The sampling frame rate is at 60 Hz. In a single frame, laser has scanned back and forth three times. The kicking effect is effectively “average” out. The kicking fluctuation is uncorrelated from the “potential fluctuation”. In our measurement, we have about 30 nm resolution, a “dead-zone” which could be either from centroid measurement error or kicking.

3.8 fd Bacteriophage

The rod shaped virus particles fd, m13 and pfl are unique experimental systems. They are identical in structure which gives rise to the same length, diameter and charge density. Currently no synthetic colloidal rod system can achieve this high degree of monodispersity. The bacteriophage fd is long and thin with contour length

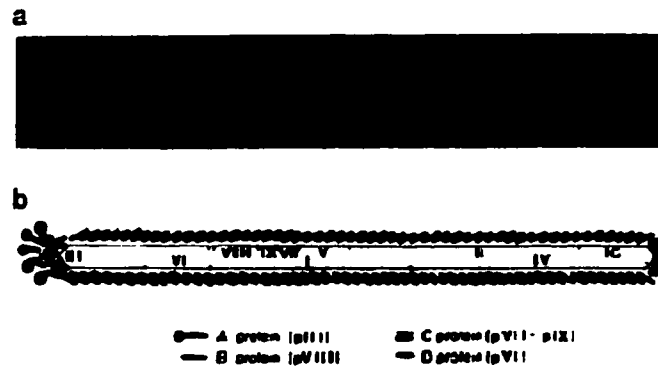


Figure 3.12: The fd bacteriophage particle. a. The top is an electron micrograph of fd virus. b. The bottom is a schematic representation of the phage particle showing the location of the capsid proteins. The figure is adapted from [3].

$L \cong 880$ nm and diameter $D \cong 6.6$ nm and it is flexible with a persistence length (previous reported in [123]) of $\ell_p \cong 2200$ nm. The electron micrograph shows a bent fd in figure 3.12A. fd is composed of five proteins shown in Figure 3.12B. The major coat protein (1IFD) has helical structure. It compose a hollow cylinder filled with the single stranded DNA. The carboxylated group end of the major coat protein is exposed and gives rise to a high charge density. One end of the minor coat protein (1G3P) contains four positive lysine residues. It comprises the knob to infect *E. coli*. The other end of the minor coat protein is hydrophobic. The molecular weight of fd is 1.64×10^7 dalton and the optical density is 3.84 (for concentration 1 mg/ml at 1 cm optical path, wavelength = 269 nm).

3.8.1 fd Production and Purification

Recipes of fd growth are described in a number of papers [124]. We follow the protocol from Malik *et al.* [3] to grow and purify fd. fd are bacteriophages that infect *Escherichia coli*. A detailed protocol of making 4 liter bacteria growth is as follows:

When working with *E. coli*, one should take steps to prevent contamination on bacteria such as clean the bench surface with ethanol, and burning the neck of flask when it's open. This prevents unwanted bacteria growth in *E. coli* broth. *E. coli* are stored at -70 degree. When it is taken out of freezer, it should be kept in a dry ice bucket.

Day 1. A tiny amount of frozen *E. coli* is extracted onto the agar dish by a pipette tip and spread by a platinum loop. Two dishes are made and left in the 37 degree incubator overnight. We prepare 5 liter YT broth (yeast extract and tryptone from Life Science) in 1L flasks for the next day and autoclave them.

Day 2. We infect 5 batches of 3 ml YT medium with one plaque of fd and place them in the shaker for 6 hours at 37°, 300 RPM. At this stage, we mixed the E-coli with some glycerin (15%) to make the stock and froze it quickly. (The glycerin is autoclave with the small glass vial before time.) We pour these 3 ml *E. coli* broth into 50 ml broth in a 250 ml flask (Make 5) and leave them in the shaker at 37 degree at 300 RPM overnight.

Day 3. 5 flasks of 1 L YT medium were infected with this 50 ml overnight growth

batch and placed in the shaker for another hour. The optical density (OD) of medium should be between 0.35-0.45 at 660 nm. The E. coli. broth is readily infected by 1 ml fd per batch and is allowed to grow overnight.

Day 4. The broth is now filled with fd and E. coli. The solution is centrifuged at 6000 RPM for 20 minutes in the rotor GS-3 where the centrifuge bottle is filled to three quarters. This step allows to separate the E. coli body and fd. We collect the supernant which is full of fd in one or two big flask. Each liter of supernant is added with 40 g of PEG (mw. 8000) and 30 g of NaCl and left overnight at 4°().

Day 5. We run all of fd/PEG/NaCl broth through the centrifuge in 150 (200ml) bottle in rotor NO. SLA 1500, 13K RPM for 20 min and remove supernant quickly to avoid redisperse fd. We collect pellets of fd virus . At this step, fd are strongly aggregated in the bottom of bottle. We squirt them off from the bottle wall in a gentle fashion by a plastic pipette with TE buffer ⁶. We add 25% volume of 20% PEG (mw. 8000) with 2.5 M NaCl to the supernant. The virus will be precipitated almost immediately but store the suspension in the refrigerator for at least one hour or overnight.

Day 6. The virus solution is spinned for 1 hour at 10,000 RPM (19900 g) in Ti42.1 rotor. We trash supernant immediately by inverting the tube in the upside down for one minute and redisperse fd again in 10 ml pH 8 TE buffer per tube. (5 tubes) wait

⁶TE buffer (pH 8.0): 10 ml of 1M Tris (pH 8.0) 2 ml of 0.5 M EDTA dilute to a final volume of 1 L with Millipore water.

over night.

Day 7. (Gradient) We dilute the original solution to the final concentration between 0.5 - 1 mg/ml. The O.D. for fd at 269 nm is 3.86. CsCl is added at 0.5 g / ml amount. (Wear gloves to handle CsCl which is neural toxic.) We centrifuge the whole fd/CsCl suspension at 40,000 RPM in swinging rotor SW50.1 for 30 hrs.

Day 8. After the gradient centrifuge, the virus will appear as a blue translucent band at a level about 1/3 from the top of the tube. We collecting all the bands into a dialysis tubing (12,000-14,000 Mw) and dialyze against 0.5 M NaCl (116.88 g per 4L) and the desired buffer (e.g. 5mM sodium borate) for at least twelve hours for three changes.

Final: Concentrate fd by spinning at 50,000 rpm in the SW50 rotor for two hours.

To determine the final yield of the phage, we dilute the phage at least 20 times and scan sample by light with wavelength from 200 to 400 nm. The spectrum should peak at 269 nm and the A_{260}/A_{280} ratio should be approximately 1.1.

Fd can last for a long time if not drying out. It should be stored in the buffer at 4 °. The buffer can be TE or Sodium Borate at pH 8. When the sample is left too long and impurity grows inside, you may centrifuge at lower speed to sediment the impurity or perform a gradient again with enough fd quantity (> 0.5 ml). fd can be broken by strong shearing. therefore, It should be pipetted in a gentle fashion and never vortexed, instead stirred to mix by pipette instead.

3.9 Physical Dimensions of filamentous bacteriophage

The literature contour length of fd are consistently ranging from 850 – 920 nm by various methods [125]. There are quite a few experiments to determine the persistence length and contour length. We summarize the different approaches in the following section.

3.9.1 Electron Microscopy

The high resolution electron microscopy (EM) allows one people to look at biopolymers such as DNA and filamentous bacteriophage. The images reveal the physical properties of biopolymer such as dimensions and the flexibility by measuring the contour length L and the end-to-end distance R . For a 2D system, the relationship between R , L and the persistence length ℓ_p is,

$$\langle R^2 \rangle = \frac{2L}{\lambda} - \frac{2}{\lambda^2}(1 - e^{-\lambda L}) \quad (3.7)$$

where $\lambda = 1/\ell_p$. Persistence length is a mathematical definition by the correlation of tangent vector along the polymer while λ , the bending energy has more physical meaning. Maeda and Fujime (MF) [126] analyzed about 900 fd's EM images and determined $L = 885 \pm 30\text{nm}$ and $\ell_p = 1.95 \pm 0.2 \mu\text{m}$. Beck and Duenki [127] examined M13, a close relative of fd, under EM by two different sample preparation methods – spraying and sandwiching which yielded two distinct results. They determined the contour length $918 \pm 25 \text{ nm}$. One is to spray the droplet with virus onto the grids

and the contour length has binomial distribution and the mean end-to-end distance is 766 nm and the most probable end-to-end distance is 850 nm. The other method is by sandwiching the sample droplet between two mica-chips. The samples often exhibited short rod-like particles, rather different in length. The mean end-to-end distance was $R = 862\text{nm}$ and the most probable R was 900nm. They determined $\ell_p = 0.49 \mu\text{m}$ (spray) and $\ell_p = 3.33 \mu\text{m}$ (sandwich) respectively and concluded that sandwiching method was more reliable since the result agreed with the light scattering result better. However, in 2D, λ should be $1/\ell_p$ so the value of persistence length should be doubled from their original value, $\ell_p = 0.98 \mu\text{m}$ (spray) and $\ell_p = 6.66 \mu\text{m}$ (sandwich) . It is questionable that sandwiching is a better method since during the drying process fd experienced very strong shear force which gives rise to the wide range of contour length distribution and straighter looking. Jay Tang (private communication) examined 68 M13 and measured $R = 690\text{nm}$ and $L = 800\text{nm}$, suggesting $\ell_p = 0.47 \mu\text{m}$. In summary, the huge range of end-to-end separation from different experiments indicates that EM is not a reliable method to measure the persistence length. Moreover, this method is less reliable when the persistence length is long as shown in Fig.3.13. For example, when $R = 800 \pm 10 \text{ nm}$, $\ell_p = 1.25 \pm 0.2 \mu\text{m}$ while the contour length is $L = 880 \pm 20 \text{ nm}$ which will gives rise to $R = 825 \pm 10 \text{ nm}$ assuming $\ell_p = 2.2 \mu\text{m}$.

To determine persistence length more reliably by EM, it may be best to fit the

distribution function of end-to-end distance [128]:

$$G(r) = \frac{\kappa}{\pi^{3/2}\mathcal{N}} \sum_{j=1}^{\infty} \frac{(2j-1)!!}{2^j j! [2\kappa(1-r)]^{5/4}} \exp\left[-\frac{(j+1/4)^2}{2\kappa(1-r)}\right] D_{3/2}\left[\frac{2(j+1/4)}{\sqrt{2\kappa(1-r)}}\right], \quad (3.8)$$

where $D_{3/2}(x)$ is a parabolic cylinder function, κ is L/ℓ_p and \mathcal{N} is a normalization factor. $G(r)$ is calculated based on the distribution of end-to-end distance in 2D equilibrium. If the sample agrees with the distribution function, it is less likely to have artifact from the sample preparation. Moreover, the comparison to the distribution function gives better accuracy especially because the distribution function is highly asymmetric and sharply peaked. The other possibility is to AFM scanning on adsorbed fd on substrate which can eliminate the problem of meniscus force during drying out.

3.9.2 Dynamic Light Scattering

The other method to measure the persistence length of semiflexible polymers without obvious artifact from sample preparation is to determine the dynamic structure factor by light scattering. However, this method depends on the theoretical models to interpret data. In 1977 Newman *et al.*[129] analyzed the intensity autocorrelation function by the rigid rod model. They concluded the dimensions of fd virus to $L = 890 \pm 20$ nm and $D = 9 \pm 1$ nm assuming $\ell_p = \infty$. In 1979, Loh *et al.* fit the data with two exponential decays – “slow” and “fast” and attributed the fast decay

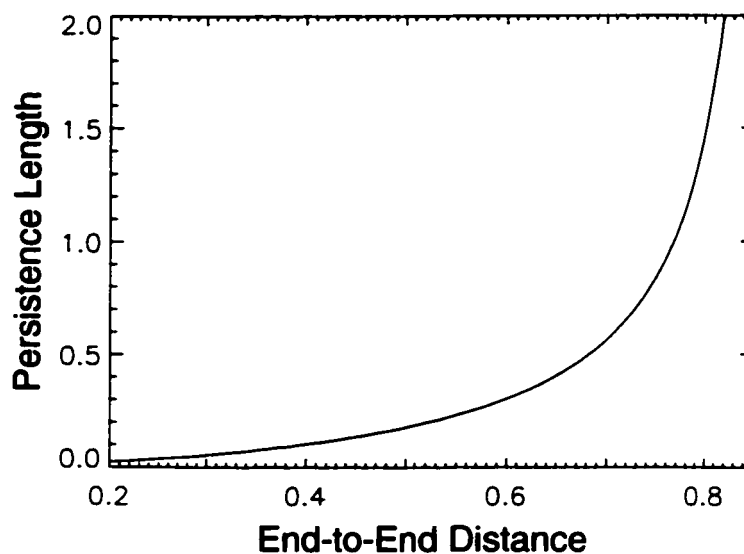


Figure 3.13: Persistence length vs. End-to-End distance for a semiflexible polymer with contour length $0.88 \mu\text{m}$. When the end-to-end distance becomes close to the contour length, the persistence length increases exponentially.

to the bending mode of virus and interpreted the slow decay as rigid rods. They showed $L = 900 \text{ nm}$. In 1985 Maeda and Fujime (MF) not only performed EM on fd virus but also light scattering measurement. They built a weakly bending rod model by calculating perturbation of the rigid rod model. They determined the flexibility parameter $\lambda L = 0.23$ with lower bound 0.13, upper bound 0.25 and the contour length $L = 895 \pm 40 \text{ nm}$. In 1991 Song *et. al.*[130] conducted similar experiments on m13. They concluded the persistence length of m13 virus between $1.5 - 2.0 \mu\text{m}$ with a different theoretical model. In Song's paper, they pointed out few flaws in MF model. MF considered the hydrodynamic of rods by employing isotropic, spherically average Oseen tensor which may be inconsistent They also assumed that the trans-

lational and rotational modes are not influenced by the bending modes. In Song's work, they employed the discrete bead model developed by Goldstein where all bead motions associated with bending are constrained to occur in a plane perpendicular to the end-to-end vector, thus prohibiting extension or contraction along the axis, i.e. the end-to-end distance is constant while the contour length can vary. Both MF and Goldstein's theories have the common assumptions and limitations. They both restrict the subunit displacements due to the bending to be perpendicular to the end-to-end vector (rod-axis) and for a short time that end-to-end vector (rod-axis) rotates only slightly ($\sqrt{2D_R t} \ll 1.0$). They are only quantitatively valid for $L/\ell_p < 0.6$ [130].

It is difficult to develop a complete theory for the dynamical properties of a semiflexible rods [131]. The flexibility increases the diffusion coefficient $D \propto R_g^{-1}$ and decreases the intrinsic viscosity $[\eta] \propto R_g^3$ as the flexibility increases. It also gives a relaxation in the high-frequency region. There are few recent theoretical models of the dynamic structure function of semiflexible polymers which account for the inextensibility of the polymer chain and hydrodynamic interactions [132, 133]. Based on both models the structure factor due to structure relaxation obeys a stretched exponential decay instead of single exponential decays of MF and Goldstein's theories. The most recent dynamic light scattering experiments performed by Augustin[134] confirmed this and his results were compared with [132] theory and showed that the persistence length of fd is smaller than the literature value without however giving the value.

3.9.3 Isotropic and Cholesteric Transition

It is well known that rod-like molecules self-assemble into nematic and smectic phases. For semi-flexible polymers they can still exhibit this variety of phases but the phase transition point depends on flexibility. Khokhlov and Semenov (KS) first generalized Onsager's theory to the systems of $L \gg D$ for arbitrary ℓ_p [135]. They solved explicitly only in the limit $L \gg P$. In 1995 Chen reported an accurate numerical calculation of the KS model for hard particles of arbitrary flexibility. Meanwhile, Tang and Fraden measured the coexistence concentration of the isotropic and cholesteric liquid crystalline phases of semi-flexible rod-like virus fd in aqueous suspension and compared with Chen's numerical solution [136] to KS theory. They measured the ratio of isotropic to cholesteric coexistence concentration $(\rho_{i,a}, \omega = (\rho_a - \rho_i)/\rho_i)$. The average ω from the experiments is 0.099 which corresponds to $\lambda = 0.2$ in Chen's theoretical model. However, in [136] Chen referred to the definition of $\lambda = L/\ell_p$ instead of $\lambda = L/2\ell_p$. Through private communication, the correct definition should be $\lambda = L/2\ell_p$ and all the theory should be rescaled by factor of two. Therefore $\lambda = 0.4$ which gives $\ell_p = 1.1 \mu\text{m}$ instead of $2.2 \mu\text{m}$.

3.9.4 Summary on the Physical Dimensions of fd

There are also independent measurements on mass per length (18400 ± 1400 dalton nm^{-1}) and the molecular weight of fd is $16.4 \pm 0.6 \times 10^6$ dalton. From here we can

deduce the total length: 890 ± 40 nm.

L (nm)	ℓ_p (μm)	R (nm)	References	Comments
890 ± 20	∞	890	[129], [137]	
885 ± 30	2.2 ± 0.2	825	[126]	EM and DLS
895 ± 20	2.2 ± 0.2	840	[130]	DLS (M13 virus)
916 ± 30	0.98	760	[127]	EM (M13 virus) Spraying method
900	6.66	862	[127]	EM (M13 virus) Sandwich method

Table 3.4: Summary of fd Persistence Length Measurement

Chapter 4

Colloidal Interaction in Rod-like Molecule solutions

In Chapter 2, we provided a theoretical background associated with the rod depletion interaction. In Chapter 3 we described the experimental setup and the sample preparation. In this Chapter, we describe the first interaction potential energy measurements between spheres in a suspension of monodisperse rod-like molecules, specifically fd bacteriophage virus. We measure the potential of mean force between two spheres as a function of rod concentration and the ratio, a/L , of sphere radius to rod length. We compare our data to various theories [11, 19, 21, 138] and tested few modified models. We find significant deviations from YJM models that we attribute rod flexibility. We compare the data to the bent rod model which approximates the semi-flexible rod into a bent rod at fixed angle.

The attractive depletion potential was unchanged over a relatively broad range of salt concentrations. At high salt, however, we found qualitatively different repulsive and harmonic potentials. These latter observations suggest that the ends of the fd

virus can adhere to the particles, and can bridge between particles. Measurements on the bridged case provide mechanical information about single macromolecular rods.

4.1 AO sphere, Derjaguin, and YJM models

From chapter 2, we derived the rod-induced depletion potential between spheres when $a \gg L$. Eq. 2.10 can be written in terms of rod volume fraction ϕ , i.e.,

$$U_{\text{rod}}(h) = -\frac{2}{3} k_B T \phi \frac{La}{D^2} (1 - h/L)^3. \quad (4.1)$$

Here we have taken the diameter of the rod to be D [20]; hereafter we will refer to this result as the Derjaguin model. This result contrasts with the well known Asakura and Oosawa (AO) depletion potential due to a dilute gas of smaller spheres Eq. 2.11 which we can also express in terms of sphere volume fraction ϕ , i.e.,

$$U_{\text{sphere}}(h) = -3k_B T \phi_s \frac{a}{\sigma} (1 - h/\sigma)^2 \quad (4.2)$$

where σ is the small sphere diameter. In our case, the rods produce a depletion interaction more than $1000\times$ stronger than the same volume fraction of spherical depletants [139].

In our experiments, we are also going to compare our results to the YJM model (Eq. 2.16)

$$U_{YJM}(h; a/L) = -k_B T n_r a L^2 K(h/L; a/L).$$

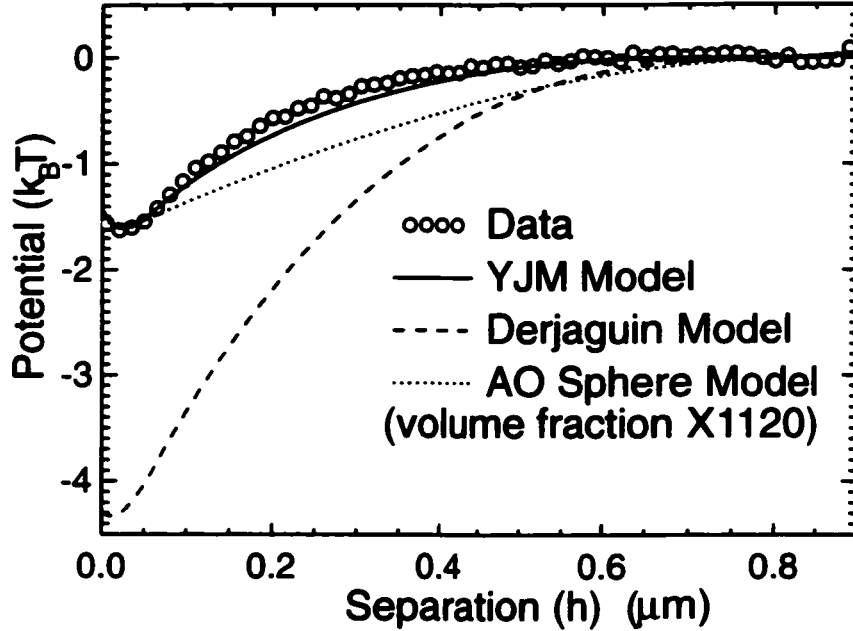


Figure 4.1: Comparison of typical data with three different models - Derjaguin rod, AO sphere and YJM models.

The program provided by YJM computes $K(h/L; a/L)$ numerically. We fit the numerical data with a polynomial and multiplied the polynomial by the rod number density n from optical density measurement, the squared length L^2 and the particle radius a to compare it to experimental data.

Fig. 4.1 shows a typical data set compared with Derjaguin (2.10), AO sphere (2.11) and YJM (2.16) models. The circles are the experimental data for $1.0 \mu\text{m}$ diameter silica particles in a dilute (0.7 mg/ml) solution of fd virus. The theory curves are computed with no free parameters and then numerically blurred to account for our instrument's spatial resolution. The Derjaguin model has an attraction at contact that is much too large. On the other hand, the YJM model has approximately the

correct magnitude and shape. We will show below that the experimental deviations from the YJM model are likely due to the entropy associated with rod flexibility. We also plot the AO sphere model rescaled to have the correct depth, with $L = \sigma$. The volume fraction of spheres is more than $1000\times$ higher than the real rod volume fraction. The experimental potential curve is distinctly more curved than any of these models.

4.2 Results and Modified YJM models

Fig. 4.2 displays the resulting potentials for all measured fd concentrations and two different sizes of colloidal spheres. As expected, we see that for the same rod concentration, the depletion attraction is stronger between the larger pair of spheres. Also shown in the figure (dotted curves) is the resolution-blurred YJM model with exact input parameters ($L = 880$ nm and number density). The measured potential however, is more strongly curved and systematically weaker than the theoretical model. We believe this discrepancy is due to rod flexibility. Even though the persistence length $\ell_p = 2.2$ μm of the rods is much longer than their contour length of 880 nm, bending and undulations of the virus make them appear shorter on average. The mean-squared end-to-end distance, $\langle R^2 \rangle$, is given by the Kratky-Porod (KP) expression [131],

$$\langle R^2 \rangle = 2L\ell_p + 2\ell_p^2 (e^{-L/\ell_p} - 1). \quad (4.3)$$

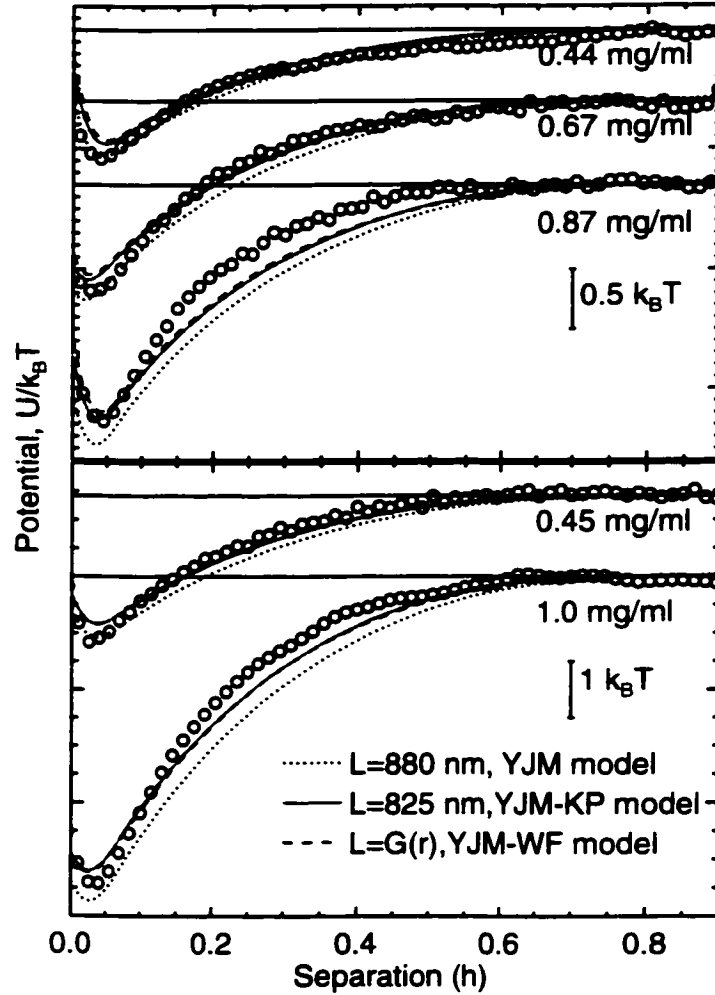


Figure 4.2: Interaction potential between pairs of (a) $1.0 \mu\text{m}$ and (b) $1.6 \mu\text{m}$ silica spheres in a suspension of fd virus at varying concentration. The dotted (solid) line is generated by the YJM model with $L = 880 \text{ nm}$ ($L = 825 \text{ nm}$). The dashed line is generated by YJM model with length distribution. This is essentially indistinguishable from $L = 825 \text{ nm}$ model.

For fd. the root-mean-squared end-to-end length is $R = 0.825 \mu\text{m}$. We substitute R for L in the YJM model yielding the solid curves in Fig. 4.2. The rod-bending modified YJM curves (YJM-KP) provide better agreement at large separations, but they are generally deeper than the experimental curve. At the closer separation, the experimental data are deeper than the model predictions.

The agreement of the KP-modified Yaman model and our data at further separation lead us to consider the actual end-to-end distance distribution, $4\pi r^2 G(r)$, of the rods because a polydisperse rod suspension can have a more strongly curved depletion potential. Wilhelm and Frey [128] have determined an accurate analytic form for the end-to-end distance probability density of semi-flexible rods:

$$G(r) = \frac{\kappa}{8\pi^{3/2}\mathcal{N}} \sum_{j=1}^{\infty} \frac{1}{[\kappa(1-r)]^{3/2}} \exp\left[-\frac{(j-1/2)^2}{\kappa(1-r)}\right] H_2\left[\frac{j-1/2}{\sqrt{\kappa(1-r)}}\right] \quad (4.4)$$

where $H_2(x) = 4x^2 - 2$ is the second Hermite polynomial, \mathcal{N} is a normalization factor, $\kappa = l_p/L$, r is the end-to-end distance normalized by the contour length L . The distribution function is shown in Fig. 4.3.

We computed a new depletion potential by numerically superposing YJM models (Eq.2.16) with different $L = R$, weighted by $4\pi r^2 G(r)$, i.e.,

$$U_{\text{YJM-WF}} = \frac{\int_0^L dR 4\pi R^2 U_{\text{YJM}}(h/R; R/a) G(R/L)}{\int_0^L dr 4\pi R^2 G(R/L)}. \quad (4.5)$$

We did this numerically by choosing 100 points of R . we calculated U_{YJM} by interpolating pre-calculated potentials with $R/a = 0.1, 0.2, \dots, 1.0$ and scaled to R corre-

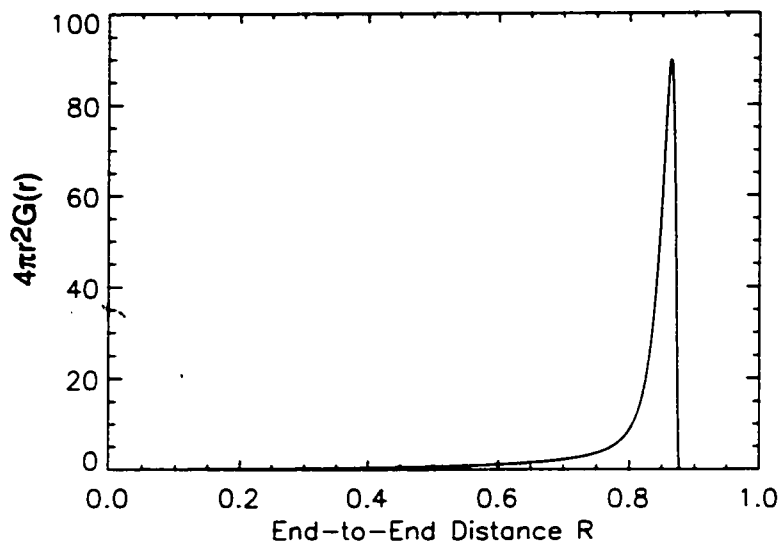


Figure 4.3: Probability distribution of fd end-to-end distance.

spondingly. The results (dashed line, YJM-WF) were barely distinguishable from the YJM-KP model, suggesting that the distribution of effective lengths does not explain the entropic discrepancy at short separation. Similar calculations demonstrated the data could not be explained by a fraction of the virus having broken during storage and handling.

We also compared YJM models with shorter length $L = 740, 760,$ and 780 nm with experimental data (Fig.4.4). They all showed better agreement at further separation. The deviation between data and model generally occurs around separations $h \sim 0.2\mu\text{m}$. The repeatable discrepancy at small h reveals entropic contributions from another degree of freedom in the system illustrated in Fig. 4.5. Flexible rods undulate in thermal equilibrium, and entropy is associated with these degrees of freedom. For

example, the bent rods have more rotational degrees of freedom than straight rods: bent rods explore physically distinguishable configurations when they rotate about the axis connecting their ends. These effects become significant only when the sphere surface separation is less than the typical transverse extent, W , of the rods. The relative increase of suspension entropy for closely separated spheres is thus greater for flexible rods than for rigid rods with equivalent end-to-end length. To estimate W , we consider a rod bent into a circular arc with end-to-end separation $0.74 \mu\text{m}$ and $0.78 \mu\text{m}$ and contour length $0.88 \mu\text{m}$. W will be $0.22 \mu\text{m}$ and $0.18 \mu\text{m}$ respectively. These are roughly the separation length-scale at which our experimental data deviate from the YJM-KP model. We can rule out dispersion force effects [140] as a possible mechanism: they are smaller, they would produce a deviation with the opposite sign, and they do not predict a natural crossover around $0.2 \mu\text{m}$. Furthermore, the agreement at large h demonstrated that the bent rod can be approximated as a straight rod with shorter length at large length scale. The entropic force in this case originates from the rotation about the rod center; therefore the interaction range should be the same as end-to-end distance R . Our data suggests a smaller end-to-end distance than the calculated value based on the literature values l and ℓ_p .

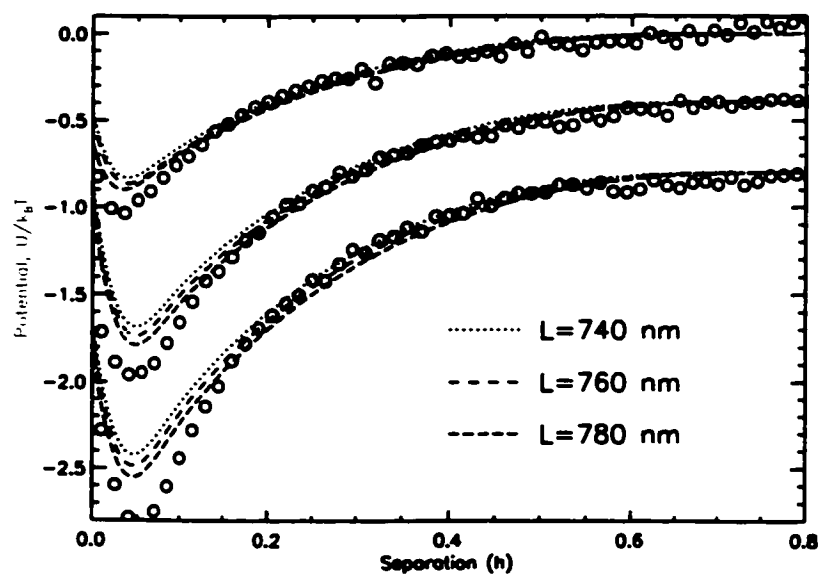


Figure 4.4: Compare Data with YJM model with different length $L=740$, 760 and 780 nm.

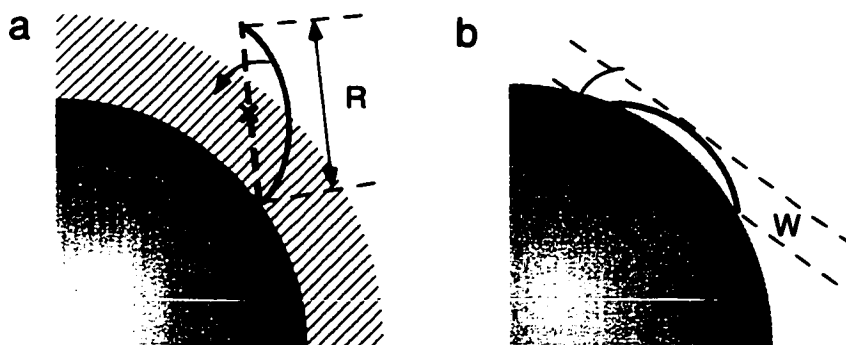


Figure 4.5: (a) The depletion zone for a bent rod rotating around the center of mass. (b) The depletion zone for a bent rod rotating around the end-to-end axis.

4.2.1 Bent Rod Theory

In Section 2.5 we discussed the recent theoretical model [29] which included the short range potential arising from the extra rotational degree of freedom. The model consider the lowest bending mode of a semiflexible rod and approximate it as a bent rod at fixed angle. The bent rod theory showed that two independent rotational movements of rods contributed two distinct energy terms, thus confirming our conjecture. In the bent rod theory the short range interaction between spheres were calculated within the Derjaguin approximation and for the long range interaction we used the exact solution from the YJM model. The combined YJM-L model is

$$U(h) = -k_B T n a R^2 \left[K \left(\frac{h}{R}; \frac{a}{R} \right) + \frac{\pi}{R^2} \int_h^\infty dx \Gamma(x, \alpha) \right]. \quad (4.6)$$

$\Gamma(h, \alpha)$ is the short range depletion interaction from rotation about the end-to-end axis of bent rods between two plates; the first term is the YJM model for a straight rod solution with $R = L \cos \alpha$. Fig. 4.6 compares a typical data set with three different models – YJM, YJM-KP, and YJM-L with $R = 740$ nm. The YJM-L model clearly gives best fit.

To determine the end-to-end separation of fd more precisely, we performed a χ^2 calculation of the YJM-L models for R between 720–825 nm and L between 880–920 nm for all data sets. We compared the average of χ^2 of the different concentration data for different R and L (See Table 4.1 and 4.2). When we constrained the concentration to the measured value, the YJM-L model of $L = 920$ nm and $R = 780$ nm gave the

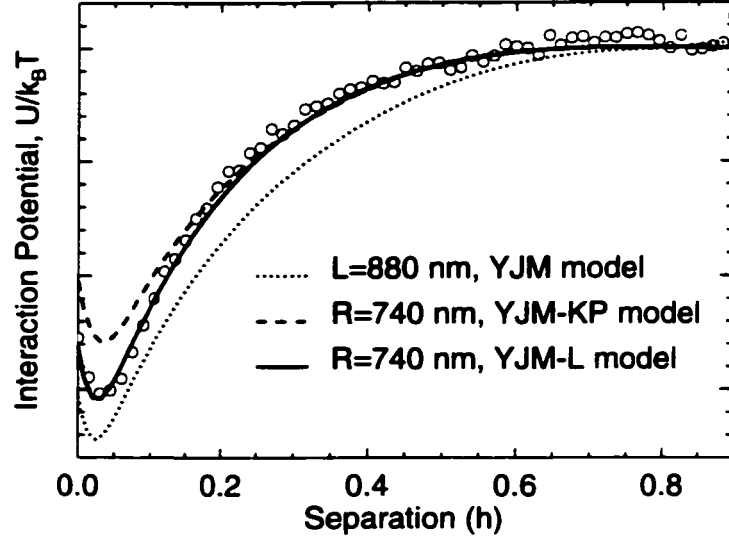


Figure 4.6: Comparison of a typical data set with three different models.

smallest average χ^2 value (Fig. 4.7). If we allow $< 5\%$ error in the concentration 1 and χ^2 is from the best fit, χ^2 is the smallest for YJM-L model of $L = 900$ nm and $R = 740$ nm (Fig. 4.8). From Eq. 4.3 we obtain an fd persistence length $\ell_p = 680 \pm 60$ nm, contour length $l = 920$ nm; from the fixed concentration analysis and $\ell_p = 850 \pm 100$ nm, contour length $l = 900$ nm. The literature values of fd [123] has contour length $l = 880$ nm and persistence length $\ell_p = 2200$ nm. The persistence length based on our measurement is surprisingly 2 or 3 times smaller than the literature value.

The YJM-L model explains our data very well. We should however make some notes about the approximation. Only the lowest mode of a semiflexible rod which is

¹The best fit concentrations are consistently higher than measured quantity.

	720	740	760	780	800	825
880	2.75	2.27	2.63	2.75	3.99	10.05
900	2.48	2.18	2.41	2.78	3.40	6.30
920	3.66	2.42	2.32	3.27	4.05	7.44

Table 4.1: Average χ^2 for different R and L with concentration as a adjustable parameter.

	720	740	760	780	800	825
880	10.20	8.35	7.30	6.40	6.50	7.99
900	7.01	5.95	5.04	4.38	4.09	7.95
920	4.12	4.12	3.44	3.26	3.58	9.57

Table 4.2: Average χ^2 for different R and L with fixed concentration as measured.

the arc shape is considered (Fig. 4.9a). The approximation of a bent rod with fixed angle exaggerates the transverse width W (Fig. 4.9b). The depletion interaction due to semiflexible rods should exhibit more curved potential at smaller h than the fixed bent rods.

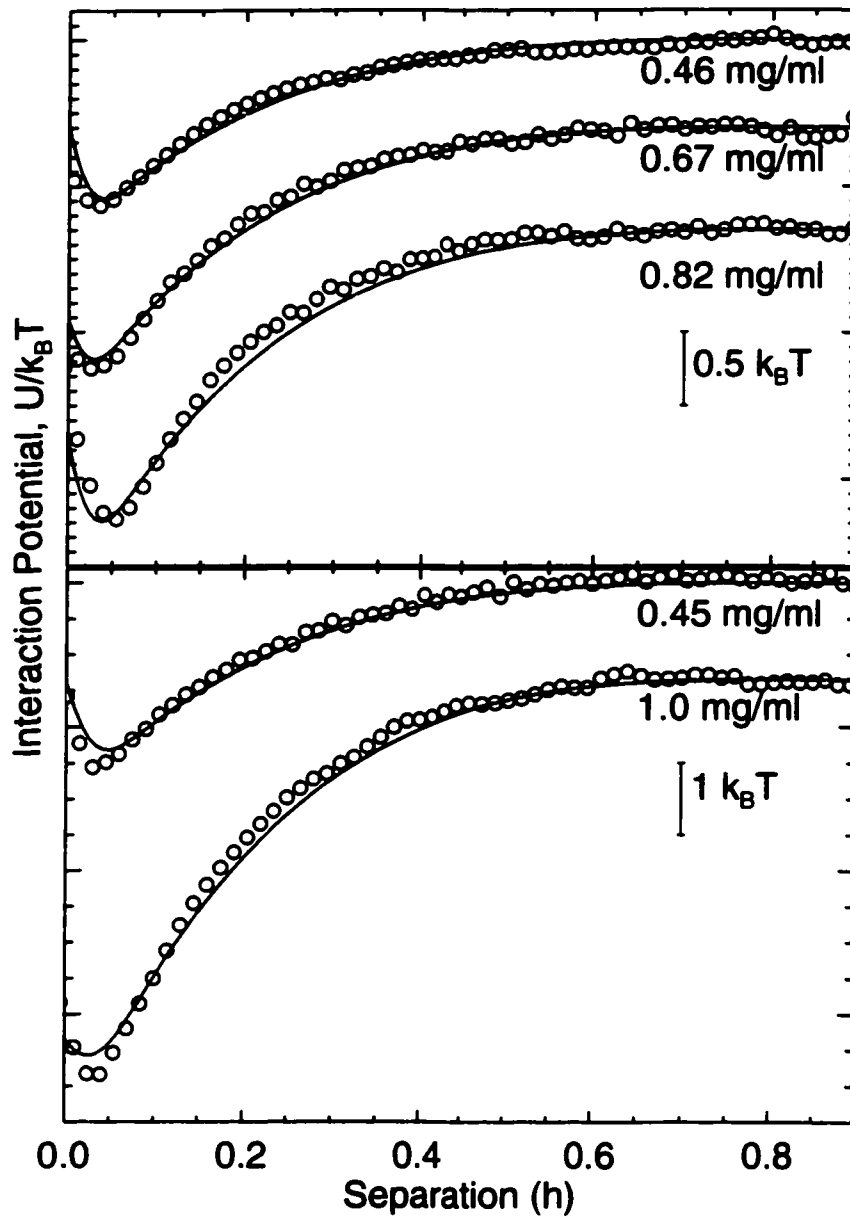


Figure 4.7: Compare YJM-L theory of $L = 920$ nm and $R = 780$ nm with data at given concentration.

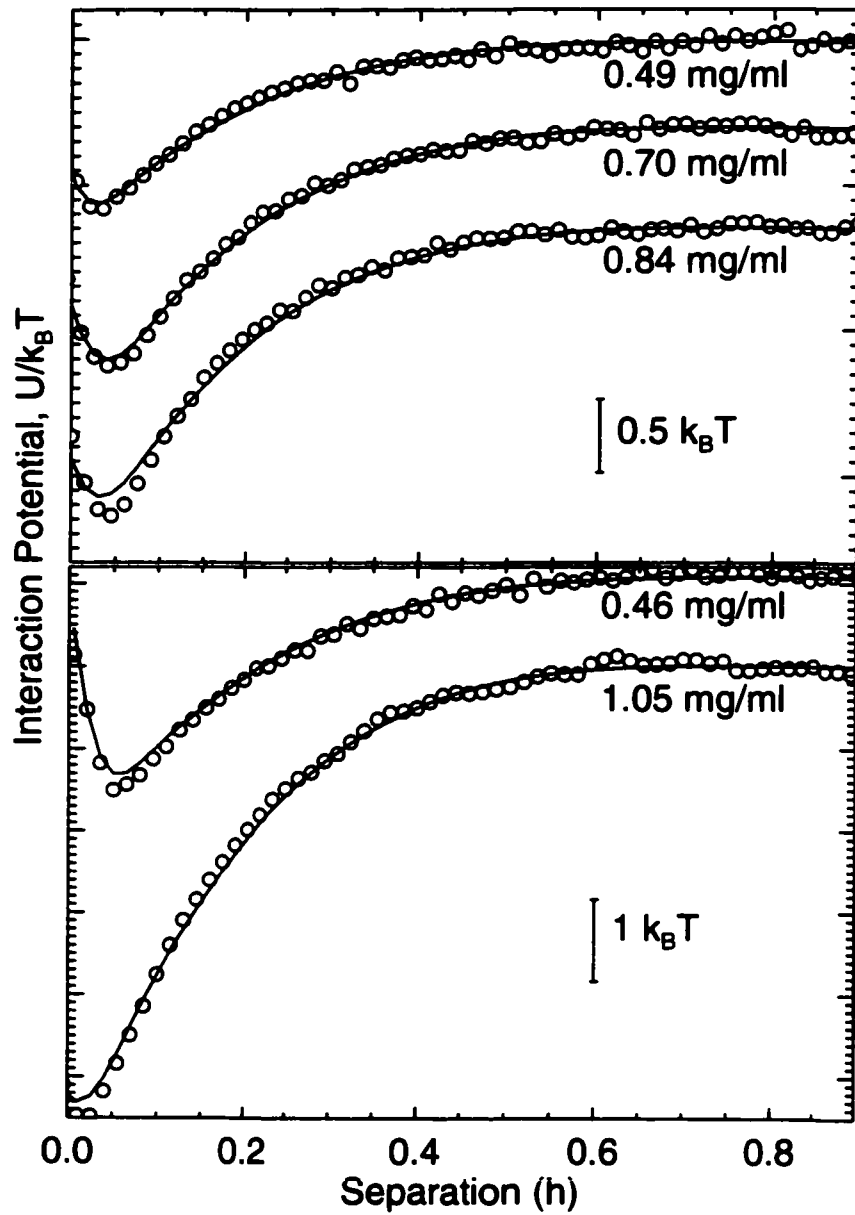


Figure 4.8: Compare YJM-L theory of $L = 900$ nm and $R = 740$ nm with data with tunable concentration.

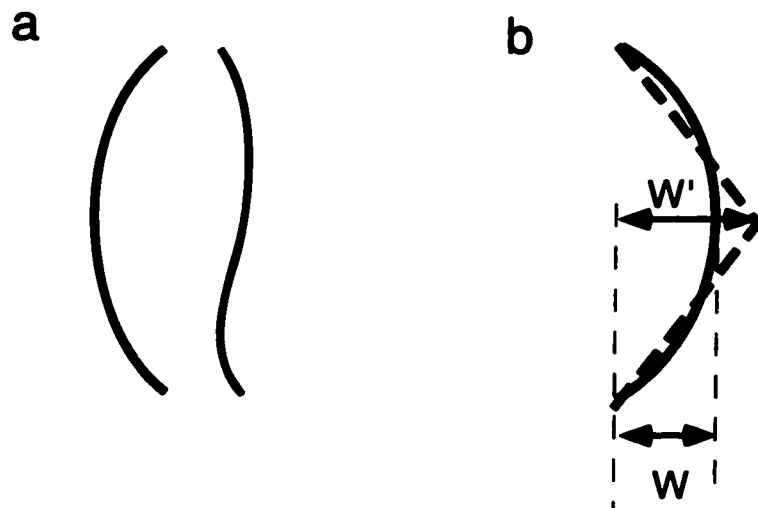


Figure 4.9: The bent rod approximation. (a) different bending mode of semiflexible rods. (b) With the same R and L the bent rod transverse amplitude W' is larger than the arc shape rod W generally by 10 – 20%.

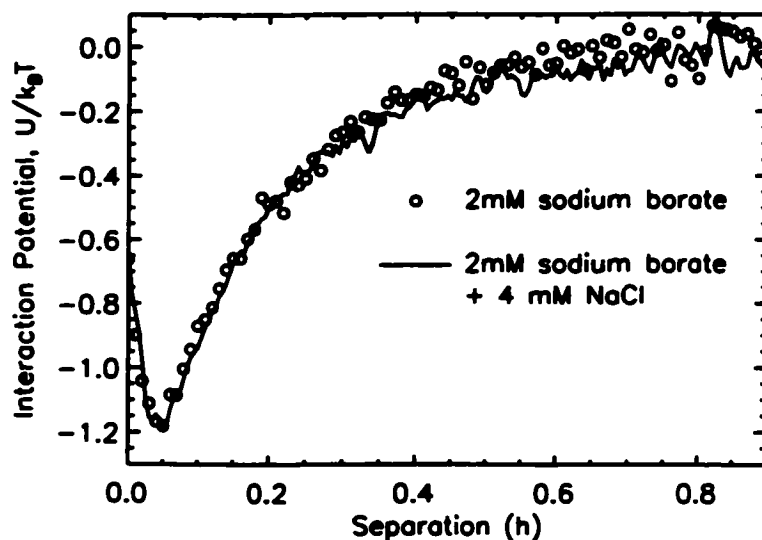


Figure 4.10: Depletion Attraction Potentials at Different Ionic Strength

4.3 Salt Concentration in Buffer

We next explored how variation of the effective rod diameter alters the depletion potential. To this end, we changed the Debye screening length, κ^{-1} , from 16 nm to 3 nm; which in turn modified the effective rod diameter $D_{\text{eff}} = D + 2\kappa^{-1}$, changing the ratio L/D of the rods. Specifically, we varied the NaCl concentration between 0 and 10 mM at constant 2 mM sodium borate and pH 8.0. Our measurements (Fig. 4.10) found no change in the depletion attraction over this range of salt concentration, suggesting that the thin rod approximation holds in our system. Moreover, this confirms the electrostatic interactions between the spheres and the rods are insignificant in this range.

4.4 Sticky Rods on the Spheres

At still higher salt concentrations (i.e. > 20 mM), the spheres in a pure buffer solution become sticky and the sphere-sphere interaction in the rod solution changes dramatically, becoming repulsive. We speculate this repulsion is due to the fd molecules adhering (perhaps end-on) to the particle surfaces. The major coat protein along the fd-cylinder is highly negatively charged, making adsorption there more difficult than for the ends. The composition of the ends is different; one end of fd is the G3P minor coat protein whose function is to grab the pili of *E. coli*, the other end is hydrophobic.

In Fig.4.11 (a) and (b) we illustrate the two types of repulsive interactions we have observed—linear and harmonic. In Fig. 4.11(a) we exhibit two potentials. Both decay in a linear fashion with increasing separation and have a range approximately equal to the length of the virus, L . Although both of these potentials are repulsive and have the same range, the force between the spheres is quite different in the two cases. i.e. (x) 29.4 ± 0.03 femtoNewton (fN) and (y) 5.9 ± 0.04 fN respectively. One explanation for this difference is that a different number of virus are bound to the particles in each case. In Fig. 3(b) we observe a more harmonic interaction, which we hypothesize is due to fd bridging between the spheres. The maximum separation between the spheres was L and the potential minimum occurred at $h = 0.57 \mu\text{m}$. For $h < 0.57 \mu\text{m}$, the potential is approximately linear as in Fig. 3a. For $h > 0.57 \mu\text{m}$, the potential is well fit by a quadratic form, giving a spring constant of $84 k_B T / \mu\text{m}^2$.

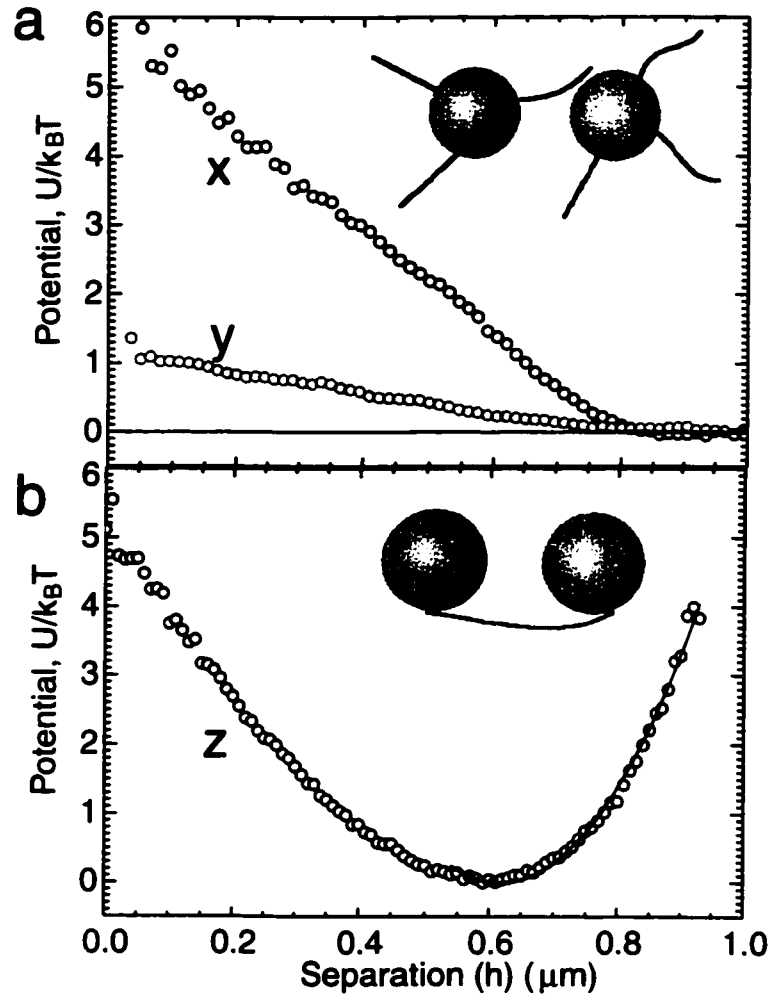


Figure 4.11: x is derived from samples with 2mM Sodium Borate + 10 mM NaCl, 0.5 mg/ml fd and the two other potentials are derived from samples with 10mM TE + 20 mM NaCl, 0.2 mg/ml fd and (a) Steric repulsion between particles due to the 'rod brush'. (b) Harmonic interaction potential due to bridging of fd between two spheres.

Understanding these harmonic interactions from the microscopic properties of the rods will require further effort. Still, this methodology provides a new window into the equilibrium mechanical properties of single macromolecular rods.

4.5 Measurement at Higher Concentration

The sphere depletion interaction has been used to probe the liquid structure of small spheres around the big spheres [141]. The depletion interaction exhibits oscillatory shape with repulsive peaks and attractive wells. In rod depletion interactions it was first suggested [138] that a large repulsive barrier may occur in the intermediate-to-high concentration to second order in perturbation theory. But when they considered third order perturbations, the conclusion was quite different – there was no significant energy barrier in the intermediate-to-high concentration.

We attempted to measure the interaction near and below the isotropic-cholesteric (I/C) phase transition (~ 10 mg/ml). However, there are few problems. First, fd increased the viscosity and index of refraction of the solution significantly. It was harder to trap the particles in place in the same power and the change in index of refraction makes the differential measurement less reliable. Second when it is below the I-C transition point, the particles tend to stick together forever. For first order perturbation theory, the estimated contact potential at 6 mg/ml for 1 micron particles is $\sim 9 k_B T$. This deep potential makes the time needed for measurements too long,

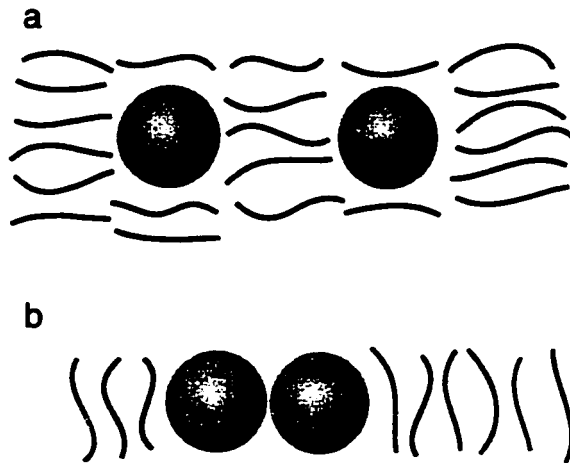


Figure 4.12: Schematic drawing of spheres in nematic rod suspension: (a) The spheres can be stabilized by one rod separation apart. (b) Strong attraction between spheres due to strong surface tension of rods in parallel.

or causes the particle fall into the deep potential due van der Waal interaction. When the concentration is in the cholesteric phase, we sometimes observed that particles separated by about one micron and stabilize for a while before they stick together permanently. The possible scenario is illustrated in Fig. 4.12.

4.6 Conclusion

We have presented the first measurements of interactions between particles in rod-like suspensions. Our results are well approximated by the YJM-KP model [21], which takes both sphere and rod curvature into account. The remaining deviations at small separation are due to non-negligible contributions from the entropy of bent rod conformations, which until our work have not been considered in the literature. The

YJM-L model provides an excellent agreement with data and predicts a surprisingly smaller ℓ_p than the literature value. Thus the depletion interaction measurement provides an independent measurement on persistence length. There is no obvious artifact from sample preparation and it does not require complicated theoretical model for hydrodynamic interactions of a semi-flexible polymer. Our result suggests more experiments should be carried out to re-examine the value of persistence length of fd and also provides another way to check the statistical properties of semi-flexible polymers.

We also observed steric repulsion and bridging effects at high salt conditions. In total, these observations can be used to understand the phase behavior and stability of these and related suspensions, and to gain insight into the mechanical behavior of macromolecules.

Chapter 5

Entropically Driven Colloidal Crystallization on Patterned Surfaces

In this chapter we describe a novel colloidal system that enable us to two-dimensional phase transitions and also provides a new approach for colloidal epitaxy based on equilibrium thermodynamics and geometry.

We use patterned surfaces with spatially periodic 1D- and 2D-height profiles as templates to nucleate the growth of two- and three-dimensional structures. Depletion effects in suspensions of large and small particles of macromolecules produce forces that push large spheres together [142], towards flat walls [143], and towards inner corners on surfaces [144]. We use these forces to attract and repel colloidal spheres from specific positions on the corrugated template.

We observed the formation of 1D, 2D, and 3D commensurate structures as a function of sphere size and grating periodicity. Our experiments complement recent work on charged 2D colloidal phase transitions in a perturbing 1D optical potential [69, 70, 74]. Our particle interactions are, however, short ranged, and are much

weaker than the external template potentials. Our surface particle density is set by its equilibrium at constant chemical potential with the bulk (3D) colloidal liquid. The 1D line grating creates a surface potential for the colloids that induced 2D structures, all of which exhibit diffuse scattering peaks characteristic of 2D bond-angle ordered phases in an aligning field rather than power-law peaks characteristic of 2D crystal order. They thus correspond to the liquid phases of [70]. The 2D crossed grating, surface potential induced both liquid- and solid-like structures, and provided the optimum template for growth of a large, defect-free FCC crystal in 3D. Finally we created a template of FCC(100) with lattice spacing $d = 1.15\sigma$ where σ is the diameter of hard sphere. The substrate induces an expanding FCC crystal at $\sim 50\%$ which is below than bulk freezing point. As the system's osmotic pressure increases, a comensurate-incomensurate transition is observed. At very high osmotic pressure, the system eventually turn into hexagonal close packed structures.

5.1 Depletion Interaction and Surface Structure

In chapter 2 we discussed the depletion interaction between two spheres. The same attraction occurs between sphere and wall as shown in Fig 5.1. At contact, the overlapping excluded volume between the wall and sphere is almost twice as great as the overlapping excluded volume between two spheres in contact. This explains why crystal growth using depletion interaction normally occurs in the bulk suspension at

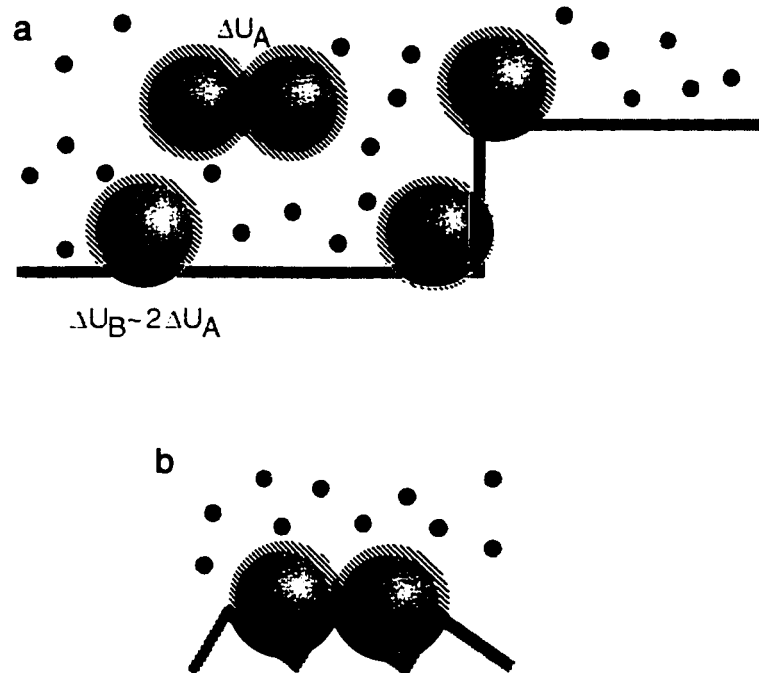


Figure 5.1: (a) The hashed region represents the volume excluded to depletants. The dark region is the overlapped excluded volume. In flat wall and corner geometries, the overlapping excluded volumes are bigger than between spheres. (b) Colloids are driven to the grating grooves due to depletion interaction.

the wall, especially, when the concentrations are chosen close to the phase boundary.

The dependence of depletion interaction energetics on large scale geometric structure was systematically studied in Tony Dinsmore's thesis. He showed that spheres preferentially lined up along the corner on silicon substrates [144], are repelled from step edges [145], and are attracted to regions of higher curvature in walls [146]. He also proposed that an array of 2D posts can be used as a template to crystallize particles by depletion. We demonstrate the feasibility of this idea by positioning colloids using various periodic surface topologies.

5.2 Sample Preparation

To create the geometrical templates, we have employed the imprint technique discussed in chapter 3 using optical diffraction gratings.

The colloids consisted of 0.7 to 1.2 μm diameter PMMA (polymethylmethacrylate) spheres stabilized by a grafted layer of poly-12-hydroxystearic acid. [86, 4]. In a mixture of decalin and cycloheptyl-bromide, these spheres are nearly density matched and have a refractive index mismatch of < 0.01 with respect to the solvent. Such small index mismatches reduce light scattering, which facilitates optical microscopy deep into the suspension. However, it also results in low imaging contrast in the bright field. We used phase contrast and confocal microscopy to observe the resulting 2D and 3D structures, respectively. Both techniques are reviewed in chapter 3.

Depletion attraction was induced by adding polystyrene microspheres with $R_g \approx 15$ nm ($M_w = 320000$, $M_w/M_n = 1.04$, Polymer Laboratories) to the suspension of particles. The PMMA/PS mixture has been thoroughly investigated by Pusey's group [4]. A typical bulk phase diagram is shown in Fig. 5.2. A fluid-solid phase transition due to binary sphere depletion on a flat hard wall was investigated in reference [5]. It was shown that the surface crystal is best grown near the fluid-solid coexistence line. In our experiments, we tuned the bulk concentration to just below the fluid-solid coexistence region and adjusted the polymer concentration to keep the free energy of the system fairly constant as we varied the spatial period p

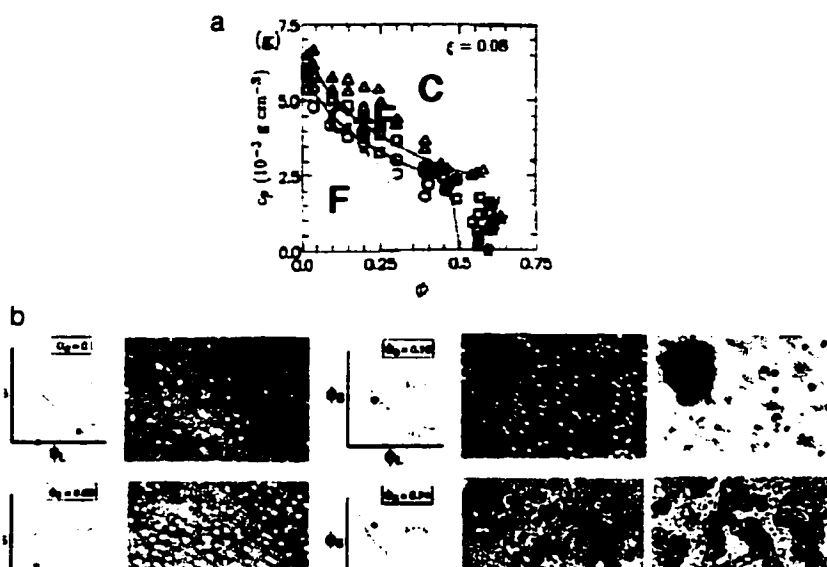


Figure 5.2: (a) typical bulk phase diagram of spheres and polymer [4]. (b) The phases on a flat surface with corresponding the bulk phases [5].

of the template and the sphere size. Two dimensional surface structures formed in approximately one hour and evolved very slowly thereafter. The number density and growth rate depended on bulk concentration of colloids and polymer. They exhibited local density inhomogeneities and defects whose positions were quenched over the lifetime of the experiments.

5.3 Line Grating Templates

The interplay between bulk particle volume fraction, Φ , bulk polymer concentration, C_P , and mean nearest neighbor spacing, d , is most clearly exhibited by the 1D colloidal liquids that form in the grooves of the 1D grating template. The simplest case arises when the spheres are large enough to fill the groove, but not large enough to

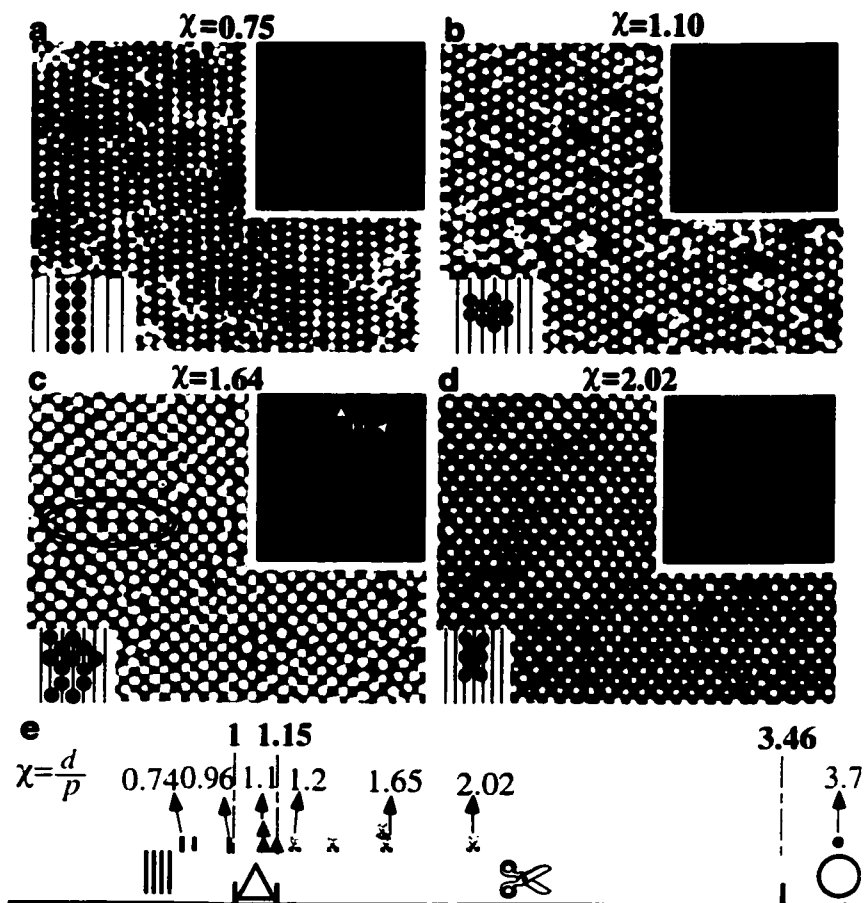


Figure 5.3: Phase-contrast micrographs of four representative 2D structures with the schematic reconstruction in the bottom left corner. The $S(k)$ computed from these images is shown in the top right corner. (A) Stripe phase. (B) Triangular phase. (C), (D) Scissor (Centered-Rectangular) phases with different scissor angles as defined in the structure function image of (C). In (C) we circle the mirror line of a twinning defect. (E) Diagram indicating the observed phases as a function of χ .

interact with spheres in adjacent grooves. Our observations of self-assembled crystal structures on the line gratings are displayed along with the corresponding structure function, $S(\mathbf{k})$, in Fig. 5.3. The 1D liquid phase (i.e. stripe phase) is shown in Fig. 5.3a. and its pair correlation function along the groove, $g(r)$, is plotted in Fig. 5.4a for three different combinations of Φ and C_P . We derived an approximate bulk phase-diagram for this system based on [4] (see the inset of Fig. 5.3). At low volume fraction Φ and low polymer concentration $C_P(Y)$, the first peak position is significantly larger than $2a$. This suggests that there may be repulsive interaction between the spheres since the first peak position should be the diameter of the sphere for a hard sphere liquid. However, at low particle volume fraction, Φ , and high polymer concentration $C_P(Z)$, the measured pair correlation function $g(r)$ exhibited peaks whose positions were asymmetric, like those of a classical hard-core gas [147]. Its magnitude, however, decayed more rapidly toward 1 at large r than the hard core gas shown in Fig. 5.4b. Thus the short-range depletion attraction may be the dominant interaction in this case. At higher concentration Φ and lower concentration $C_P(X)$ the peak positions are comparable to Y, with slower decay at large r . However, the peak shape is more symmetric. The structure function analysis shows that there is small coupling between neighboring grooves caused either by coupling to defects or by coupling colloidal particles in the bulk. At higher concentrations the mean nearest-neighbor spacing, d , derived from the first peak in $g(r)$, shifted to smaller values. The typical

spacing was larger than the depletion interaction range, about 1.1 particle diameters. These observations suggest that the surface density of spheres is determined by the competition of the depletion attractions driving the spheres to the surface and the osmotic pressure of the spheres already there.

When the sphere diameter increases relative to the spatial period of the grating p , the 1D colloidal liquids in adjacent rows interact more strongly. The most important parameter characterizing the 2D phase behavior is the commensurability ratio, $\chi = d/p$, where d is derived from the pair correlation function along the groove. For the phases in Fig. 5.3, $\Phi = 0.25$ is high enough to serve as a reservoir for surface adsorption. C_P was set near the *bulk* fluid-crystal phase transition region (point 'X' in Fig. 5.4). This choice ensured that bulk crystallization did not occur in our thin sample chambers and that the spheres densely covered the template surface. On flat substrates at the same concentration, the colloids formed isotropic liquid structures. The line grating breaks the symmetry in one direction and the assembled structures exhibit a range of two-dimensional patterns shown in Fig. 5.5. Generally, the 2D colloidal structures on the line-grating surfaces do not exhibit very long range translational order along the groove direction. Point defects and dislocations are common, as are twinning planes perpendicular to the groove direction (see Fig. 5.3C).

When the sphere size is bigger than the groove pitch, more particles can be packed onto the grooves through the interlacing of spheres in different grooves. For $1 < \chi <$

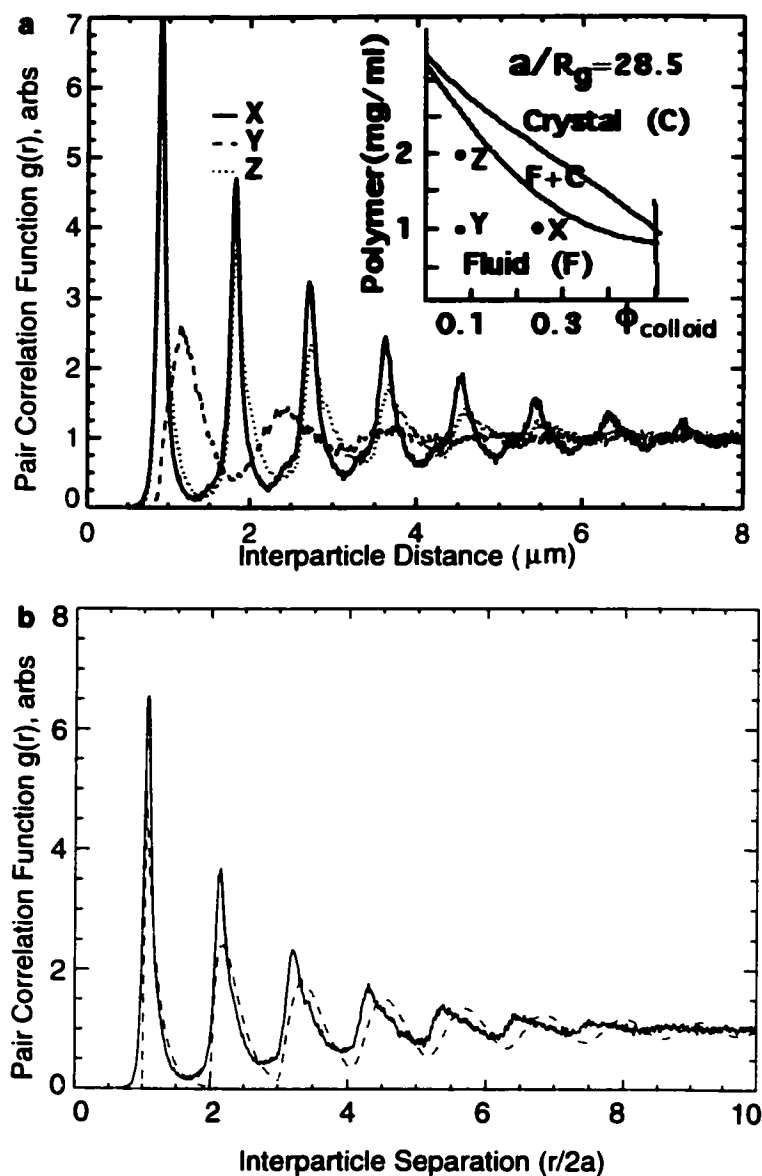


Figure 5.4: (a) 1D pair correlation function along the groove direction for colloidal spheres in the stripe phase ($2a = 0.86 \mu\text{m}$, $p = 1.21 \mu\text{m}$, see Fig. 5.3a). For curve X, the first peak of $g(r)$ occurs at $r = 0.93 \mu\text{m}$. The inset is the approximate bulk phase diagram scaled from [4] for this system as a function of Φ and C_P . (b) The comparison of $g(r)$ (dashed-line) of Z to the exact 1D hard-sphere correlation function (solid-line).

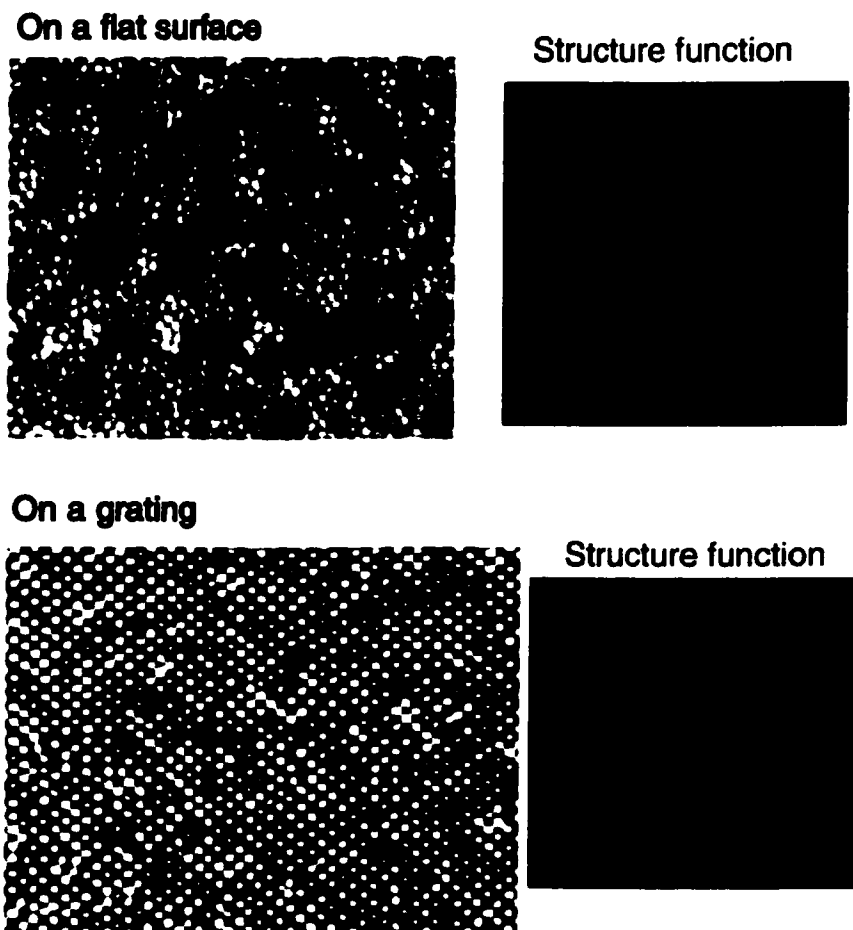


Figure 5.5: At the bulk same concentration, the structure on the flat surface and on a line grating template.

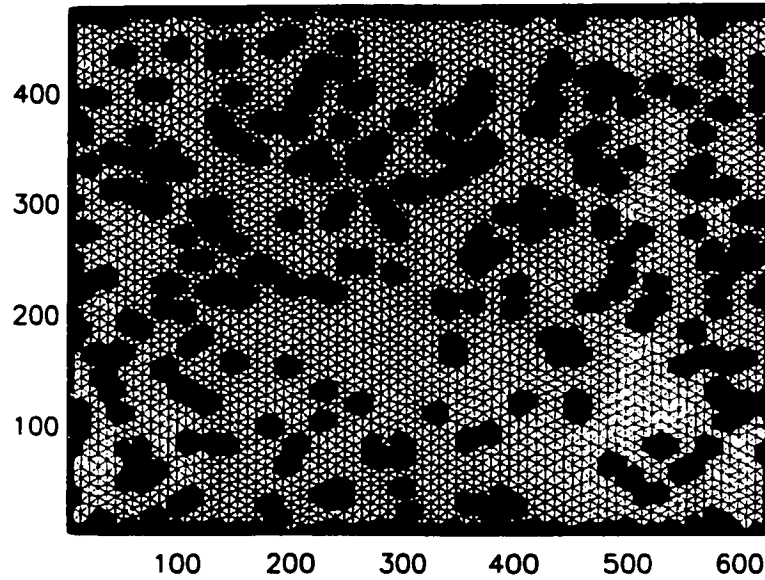


Figure 5.6: Bond orientation order of the triangular phases.

$2/\sqrt{3} = 1.15$ (see Fig. 5.3b), the spheres can have nearest neighbors along the same groove and in the neighboring grooves. Hexagonally symmetric crystals emerge. As χ increases towards 1.15, this structure becomes more ordered. Fig. 5.6a shows the Delauney triangulation with disclination neighbors shaded. The defects are usually connected to each other which shows long range orientation order.

For $1.15 < \chi < 2\sqrt{3} = 3.46$, the ordered structure is maintained while hexagonal symmetry gives way to crystals with centered rectangular unit cells (see Figs. 5.3c.d). Two dimensional phases with centered rectangular symmetry have not been previously observed [69, 70]. We define the scissor angle, θ , as the angle between the grating groove direction and the crystal lattice vector (see Fig. 5.3C), and refer to the centered rectangular phase as the scissor phase. Using the geometric relation

$\tan \theta = 2p/d$, we again find the mean nearest neighbor spacing is $\approx 10\%$ bigger than the sphere diameter. A peculiar kind of defect twinning is often observed in this phase after a long time (See Fig. 5.3c and its inset).

To better understand the nature of these phases, we examined the shape of the peaks in the structure function, $S(\mathbf{k})$. It exhibits resolution-limited Bragg peaks, arising from the periodic template, at $k_y = 0$ and $k_x = nG_x$, where $G_x = 2\pi/p$ and n is an integer, and diffuse peaks along the lines $k_y = mG_y$ with m an integer, where $G_y = 2\pi/d$, reflecting correlations within and between grooves. Fig. 5.7 shows the structure function for different phases. The diffuse peaks become sharper in the scissor phase. The intensities as a function of k_x at $k_y = mG_y$ are well-described for all $m \neq 0$ and χ by

$$S_m(k_x) = \frac{A_m e^{-k_x^2 W_m}}{1 + C_m \cos(k_x p)} + B_m, \quad (5.1)$$

which exhibits Lorentzian peaks of width $2(1 - |C_m|)/p^2|C_m|$ at k_x equal to odd multiples of $G_x/2$ for $C_m > 0$ and to even multiples of $G_x/2$ for $C_m < 0$. This is the scattering function for a model system in which a 1D liquid in each groove interacts weakly with the 1D liquids in its nearest-neighbor grooves. Within this model, W_m is a Debye-Waller factor arising from uncorrelated motion of spheres perpendicular to the grooves, C_m is proportional to the product of interparticle potential at wavenumber $k_y = mG_y$ and the structure factor $S_{1D}(mG_y)$ of the spheres along an isolated groove,

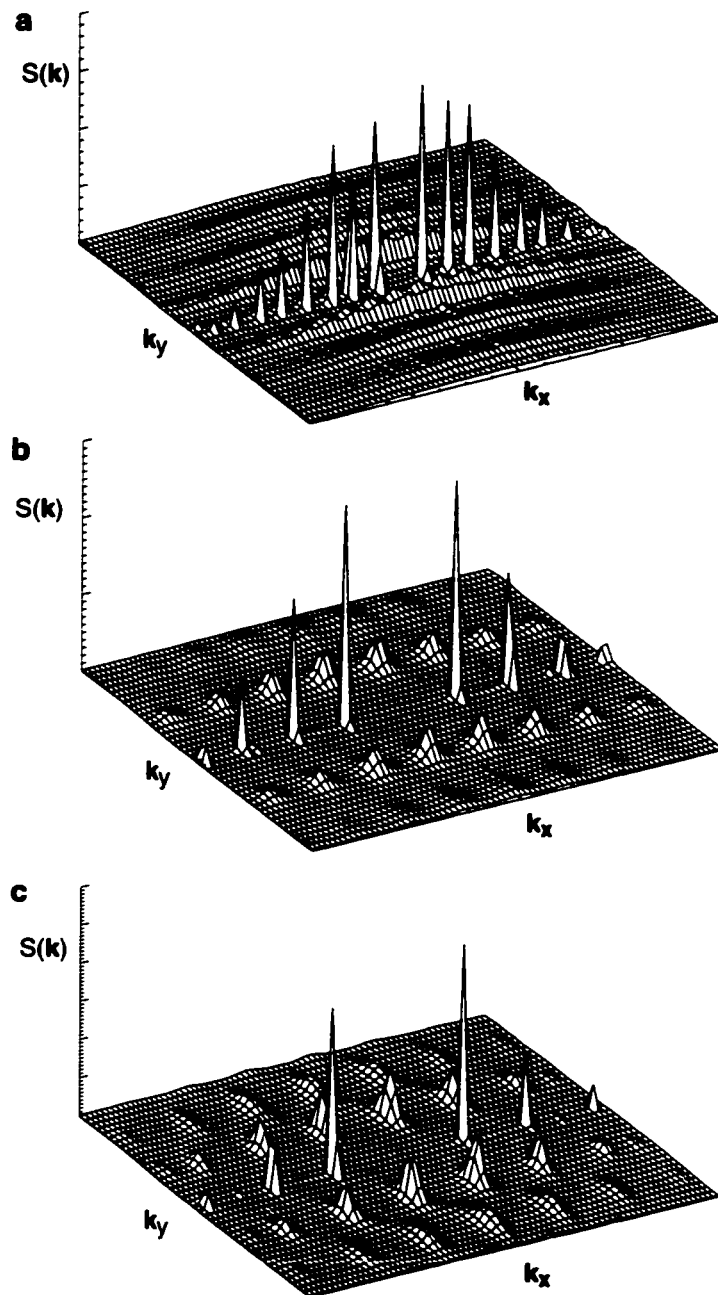


Figure 5.7: The structure function $S(\mathbf{k})$ plotted in the xy plane for three different phases (a) stripe, (b) hexagonal and (c) scissor.

A_m is an amplitude proportional to $S_{1D}(mG_y)$, and B_m is a background. In the stripe phase, there is short-range simple rectangular order (see Fig.2A), and $S_m(k_x)$ exhibits diffuse peaks at $k_x = nG_x$ for $m = 1$ and $m = 2$ described by Eq. (5.1) with $C_m < 0$, corresponding to attractive interactions between spheres in neighboring grooves. The ratio C_1/C_2 is equal within experimental error to $S_{1D}(G_y)/S_{1D}(2G_y)$ determined by direct measurement of the 1D structure function of a line, in agreement with the model of weakly interacting 1D liquids. As the density is increased, centered rectangular (or hexagonal) correlations become more pronounced, and the structure function peaks become those of a centered rectangular reciprocal lattice at $k_x = (n + \frac{1}{2})G_x$ for m odd and $k_x = nG_x$ for m even. We observed this effect in the scissor and hexagonal phases, whose structure functions are well-described by Eq. (5.1) (even though the inter-groove coupling is no longer weak) with $C_m > 0$ for m odd and $C_m < 0$ for m even. A similar structure function results when unbound or quenched dislocations convert the power-law Bragg peaks of the “locked floating solid” phase of Ref. [74] to Lorentzian peaks in the liquid phase. In our experiments, W_n was approximately constant, and $|C_m|$ decreased with increasing m in all phases. The decay of $|C_m|$ was slower in the scissor phase than in the hexagonal phase.

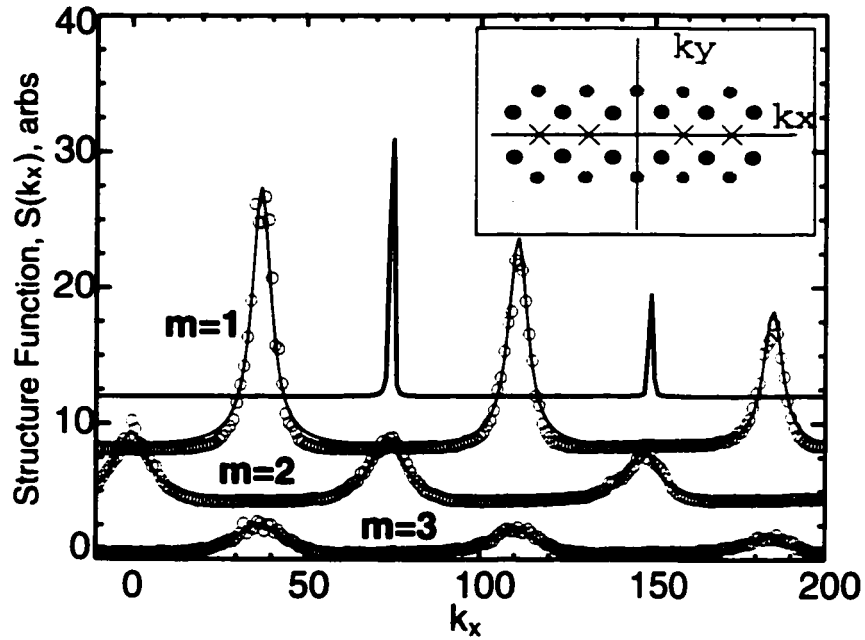


Figure 5.8: $S(k)$ for the centered rectangular phase shown in Fig. 5.3C. The peak positions are indicated in the inset. The \times 's indicate delta-function Bragg peaks and circles indicate Lorentzian-like peaks. The grooves are aligned parallel to the Y-axis, and plot $S(k)$ vs k_x , at four different values of k_y . The topmost row shows the Bragg-peaks (i.e., at $k_y = 0$) scaled $50 \times$ smaller. For non-zero k_y , the curves are well modeled by Eq. 5.1 (solid curves).

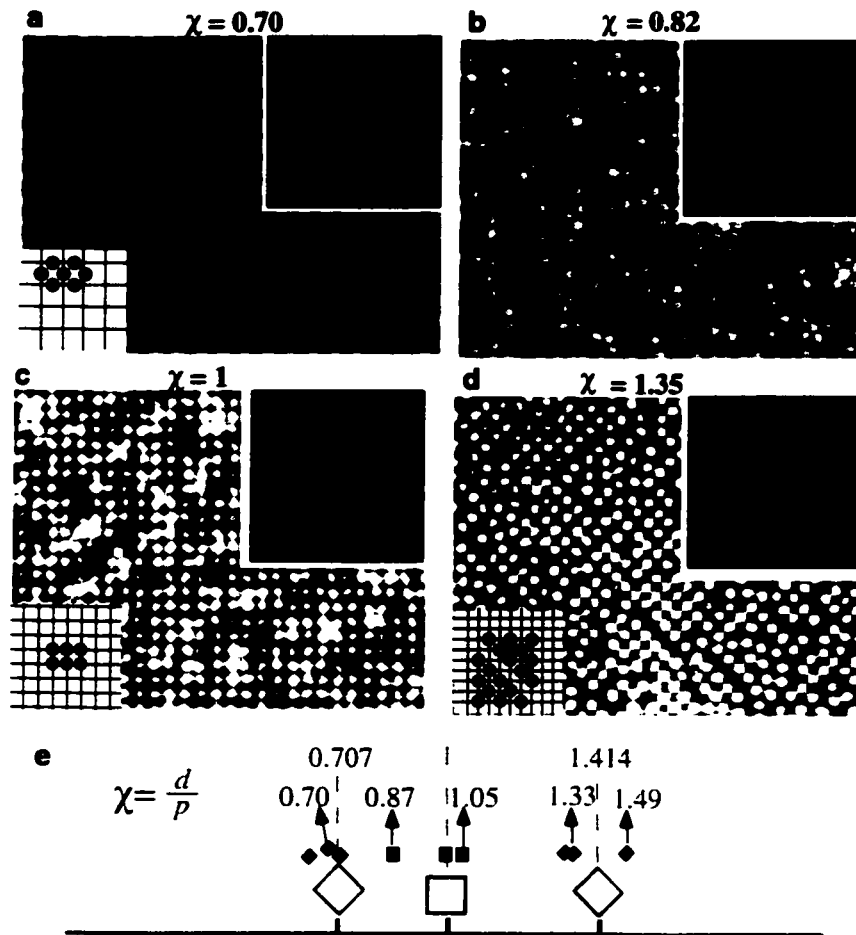


Figure 5.9: (a), (b) and (d) illustrate 2D colloidal assembly commensurate with the cross grating template. Notice that the crystal orientation rotates by 45 degrees for $\chi = 0.71, 1.41$, and that different crystal domains are clearly seen in (c). The domain size in (b) is greater than the microscope field of view which is $60 \mu\text{m} \times 80 \mu\text{m}$. (c) shows the disorder structure when χ is far away from the commensurate value.

5.4 Crossed Gratings

The crossed gratings impose a 2D surface potential on the colloidal suspensions. Since the crossed-gratings have two-dimensional square symmetry, we expect the assembled structures to have this symmetry. All the ordered patterns have square symmetry, but with different lattice constants and orientation. (See Fig. 5.9). Here $d = 1/\sqrt{\sigma}$, where σ is the particle surface density. When $\chi \sim 1/\sqrt{2} \approx 0.71$, a commensurate overlay FCC(100) $1/\sqrt{2} \times 1/\sqrt{2}$ 45° was formed. When $\chi \sim 1$, commensurate structures with FCC(100) 1×1 pattern were formed, and finally for $\chi \approx \sqrt{2} = 1.41$, a commensurate, rotated square structure formed, i.e. FCC(100) $\sqrt{2} \times \sqrt{2}$ 45° . In the latter case large domains did not arise because two possible nucleation sites exist on the template and produce different lattices, corresponding to lattices built on either the black or the white squares of a checker board. When d was commensurate with the pitch at the ratios, 0.71, 1, and 1.41, larger crystal domains with fewer defects formed.

The structure functions for crossed-grating phases had both solid- and liquid-like features. Each phase exhibited Bragg-like peaks on the reciprocal lattice of the template potential along with a ring-like background and diffuse peaks characteristic of a liquid or residual sample disorder. Generally the diffuse peaks were narrower than the corresponding peaks in the 1D potential. When χ deviates from the commensurate values, the liquid-like ring becomes more pronounced.

5.5 3D assembly

A crossed grating commensurate with the FCC(100) plane ($\chi = 1$) was used to grow an FCC crystal without stacking defects. With some density mismatching (e.g. 0.3 g/cm³ difference), the growth process was enhanced by a gravity-induced increase in sphere concentration near the surface. The spheres then crystallized faster and grew more than 30 layers. In contrast to previous sedimentation-based assembly [96], control experiments without polymer did not produce large ordered colloidal crystals (Fig. 5.10b and c) probably because the energy difference between the top and the bottom of the groove is only $0.2 k_B T$ ($3\times$ less than [96] and $20\times$ less than with the depletion effect). Nevertheless after > 24 hours a few layers of crystal nucleated.

We employed a 2D bond orientation parameter Φ_4 to analyze the defect structure layer by layer. In the square cell, it is best to use a voronoi diagram instead of triangulation (see Fig. 5.11a). We only include the long edges of voronoi cell which divide the particle from the nearest neighbors. The most common defect is a void with the characteristic shape of a cross composed of 4 pentagons in the voronoi cell analysis.

5.6 Expanded FCC(100) Lattice

With the waffle templates, it is possible to study crystallization on a square lattice template with small χ . While on crossed grating of small χ , liquid-like structure is

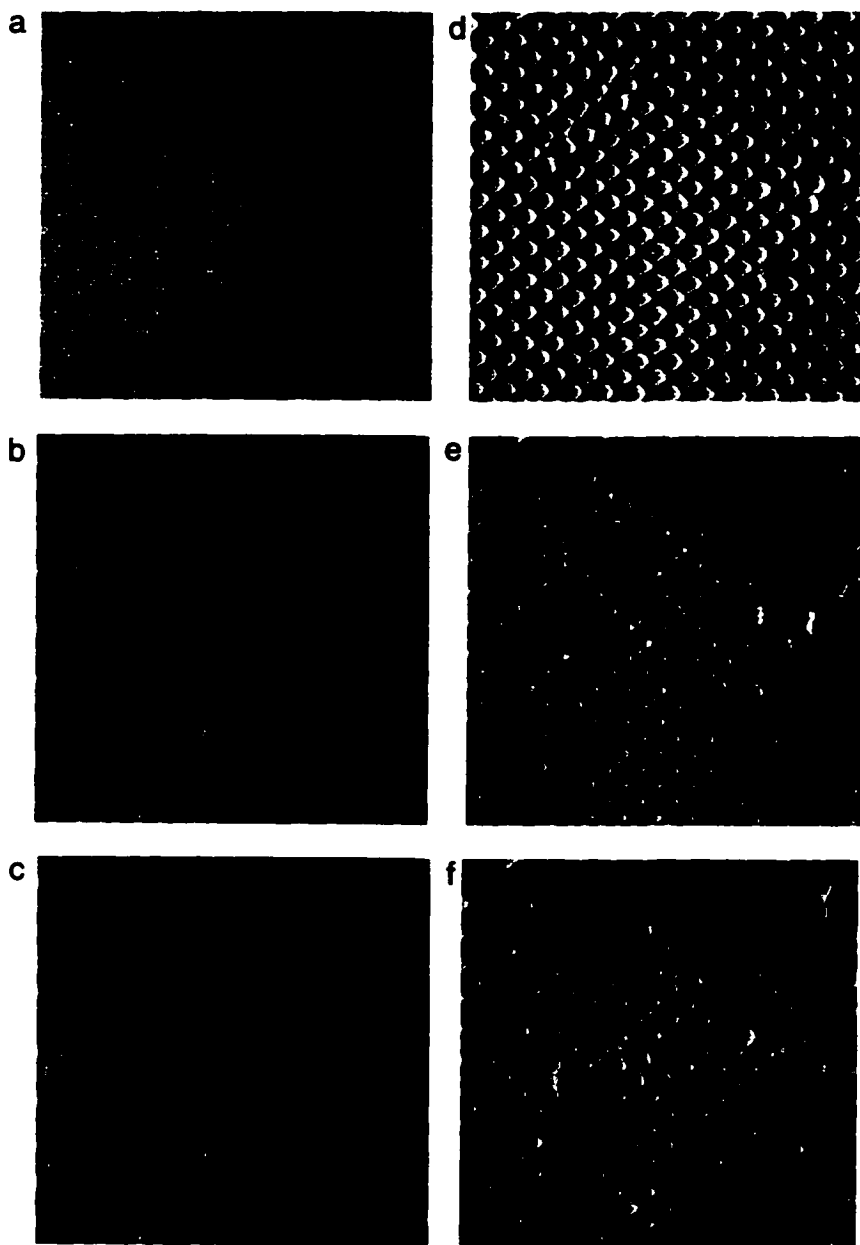


Figure 5.10: (a) fluorescent picture of a crossed grating template. (b), (c) DIC pictures of particles sediments on the template within few hours. (d), (e) and (f) particles sediments with polymer added.

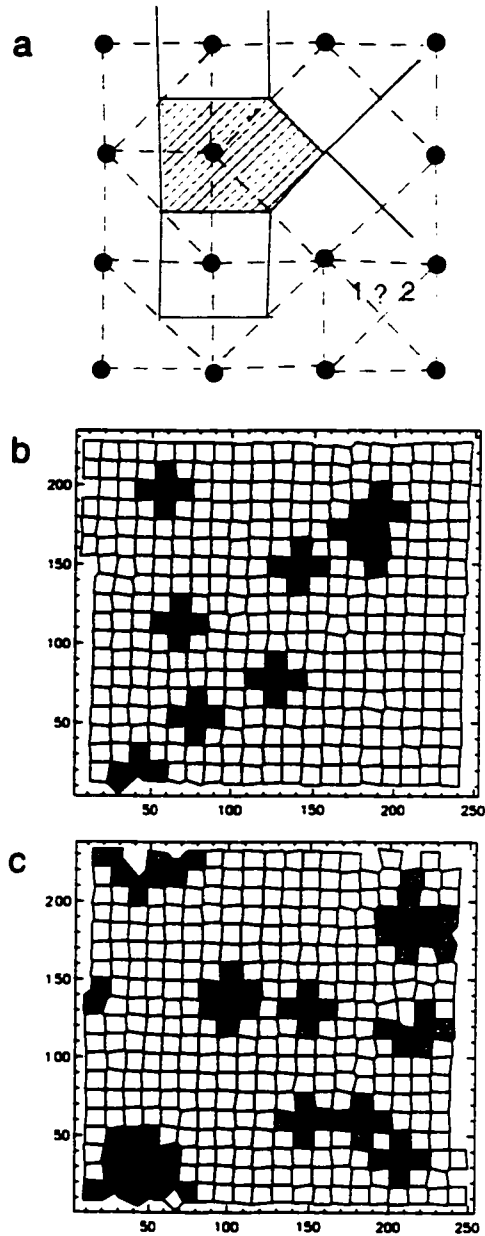


Figure 5.11: (a) The solid lines show a voronoi diagram of square lattice with a void. The shaded pentagon indicates a vononoi cell with a missing lattice point. The dashed lines show Delauney triangulation. In the bottom right it shows that either bond 1 or 2 are allowed because they are the same length. Voronoi diagram gives no ambiguity in the square lattice analysis. (b) and (c) are the voronoi diagram from the fcc crystal data with shaded region as defects identified by Φ_4 .

more pronounced because colloids can move freely along the grooves on a crossed-grating while colloids nucleate into a monolayer of crystal commensurate with waffle template lattice of small χ . One of the original goals is to create open structures such as a BCC crystal of hard-sphere-like particles. We designed a template with $\chi = 1.13$ (shown in Fig. 5.12).

For our studies, we varied the buoyancy density, volume fraction, and depletion interaction and watched the sample to evolve with time. We observed three stages of crystal structure: (I) commensurate crystals, (II) incommensurate crystals, and (III) random hexagonal packed crystals (see Fig. 5.13). In the commensurate phase (I), the particles register to the template lattice well to the high layer. Fig. 5.14) shows the coordinates of all particles in a commensurate crystal of 24 layers projected onto xy and xz plane. The projected particle positions maintain well periodic positions of a crystal. The area distribution of voronoi cells in each layer are almost the same and the average bond orientation order parameter Ψ_4 for each layer is between 0.7-0.8. In the incommensurate phase (II), crystals with domain boundaries are observed. The particles lose registration from the template. In the plots of projected coordinate (Fig. 5.15), there are regions exhibiting particles more scattered from a crystal lattice because of domain boundary. There should be misfit dislocation line introduced in the system and more work is required to identify this type of defect. In the stage (III) of random hexagonal packed crystal, the structure above the template not only lose the

spacing registration to the substrate but also lose the orientational symmetry. The colloids turn into hexagonal packed in each plane. There is a small layer of disordered structure from square substrate layer to the hexagonal plane bulk structure.

We first observed effects due to different buoyancy mismatch ($\Delta\rho$) in the short time. When $\Delta\rho = 0.9$ g/cc with corresponding gravitational length ($\ell_g \sim 0.8\mu\text{m}$), the colloids assemble into random hexagonal packed crystals as in stage III (Fig. 5.16). When $\Delta\rho = 0.2$ g/cc ($\ell_g \sim 3.5\mu\text{m}$), the colloids initially assemble to commensurate crystals as in stage II. When $\Delta\rho = 0.44$ g/cc ($\ell_g \sim 1.6\mu\text{m}$), the colloids may go to incommensurate phase (stage II) without going through stage I¹.

We then observed different initial volume fractions of 0.1 %, 1%, 2% and 10% at $\Delta\rho = 0.2$ g/cc. They exhibit similar behaviors of evolving from stage I to III with different time scale for system evolution. The system evolves faster at higher initial volume fraction. In the beginning there are commensurate crystals grown on the template. Then they turn into incommensurate structures. At the end they all evolve to hexagonal packed crystals.

Even though the system is not in truly equilibrium, there is no well defined overall osmotic pressure for the whole system. It takes a long time to reach real gravitational equilibrium. However, we may understand the system assuming locally the system is in equilibrium. The local osmotic pressure Π of colloidal fluid above the tem-

¹We may miss the observation of stage I at this density mismatch.

plated crystals determines the structure of crystals on the template. As the time goes on the osmotic pressure of colloidal fluid above the template increases through sedimentation. When Π reaches surface freezing point, the fluid crystallizes on the patterned substrate (either on the waffle template or on the crystal facet) as a commensurate crystal. When the osmotic pressure of colloidal fluid is higher than the osmotic pressure of commensurate crystal and also overcomes the interfacial energy, they crystal turns incommensurate structure with higher volume fraction in order to maintain the mechanical balance from pressure above. At the end the planar hexagonal structure is the most stable structure under high osmotic pressure with gravity. This can be confirmed from local volume fraction measurement. ϕ is between 50-54% for stage (I), 54-58% for stage (II) and more than 60% for stage III. The crystal osmotic pressure must balance the pressure from the fluid to maintain the structure (Fig. 2.10). The lower volume fraction of commensurate crystal than bulk freezing point 54.5% suggests that a surface induced phase transition happens on a patterned substrate[17, 148].

We examined the correlation function and the ratio of the interparticle separation d in one plane to the interplane separation h (Fig. 5.12) to have more quantitative measures on the crystal structure. Fig. 5.18 shows that $g(r)$ of the commensurate crystal (stage I) on the template is close to FCC crystal instead of BCC. However, we have data showing the other way which may suggest there exist a range of body

center tetragonal (BCT) crystal under different conditions. However, a more accurate z calibration is necessary to determine the exact structural relation.

We also add polymer into the system to induce the attraction between particles. The polymer increase the osmotic pressure of the system and accelerates the crystallization process. However, $h/d = 0.62$ is close to BCC ration when 0.2 mg/ml polystyrene of m.w. 3,390,000 was added. The depletion interaction decrease the interplane spacing. Fig. 5.15 shows the position of particles on xy plane and xz plane of stage II crystal. Particles lose their registry from one layer to another.

5.7 Conclusion

To conclude, we have reported on a rich variety of 2D self-assembly phenomena generated by varying colloidal composition, addition of polymers, and engineering entropic surface potentials. The combination of depletion attraction and a simple, robust surface templating scheme provided a qualitatively new route for controlled colloidal self-assembly in 3D. Since the entropic techniques used here are not restricted to micron size particles, the underlying principles should be applicable on smaller, macromolecular length scales. The preliminary results of 3D assembly on BCC-like templates show interesting crystal growth dynamics. A better understanding of the relevant parameters for crystal growth can open the possibility of novel crystal structures.

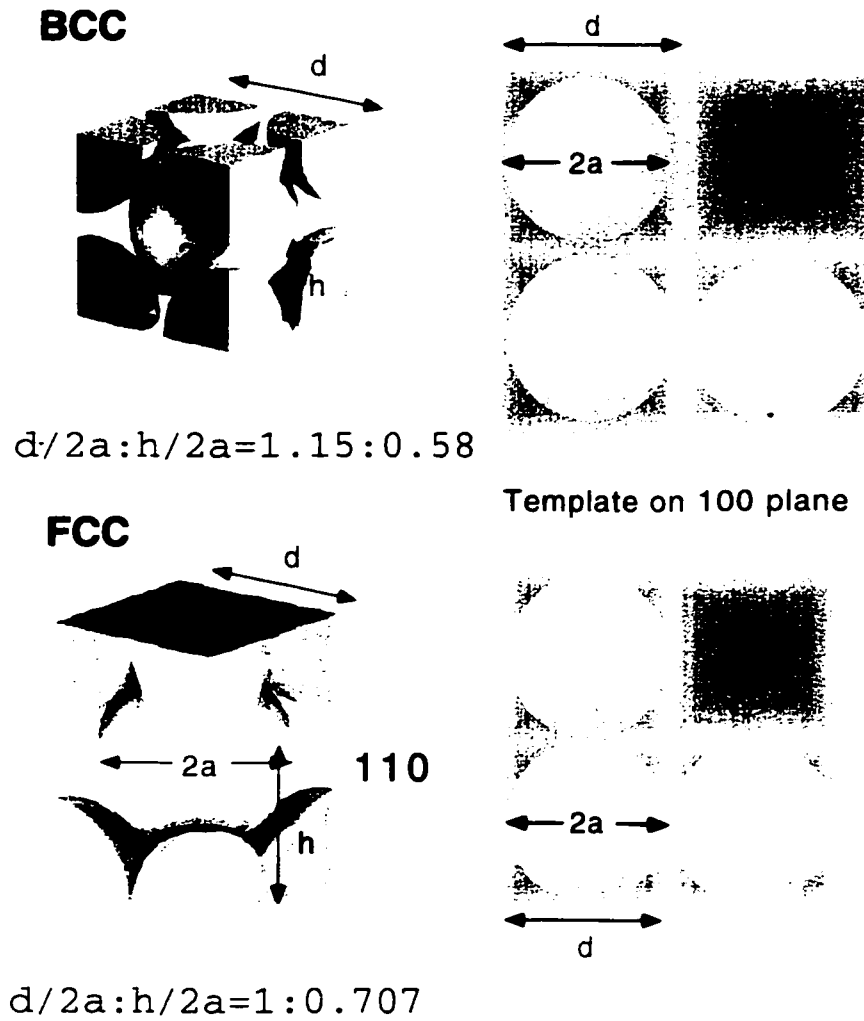


Figure 5.12: The comparison of particle spacing between FCC and BCC crystals.

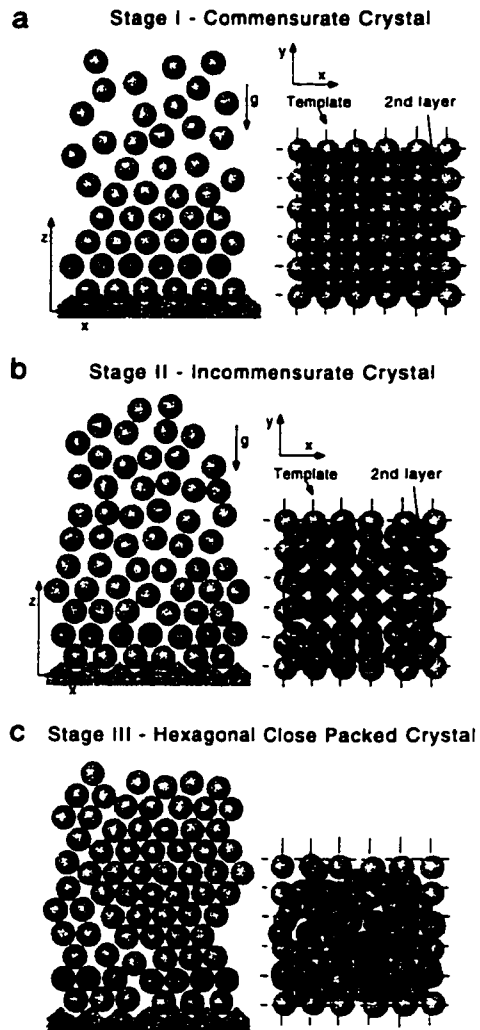


Figure 5.13: Three stages of crystal formation observed: (I) at lower ϕ a crystal commensurate with the template; (II) at intermediate ϕ a crystal with square symmetry with smaller interparticle separation; (III) RHCP structure formed above the template.

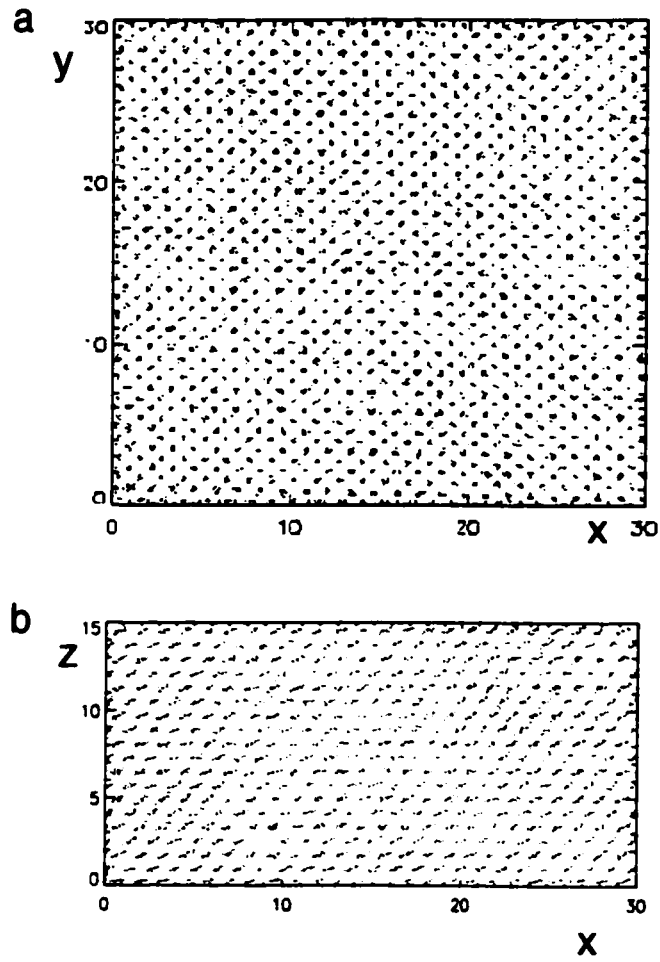


Figure 5.14: The positions of all the particles of a crystal at stage I projecting onto xy and xz plane. Particles from different layers are commensurate with each other well.

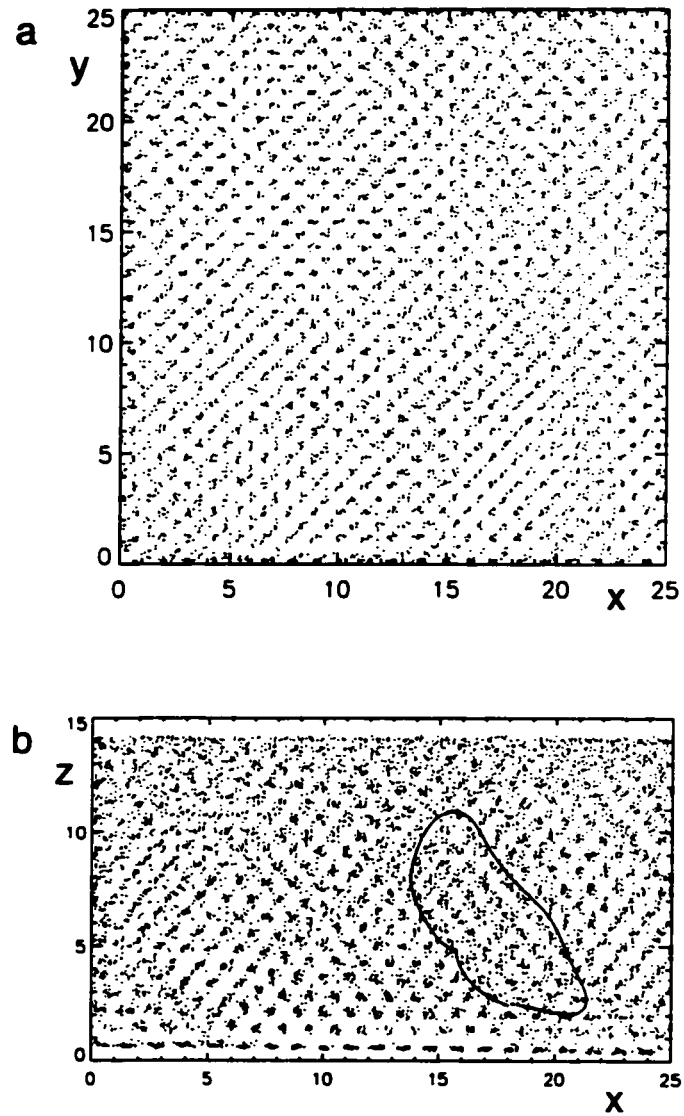


Figure 5.15: The positions of all particles of a crystal at stage II projecting onto the xy plane and in the xz plane. In (b) the particle positions have slight shift from original lattice because dislocation line in Fig. . The circled region showed the positions off from the commensurate lattice.

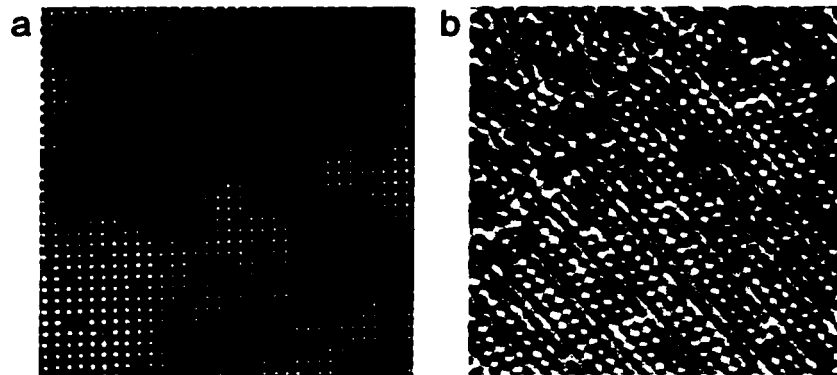


Figure 5.16: (a) silica particles nucleate on a BCC template for the first layer. (b) silica particles packed in hexagonal structure at higher layer.

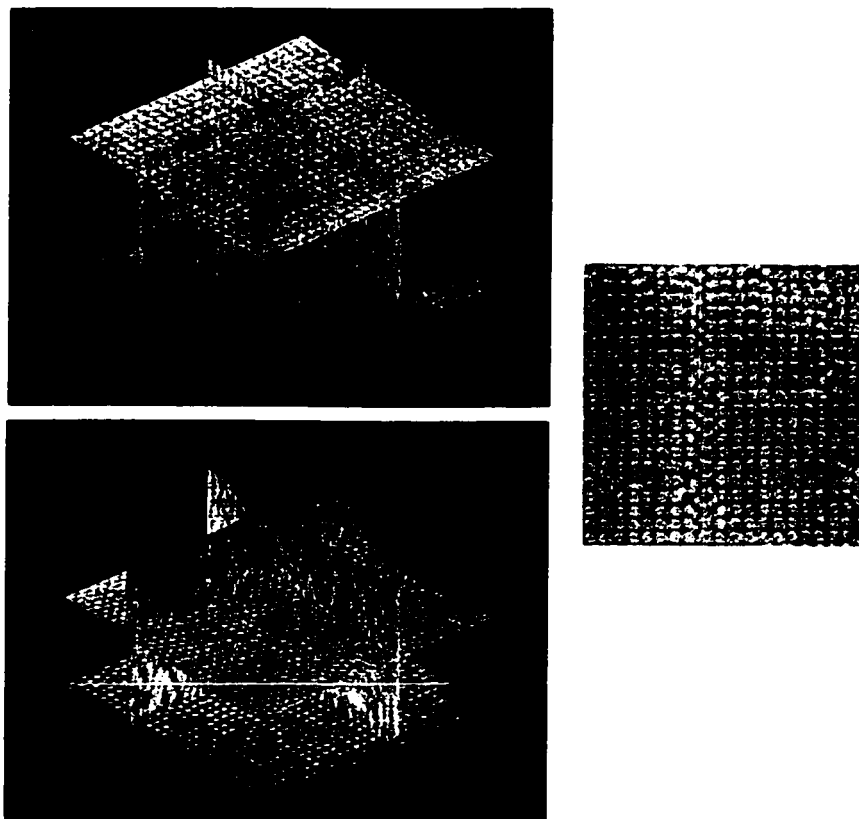


Figure 5.17: Experimental data for three different stages.

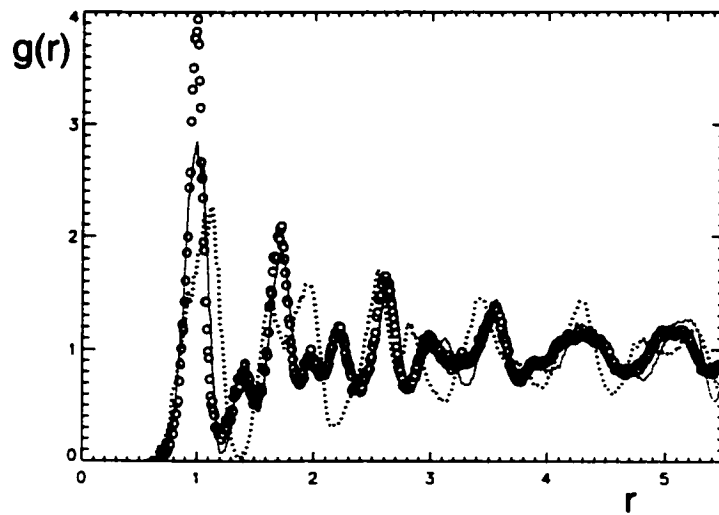


Figure 5.18: The correlation function of the BCC-like crystal compared with simulated FCC and BCC crystals.

Chapter 6

Conclusion and Future Work

In this thesis we have focused on the entropic effects in colloidal suspension. In particular we have measured the interaction between colloidal spheres in rod suspensions and observed phases of colloidal spheres on patterned surfaces.

The measurements of depletion interactions between spheres in rod-like molecule suspensions have demonstrated the strong geometric dependence of entropic interactions. The experiments are the first direct measurements of these effects. We have verified YJM theory in non-Derjaguin regime. When the sphere diameter is comparable to the rod length, the magnitude rod depletion interaction is reduced significantly from the model calculated based on Derjaguin approximation. We also saw clearly that the rod-induced depletion potential is distinct from sphere-induced depletion potential both in magnitude and in shape. The attraction energy $\sim 1 k_B T$ between $1 \mu\text{m}$ spheres can be induced by thin rods at $\sim 0.01\%$ volume fraction while require volume fraction of spheres at $\sim 3\%$. We found further that flexibility of the

rods modified the interaction potentials from the rigid rod depletion potentials. We constructed few modified models to explain the subtle but non-negligible discrepancy between data and YJM theory. We were able to attribute the short range discrepancy to the extra axial rotational degrees of freedom of bent rods. We compared the data to the bent rod theory developed by Lau [29] which accounts for the extra short range effect. The YJM-L model provides excellent agreement with experimental data and results in a surprising conclusion that the persistence length of fd virus is two or three times smaller than the commonly known value of $2.2 \mu\text{m}$. In addition to testing the depletion interaction theory, this measurement can provide a new route to determine the persistence length of rod-like molecules.

The unexplained repulsion and bridging interactions due to fd sticking on the spheres are intriguing. If we can control the sticking process, the origins of interaction can be better explored and explained. From the repulsion measurement, we can understand steric interaction due to rod-like molecules. From the bridging measurement, we may also use it to measure the bending rigidity.

The assembly experiments demonstrated that the combination of grating templates with colloid/polymer mixtures provides rich and intriguing systems to investigate physics in different dimensionality. The 1D fluid on the groove may be engineered into channels. The ordered liquid structures on line gratings may be annealed into 2D solid. It is unknown whether 2D systems with the attractive potentials exhibit the

induced freezing by 1D periodic potential. Fundamentally this is an interesting question. If annealing can be achieved, it can be a versatile template with quasi-long-range order. Can we grow 3D crystal on such a template? Will it exhibit quasi-long-range order? One-dimensional periodic structures are more easily engineered or found in nature at smaller length scale. For example, lithography nowadays can achieve nm resolution. Co-polymer or lipids can also self-assemble into ripple phase of nm periodicity. These provide templates for nano-particles such as quantum dots or proteins. The preliminary work done by A. Michelman achieved annealing by applying magnetic field with dilute ferrofluid in solutions. The peaks of structure function appear sharper with time which means that more ordered structures are formed.

We observed particles sedimented onto FCC(100) templates of lattice spacing $d = 1.15\sigma$ (σ is the hard sphere diameter). The crystal formed at $\sim 50\%$ volume fraction, lower than the bulk freezing point 54.5%. As the osmotic pressure near the template increased, we observed commensurate-incommensurate transitions on the patterned substrate. The systems are not in true equilibrium however which makes it difficult to measure system's pressure equation of state. Our data showed that the equilibrium phases mainly depend on the osmotic pressure. Experiments to investigate the dependence should have density-matched samples with different volume fractions around the liquid-bulk transition point. There are many interesting questions to address: First, the surface-induced freezing point and the critical

height of freezing layers is a function of lattice spacing. Second, the commensurate-incommensurate transitions is a function of osmotic pressure given a lattice spacing. How is the transition height changed with the osmotic pressure? How do the misfit location lines form and propagate? Third, what is the nature of the interface between bulk/fluid? Is it rough or smooth? Is there a roughening transition pressure Π_R in hard sphere systems? What is the nature of this transitions? How will gravity change the roughening? Fourth, how will the systems evolve differently by adding non-adsorbing polymers? Addressing these questions helps to understand the influence of patterned walls on bulk crystal growth. It provides key information for controlling crystal growth process which promises large single crystals. The template-directed crystals also allow the study of different crystal facet. More direct applications in technology and interesting scientific questions will be opened up by single colloidal crystals.

Colloidal systems have been compared to atomic systems. Bulk phases of colloidal systems such as gel, glass, or phase transitions have been studied a lot. Yet there are many interesting phenomena on the surface or at the interface. Combinations of patterned surfaces with colloidal systems can be compared to surface science which is a rich and important discipline in atomic science. We have already addressed many interesting and specific questions for equilibrium behaviors. In the following we would like raise more open possibilities from surface science.

One main focus in surface science is to study crystal growth. Crystals can be grown from a solution, from the melt, from the vapour, and under ultra-high vacuum with techniques like molecular beam epitaxy (MBE) [6] and the growth depends on many parameters: wetting between substrate-adsorbate, commensurability, interparticle interaction, temperature, and volume fraction in the bulk. There are few different types of heterogrowth. For example, when lead is deposited on graphite (Fig. 6.1a), it forms droplet-like structures such as water droplets on a frying pan. This is called the Volmer-Weber (VW) type of growth. In the other limit, rare gases adsorbed on graphite form monolayers, and eventually well-spread multilayers. The xenon equilibrium coverage is a step function of the pressure or of the chemical potential. This is called Frank-van der Merwe (FM) mode growth. One often observes an intermediate type of growth, called Stranski-Krastanov (SK) mode (Fig. 6.1b). The adsorbate grows layer-by-layer for a while, then it forms droplets, as in VW. We observed both FM and VW-like of crystal growth mode on different flat substrate due to the wetting of colloids to the substrate (See Fig. 6.1c and d). The theory of growth from dense phases is complex which takes into account of mass and energy transport and hydrodynamics. The capability of real-time observation on colloidal systems in dense phases may bring new information into this field, such as as determining the scaling exponents of kinetic roughening [81].

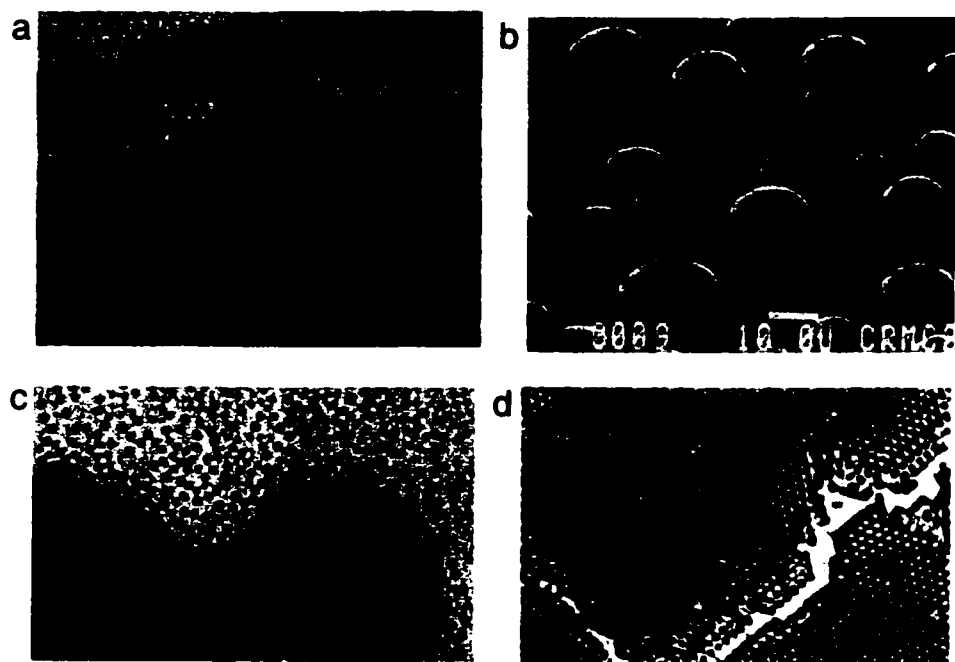


Figure 6.1: (a) V-W type of growth (Pb on graphite). (b) SK type of growth (Pb on Ge(111)). (pictures reproduced from [6]) (c) VW type of growth in colloidal solutions on optical glue. (d) FM type of growth in colloidal solution on clean glass.

Appendix A

Wormlike Chain Model

A central quantity to describe the conformations of a single polymer chain is the distribution function $G(\mathbf{r}; L)$ of the end-to-end distance \mathbf{r} for given contour length L and persistence length ℓ_p which is the characteristic length describing the decay of tangent-tangent correlations. $G(\mathbf{r}; L)$ represents the probability density of finding any two monomers at relative position $\mathbf{r} = \mathbf{r}(s) - \mathbf{r}(s')$ where $L = |s - s'|$ is the distance between the monomers along the chain. For a very flexible polymer ($L \gg \ell_p$) $G(\mathbf{r}; L)$ is described as a free-jointed chain. The physical properties of such polymers is dominated by the large number of chains (thus entropy $k_B T$ and well approximated by a simple Gaussian [149]. For a semiflexible polymer ($L \sim \ell_p$) the bending elastic energy between chains is comparable to the thermal energy $k_B T$ and thus the energetic suppression of configurations available to the chains should be considered. The corresponding model is the wormlike chain (WLC) model introduced Kratky and Porod in 1949 [150] who solved the exact expression for second moment of $\langle R^2 \rangle$. The

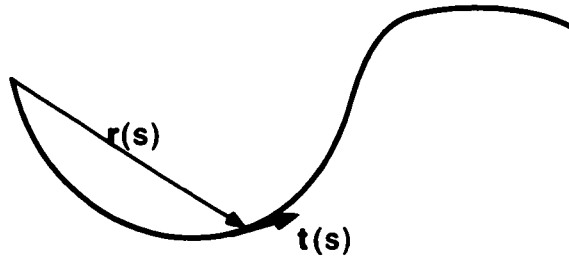


Figure A.1: $\mathbf{r}(s)$ is the position of a point on the curve and $\mathbf{t}(s)$ is a unit tangent vector at point $\mathbf{r}(s)$.

analytical expression $G(\mathbf{r}; L)$ of WLC is solved by Wilhelm and Frey in 1996 [128].

In the wormlike chain model the polymer is represented by a differentiable space curve $\mathbf{r}(s)$ of length L parametrized by arc-length s shown in Fig. A.1. Its statistical properties are determined by an effective free energy:

$$E = \frac{\kappa}{2} \int_0^L ds \left[\frac{\partial \mathbf{t}(s)}{\partial s} \right]^2. \quad (\text{A.1})$$

where $\mathbf{t}(s) = \partial \mathbf{r}(s) / \partial s$ is a unit vector tangent to the chain and κ is the bending force constant with the unit [energy]/[length]. The configurational partition function $Z(\mathbf{t}, s)$ of the polymer is thus given by Boltzmann distribution for this energy:

$$Z(\mathbf{t}, s) = \int d\{\mathbf{t}\} \exp \left[-\frac{\kappa}{2} \int_0^L ds \left(\frac{\partial \mathbf{t}}{\partial s} \right)^2 \right] \quad (\text{A.2})$$

where the integration over all possible configurations of the chains. Actually this partition function A.2 have the same form of the path integral for a free particle.

Therefore, Z readily satisfies a free particles Schrödinger-like equation:

$$\frac{\partial Z}{\partial s} = \lambda \nabla_t^2 Z \quad (\text{A.3})$$

with $\lambda = k_B T / 2\kappa$.

The inextensibility of the chain is expressed by the local constraint $|\mathbf{t}(s)|^2 = 1$.

This translates the free particle diffusing on a unit sphere; thus Z satisfies:

$$\frac{\partial Z}{\partial s} = \lambda \hat{\mathbf{L}}^2 Z \quad (\text{A.4})$$

where $\hat{\mathbf{L}}$ is the angular momentum.

The quantity we are interested is:

$$\langle [r(L) - r(0)]^2 \rangle = \int_0^L ds \int_0^L ds' \langle \mathbf{t}(s) \cdot \mathbf{t}(s') \rangle. \quad (\text{A.5})$$

But $\langle \mathbf{t}(s) \cdot \mathbf{t}(s') \rangle = \langle \mathbf{t}(s - s') \cdot \mathbf{t}(0) \rangle = \langle \cos \theta(s - s') \rangle$. If we fix one end of the filament defined as z-axis, the free end is described by angle θ and ϕ . The tangent vector correlation function $\langle \mathbf{t}(s) \cdot \mathbf{t}(0) \rangle = \langle \cos \theta \rangle$ can be calculated:

$$\begin{aligned} \langle \cos \theta(s) \rangle &= \frac{\int_{-1}^1 d(\cos \theta) \cos \theta Z(\cos \theta, s)}{\int_{-1}^1 d(\cos \theta) Z(\cos \theta, s)} \\ \frac{d\langle \cos \theta(s) \rangle}{ds} &= \frac{\int_{-1}^1 d(\cos \theta) \cos \theta \lambda \hat{\mathbf{L}}^2 Z(\cos \theta, s)}{\int_{-1}^1 d(\cos \theta) Z(\cos \theta, s)}. \end{aligned} \quad (\text{A.6})$$

Because $\hat{\mathbf{L}}^2$ is a Hermitian operator, $\hat{\mathbf{L}}^2 \cos \theta = (D - 1) \cos \theta$, where D is the dimensionality of space. Therefore in 3D,

$$\langle \cos \theta(s) \rangle = e^{-2\lambda |s|} \quad (\text{A.7})$$

and the persistence length $\ell_p = \frac{1}{2\lambda}$. The mean squared end-to-end separation can be calculated as follows:

$$\begin{aligned}
 \langle [r(L) - r(0)]^2 \rangle &= \int_0^L ds \int_0^L ds' \langle \cos(\theta(s)) - \cos \theta(s') \rangle \\
 &= \int_0^L ds \int_0^L ds' e^{-|s-s'|/\ell_p} \\
 &= \int_0^L ds \left[\int_0^s ds' e^{-(s-s')/\ell_p} + \int_s^L ds' e^{-(s'-s)/\ell_p} \right] \\
 &= 2L\ell_p + 2\ell_p^2 (e^{-L/\ell_p} - 1) \tag{A.8}
 \end{aligned}$$

The two limiting cases are: (i) $L \gg \ell_p$ (the random coil limit), $\langle R^2 \rangle = L\ell_p/2$.
(ii) $\ell_p \gg L$ (the rigid rod limit), $\langle R^2 \rangle = L^2$.

Bibliography

- [1] K.-H. Lin, J. C. Crocker, A. C. Zeri, and A. G. Yodh, *Colloidal Interactions in Suspensions of Rods*, Phys. Rev. Lett. **87**, 088301 (2001).
- [2] M. Heni, *Surface Induced Effects in Hard Sphere Systems*, Ph.D. thesis, der Heinrich-Heine-Universität, 2001.
- [3] J. W. B. K. Kay and J. McCafferty, *Phage Display of Peptides and Proteins* (Academic Press, London, 1996).
- [4] S. M. Ilett, A. Orrock, W. C. K. Poon, and P. N. Pusey, *Phase behavior of a model colloid-polymer mixture*, Phys. Rev. E **51**, 1344 (1995).
- [5] A. D. Dinsmore, P. B. Warren, W. C. K. Poon, and A. G. Yodh, *Fluid-solid Transitions on Walls in Binary Hard-sphere Mixtures*. Europhysics Lett. **40**, 337 (1997).
- [6] A. Pimpinelli and J. Villain, *Physics of Crystal Growth* (Cambridge University Press, New York, 1998).
- [7] B. V. Derjaguin and L. Landau, , Acta Physicochimica **14**, 1941 (1941).

- [8] *Theory of the Stability of Lyophobic Colloids*, edited by E. J. Verwey and J. T. G. Overbeek (Elsevier, Amsterdam, 1948).
- [9] D. Frenkel, *Entropy-Driven Phase Transitions*, *Physica A* **263**, 26 (1999).
- [10] M. Adams, Z. Dogic, S. Keller, and S. Fraden, *Entropically driven microphase transitions in mixtures of colloidal rods and spheres*, *Nature* **393**, 349 (1998).
- [11] S. Asakura and F. Oosawa, *On Interaction Between Two Bodies Immersed in a Solution of Macromolecules*, *J. Chem. Phys.* **22**, 1255 (1954).
- [12] A. Vrij, *Polymers at Interfaces and the Interactions in Colloidal Suspensions*, *Pure and Applied Chem.* **48**, 471 (1976).
- [13] J. M. Kosterlitz and D. J. Thouless, *Ordering, Metastability and Phase Transitions in Two-Dimensional Systems*, *J. Phys. C.: Solid State Phys.* **6**, 1181 (1973).
- [14] B. I. Halperin and D. R. Nelson, *Theory of Two-Dimensional Melting*, *Phys. Rev. Lett.* **41**, 121 (1978).
- [15] D. R. Nelson and B. I. Halperin, *Dislocation-Mediated Melting in Two Dimensions*, *Phys. Rev. B* **19**, 2457 (1979).
- [16] A. P. Young, *Melting and the Vector Coulomb Gas in Two Dimensions*, *Phys. Rev. B* **19**, 1855 (1979).

- [17] M. Heni and H. Löwen, *Surface Freezing on Patterned Substrates*, Phys. Rev. Lett. **85**, 3668 (2000).
- [18] S. Asakura and F. Oosawa, *Interaction between Particles Suspended in Solutions of Macromolecules*, J. Polymer Sci. **33**, 183 (1958).
- [19] L. Auvray, *Solutions of Rigid Macromolecules - Wall and Confinement Effects - Orientation By Flow*, J. Phys. (Paris) **42**, 79 (1981).
- [20] Y. Mao, M. E. Cates, and H. N. W. Lekkerkerker, *Theory of the depletion force due to rodlike polymers*, J. Chem. Phys. **106**, 3712 (1997).
- [21] K. Yaman, C. Jeppesen, and C. M. Marques, *Depletion forces between two spheres in a rod solution*, Europhys. Lett. **42**, 221 (1998).
- [22] P. van der Schoot, *Depletion Interactions in Lyotropic Nematics*, J. Chem. Phys. **112**, 9132 (2000).
- [23] M. Piech and J. Y. Walz, *Depletion Interactions Produced by Nonadsorbing Charged and Uncharged Spheroids*, J. Colloid Interface Sci **232**, 86 (2000).
- [24] M. Triantafillou and R. D. Kamien, *Polymer Shape Anisotropy and the Depletion Interaction*, Phys. Rev. E. **59**, 5621 (1999).
- [25] G. A. Vliegenthart and H. N. W. Lekkerkerker, *Phase behavior of colloidal rod-sphere mixtures*, J. Chem. Phys. **111**, 4153 (1999).

- [26] Z. Dogic, D. Frenkel, and S. Fraden, *Enhanced Stability of Layered Phases in Parallel Hard Spherocylinders due to Addition of Hard Spheres*, Phys. Rev. E. **62**, 3925 (2000).
- [27] S. A. Safran, *Statistical Thermodynamics of Surfaces, Interfaces, and Membranes* (Addison-Wesley, New York, 1994).
- [28] M. A. Tracy, J. L. Garcia, and R. Pecora, *An Investigation of the Microstructure of a Rod/Sphere Composite Liquid*, Macromolecules **26**, 1862 (1993).
- [29] A. W. C. Lau, K.-H. Lin, and A. G. Yodh, *Entropic Interaction in Suspension of Semi-Flexible Rods: Short-Range Effects of Flexibility*, Phys. Rev. E Submitted (2002).
- [30] W. B. Russel, D. A. Saville, and W. R. Schowalter, *Colloidal Dispersions* (Marcel Dekker, New York, 1997).
- [31] J. P. Hansen and I. R. McDonald, *Theory of Simple Liquids* (Academic Press, London, 1986).
- [32] R. Zallen, *The Physics of Amorphous Solids* (Wiley, New York, 1983).
- [33] B. J. Alder and T. E. Wainwright, *Studies in Molecular Dynamics I. General Method*, J. Chem. Phys. **31**, 459 (1959).

- [34] W. Hoover and F. Ree, *Melting Transition and Communal Entropy for Hard Spheres*, *J. Chem. Phys.* **49**, 3609 (1968).
- [35] H. Reiss and A. D. Hammerich, *Hard Spheres: Scaled Particle Theory and Exact Relations on the Existence and Structure of the Fluid/Solid Transition*, *J. Phys. Chem.* **90**, 6252 (1986).
- [36] S. Hachisu and K. Takano, *Pressure of Disorder to Order Transition in Monodisperse Latex*, *Adv. Colloid Interface Sci.* **16**, 233 (1982).
- [37] P. N. Pusey and W. van Megan, *Phase-Behavior of Concentrated Suspensions of Nearly Hard Colloidal Spheres*, *Nature* **320**, 340 (1986).
- [38] N. F. Carnahan and K. E. Starling, *Equation of State for Nonattractive Rigid Spheres*, *J. Chem. Phys.* **51**, 635 (1969).
- [39] I. Livsey and R. H. Ottewill, *A Light-Scattering Study of Concentrated Dispersions in Nonaqueous Media*, *Colloid and Polymer Science* **267**, 421 (1989).
- [40] M. A. Rutgers, J. H. Dunsmuir, J.-Z. Xue, W. B. Russel, and P. M. Chaiken, *Measurement of the Hard-Sphere Equation of State Using Screened Charged Polystyrene Colloids*, *Phys. Rev. B* **53**, 5043 (1996).
- [41] C. G. D. Kruif, P. W. Rouw, W. J. Briels, M. H. G. Duits, A. Vrij, and R. P. May,

Adhesive Hard-Sphere Colloidal Dispersions - A Small-Angle Neutron Scattering Study of Stickiness and the Structure Factor, Langmuir **5**, 422 (1989).

- [42] R. Piazza, T. Bellini, and V. Degiorgio, *Equilibrium Sedimentation Profiles of Screened Charged Colloids: A Test of Hard-Sphere Equation of State*. Phys. Rev. Lett. **71**, 4267 (1993).
- [43] S.-E. Phan, W. B. Russel, Z. Cheng, J. Zhu, P. M. Chaikin, J. H. Dunsmuir, and R. H. Ottewill, *Phase Transitions Equation, of State and Limiting Shear Viscosities of Hard Sphere Dispersions*, Phys. Rev. E **54**, 6633 (1996).
- [44] A. P. Gast, W. B. Russel, and C. K. Hall, *Polymer-Induced Phase Separations in Nonaqueous Colloidal Suspensions*, J. Colloid Interface Sci. **109**, 161 (1986).
- [45] A. J. Fillery-Travis, P. A. Gunning, D. J. Hibberd, and M. M. Robins, *Coexistent Phases in Concentrated Polydisperse Emulsions Flocculated by Nonadsorbing Polymer*, J. Colloid Interface Sci. **159**, 189 (1993).
- [46] H. de Hek and A. Vrij, *Preparation of Sterically Stabilized Silica Dispersions in Non-aqueous Media*, J. Colloid Interface Sci. **79**, 289 (1981).
- [47] P. R. Sperry, *Morphology and Mechanism in Latex Flocculated by Volume Restriction*, J. Colloid Interface Sci. **99**, 97 (1984).
- [48] C. Smits, B. Vandermost, J. K. G. Dhont, and H. N. W. Lekkerkerker, *Influence*

- of Nonadsorbing Polymer on the Formation of Colloidal Crystals*, Adv. Colloid Interface Sci. **42**, 33 (1992).
- [49] F. L. Calderon, J. Bibette, and J. Biais, *Experimental Phase-Diagrams of Polymer and Colloid Mixtures*, Europhys. Lett. **23**, 653 (1993).
- [50] A. P. Gast, C. K. Hall, and W. B. Russel, *Polymer-Induced Phase Separations in Nonaqueous Colloidal Suspensions*, J. Colloid Interface Sci. **96**, 251 (1983).
- [51] H. N. W. Lekkerkerker, W. C. K. Poon, P. N. Pusey, A. Stroobants, and P. B. Warren, *Phase Behaviour of Colloid + Polymer Mixtures*, Europhys. Lett. **20**, 559 (1992).
- [52] D. J. Robinson and J. C. Earnshaw, *Long Range Order in Two Dimensional Fractal Aggregation*, Phys. Rev. Lett. **71**, 715 (1993).
- [53] W. C. K. Poon and M. D. Haw, *Mesoscopic Structure Formation in Colloidal Aggregation and Gelation*, Adv. Colloid Interface Sci. **73**, 71 (1997).
- [54] W. C. K. Poon, A. D. Pirie, M. D. Haw, and P. N. Pusey, *Non-equilibrium Behavior of Colloid-Polymer Mixtures*, Physica A **235**, 110 (1997).
- [55] W. C. K. Poon, F. Renth, R. M. L. Evans, D. J. Fairhurst, M. E. Cates, and P. N. Pusey, *Colloid-Polymer Mixtures at Triple Coexistence: Kinetic Maps from Free-Energy Landscapes*, Phys. Rev. Lett. **83**, 1242 (1999).

- [56] N. A. M. Verhaegh, D. Asnaghi, H. N. W. Lekkerkerker, M. Giglio, and L. Cipelletti, *Transient Gelation by Spinodal Decomposition in Colloid-Polymer Mixtures*, *Physica A* **242**, 104 (1997).
- [57] M. Carpineti and M. Giglio, *Spinodal-type dynamics in fractal aggregation of colloidal clusters*, *Phys. Rev. Lett.* **68**, 3327 (1992).
- [58] E. H. A. de Hoog, W. K. Kegel, A. van Blaaderen, and H. N. W. Lekkerkerker, *Direct observation of crystallization and aggregation in a phase-separating colloid-polymer suspension*, *Phys. Rev. E* **64**, 021407 (2001).
- [59] P. N. Segr, V. Prasad, A. B. Schofield, and D. A. Weitz, *Glasslike Kinetic Arrest at the Colloidal-Gelation Transition*, *Phys. Rev. Lett.* **86**, 6042 (2001).
- [60] D. G. Grier and C. A. Murray, *The Microscopic Dynamics of Freezing in Supercooled Colloidal Fluids*, *J. Chem. Phys.* **100**, 9088 (1994).
- [61] D. A. McQuarrie, *Statistical Mechanics* (Harper & Row, New York, 1976).
- [62] W. H. Press, S. A. Teukolsky, W. T. Vetterling, and B. P. Flannery, *Numerical Recipes in C* (Cambridge University Press, Cambridge, 1992).
- [63] P. J. Steinhardt, D. R. Nelson, and M. Ronchetti, *Bond-orientational Order in Liquids and Glasses*, *Phys. Rev. B* **28**, 784 (1983).

- [64] A. R. Kansal, T. M. Truskett, and S. Torquato, *Nonequilibrium Hard-disk Packings with Controlled Orientational Order*, J. of Chem. Phys. **113**, 4844 (2000).
- [65] U. Gasser, E. R. Weeks, A. Schofield, P. N. Pusey, and D. A. Weitz, *Real Space Imaging of Nucleation and Growth In Colloidal Crystallization*. Science **292**, 258 (2001).
- [66] A. H. Marcus and S. A. Rice, *Observations of First-Order Liquid-to-Hexatic and Hexatic-to-Solid Phase Transitions in a Confined Colloid Suspension*, Phys. Rev. Lett. **77**, 2577 (1996).
- [67] C. A. Murray and R. A. Wenk, *Microscopic Particle Motions and Topological Defects in Two-Dimensional Hexatics and Dense Fluids*, Phys. Rev. Lett. **62**, 1643 (1989).
- [68] C. A. Murray, W. O. Sprenger, and R. A. Wenk, *Comparison of Melting in Three and Two Dimensions: Microscopy of Colloidal Spheres*, Phys. Rev. B **42**, 688 (1990).
- [69] A. Chowdhury, B. Ackerson, and N. Clark, *Laser-Induced Freezing*. Phys. Rev. Lett. **55**, 833 (1985).
- [70] Q.-H. Wei, C. Bechinger, D. Rudhardt, and P. Leiderer, *Experimental Study of Laser-Induced Melting in Two-Dimensional Colloids*, Phys. Rev. Lett. **81**, 2606 (1998).

- [71] J. Chakrabarti, H. R. Krishnamurthy, and A. K. Sood, *Density Functional Theory of Laser-Induced Freezing in Colloidal Suspensions*, Phys. Rev. Lett. **73**, 2923 (1994).
- [72] J. Chakrabarti, H. R. Krishnamurthy, A. K. Sood, and S. Sengupta, *Reentrant Melting in Laser Field Modulated Colloidal Suspensions*, Phys. Rev. Lett. **75**, 2232 (1995).
- [73] C. Das and H. R. Krishnamurthy, *Laser-Induced Quasicrystalline Order in Charge-Stabilized Colloidal Systems*, Phys. Rev. B **58**, R5889 (1998).
- [74] E. Frey, D. R. Nelson, and L. Radzihovsky, *Light Induced Melting of Colloidal Crystals in Two Dimensions*, Phys. Rev. Lett. **83**, 2977 (1999).
- [75] L. Radzihovsky, E. Frey, and D. Nelson, *Novel Phases and Reentrant Melting of Two-Dimensional Colloidal Crystals*, Phys. Rev. E **63**, 031503 (2001).
- [76] S. Dietrich, in *Phase Transitions and Critical Phenomena*, edited by C. Domb and J. L. Lebowitz (Academic Press, London, 1988), Vol. 12, Chap. 1.
- [77] R. L. Davidchack and B. B. Laird, *Direct Calculation of the Hard-Sphere Crystal/Melt Interfacial Free Energy*, Phys. Rev. Lett. **85**, 4751 (2000).
- [78] F. T. Gittes and M. Schick, *Complete and Incomplete Wetting by Adsorbed Solids*, Phys. Rev. B **30**, 209 (1984).

- [79] D. Frenkel and A. J. C. Ladd, *Elastic Constants of Hard-Sphere Crystals*, Phys. Rev. Lett. **95**, 1169 (1987).
- [80] R. Ohnesorge, H. Löwen, and H. Wagner, *Density Functional Theory of Crystal-Fluid Interfaces and Surface Melting*, Phys. Rev. E **50**, 4801 (1994).
- [81] R. C. Salvarezza, L. Vázquez, H. Míguez, R. Mayoral, C. López, and F. Meseguer, *Edward-Wilkinson Behavior of Crystal Surface Grown By Sedimentation of SiO₂ Nanospheres*, Phys. Rev. Lett. **77**, 4572 (1996).
- [82] M. Bernasconi and E. Tosatti, *Reconstruction, Disordering and Roughening of Metal Surfaces*, Surf. Sci. Rep. **17**, 1993 (1993).
- [83] P. N. Pusey, in *Liquids, Freezing and Glass Transition*, edited by J. P. Hansen, D. Levesque, and J. Zinn-Justin (Elsevier, Amsterdam, 1991). Chap. 10.
- [84] A. van Blaaderen and A. Vrij, *Synthesis and Characterization of Colloidal Dispersions of Fluorescent Monodisperse Silica Spheres*, Langmuir **8**, 2921 (1992).
- [85] *Dispersion Polymerization in Organic Media*, edited by K. E. J. Barrett (Wiley, London, 1975).
- [86] L. Antl, *The Preparation of Poly(Methyl Methacrylate) Lattices In Nonaqueous Media*, Colloids Surf. **17**, 67 (1986).

- [87] R. H. Ottewill and I. Livsey, *The Imbibition of Carbon-Disulfide By Poly(Methyl Methacrylate) Latex-particles*, *Polymer* **28**, 109 (1987).
- [88] E. H. A. de Hoog, *Interfaces and Crystallization of Colloid-Polymer Suspensions*. Ph.D. thesis, Universiteit Utrecht, 2001.
- [89] P. Pieranski, L. Strzelecki, and B. Pansu, *Thin Colloidal Crystals*, *Phys. Rev. Lett.* **50**, 900 (1983).
- [90] P. Bartlett, R. H. Ottewill, and P. N. Pusey, *Superlattice Formation in Binary Mixtures of Hard-sphere Colloids*, *Phys. Rev. Lett.* **68**, 3801 (1992).
- [91] A. P. Gast and W. B. Russel, *Simple Ordering in Complex Fluids*, *Physics Today* **51**, 24 (1998).
- [92] P. N. Pusey, W. van Meegen, P. Bartlett, B. J. Ackerson, J. G. Rarity, and S. M. Underwood, *Structure of Crystals of Hard Colloidal Spheres*, *Phys. Rev. Lett.* **63**, 2753 (1989).
- [93] J. L. Harland, S. I. Henderson, S. M. Underwood, and W. van Meegen, *Observation of Accelerated Nucleation in Dense Colloidal Fluids of Hard Sphere Particles*, *Phys. Rev. Lett.* **75**, 3572 (1995).
- [94] K. Schätzel and B. J. Ackerson, *Observation of Density Fluctuations during Crystallization*, *Phys. Rev. Lett.* **68**, 337 (92).

- [95] S.-C. Mau and D. A. Huse, *Stacking Entropy of Hard-sphere Crystals*. Phys. Rev. E **59**, 4396 (1999).
- [96] A. van Blaaderen, R. Ruel, and P. Wiltzius, *Template-directed Colloidal Crystallization*, Nature **385**, 321 (1997).
- [97] R. Micheletto, H. Fukuda, and M. Ohtsu, *A Simple Method For the Production of a 2-Dimensional, Ordered Array of Small Latex-Particles*, Langmuir **11**, 3333 (1995).
- [98] N. D. Denkov, *2-Dimensional Crystallization*, Nature **361**, 26 (1993).
- [99] P. Kralchevsky and K. Nagayama, *Capillary Forces Between Colloidal Particles*. Langmuir **1**, 23 (1994).
- [100] P. Jiang, J. F. Bertone, K. S. Hwang, and V. L. Colvin, *Single-Crystal Colloidal Multilayers of Controlled Thickness*, Chem. Mater. **11**, 2132 (1999).
- [101] P. A. Kralchevsky and N. D. Denkov, *Capillary Forces and Structuring in Layers of Colloid Particles*. Curr. Opin. Colloid Interface Sci. **6**, 383 (2001).
- [102] M. Holgado, F. Garca-Santamara, A. Blanco, M. Ibisate, A. Cintas, H. Miguez, C. J. Serna, C. Molpeceres, J. Requena, A. Mifsud, F. Meseguer, and C. Lopez, *Electrophoretic Deposition To Control Artificial Opal Growth*, Langmuir **15**, 4701 (1999).

- [103] Y. Xia, E. Kim, X.-M. Zhao, J. A. Rogers, M. Prentiss, and G. M. Whitesides, *Complex Optical Surfaces Formed by Replica Molding Against Elastomeric Masters*, *Science* **273**, 347 (1996).
- [104] S. Chou, P. R. Krauss, W. Zhang, L. Guo, and L. Zhuang, *Sub-10 nm imprint lithography and applications*, *J. Vac. Sci. Technol. B.* **15**, 2897 (1997).
- [105] H.-P. Chou, *Microfabricated Devices for Rapid DNA Diagnostics*, Ph.D. thesis. California Institute of Technology, 2000.
- [106] A. Ashkin, J. M. Dziedzic, J. E. Bjorkholm, and S. Chu, *Observation of a Single-beam Gradient Force Optical Trap for Dielectric Particles*, *Optics Letters* **11**, 288 (1986).
- [107] M. D. Wang, H. Yin, R. Landick, J. Gelles, and S. M. Block, *Stretching DNA with Optical Tweezers*, *Biophysical Journal* **72**, 1335 (1997).
- [108] J. C. Crocker and D. G. Grier, *Microscopic Measurement of the Pair Interaction Potential of Charge-Stabilized Colloid*, *Physical Review Letters* **73**, 352 (1994).
- [109] J.-C. Meiners and S. R. Quake, *Femtonewton Force Spectroscopy of Single Extended DNA Molecules*, *Phys. Rev. Lett.* **84**, 5014 (2000).
- [110] K. Takamura, H. Goldsmith, and S. G. Mason, *The Microrheology of Colloidal*

- Dispersions: Trajectories of Orthokinetic Pair-Collisions of Latex Spheres in a Simple Electrolyte*, Journal of Colloid and Interface Science **82**, 175 (1981).
- [111] K. Vondermassen, J. Bongers, A. Mueller, and H. Versmold, *Brownian-Motion - A Tool to Determine The Pair Potential Between Colloid Particles*. Langmuir **10**, 1351 (1994).
- [112] G. M. Kepler and S. Fraden, *Attractive Potential Between Confined Colloids At Low Ionic-Strength*. Phys. Rev. Lett. **73**, 356 (1994).
- [113] J. C. Crocer and D. G. Grier, *Methods of Digital Video Microscopy for Colloidal Studies*. Journal of Colloid and Interface Science **179**, 298 (1996).
- [114] K. H. Lan, N. Ostrowsky, and D. Sornette, *Brownian Dynamics Close to a Wall Studied by Photon Correlation Spectroscopy From an Evanescent Wave*. Phys. Rev. Lett. **57**, 17 (1986).
- [115] D. Rudhardt, C. Bechinger, and P. Leiderer, *Direct Measurement of Depletion Potentials in Mixtures of Colloids and Nonionic Polymers*. Phys. Rev. Lett. **81**, 1330 (1998).
- [116] J. N. Israelachvili, *Intermolecular and Surface Forces* (Academic Press, New York, 1992).

- [117] W. A. Ducker, T. J. Senden, and R. M. Parshly, *Direct Measurement of Colloidal Forces Using an Atomic Force Microscope*, *Nature* **353**, 239 (1991).
- [118] T. R. Strick, J.-F. Allemand, D. Bensimon, A. Bensimon, and V. Croquette, *The Elasticity of a Single Supercoiled DNA molecule*, *Science* **271**, 1835 (1996).
- [119] P. Poulin, V. Cabuil, and D. A. Weitz, *Direct Measurement of Colloidal Forces in an Anisotropic Solvent*, *Phys. Rev. Lett.* **79**, 4862 (1997).
- [120] F. L. Calderon, T. Stora, O. M. Monval, P. Poulin, and J. Bibette, *Direct Measurement of Colloidal Forces*, *Phys. Rev. Lett.* **72**, 2858 (1994).
- [121] R. Verma, *Entropic Attractions in Colloid-Polymer Solutions*, Ph.D. thesis, University of Pennsylvania, 1999.
- [122] R. Verma, J. C. Crocker, T. C. Lubensky, and A. G. Yodh, *Attractions between Hard Colloidal Spheres in Semiflexible Polymer Solutions*, *Macromolecules* **33**, 177 (2000).
- [123] S. Fraden, in *Observation, Prediction, and Simulation of Phase Transitions in Complex Fluids*, edited by M. Baus, L. F. Rull, and J. P. Ryckaert (Kluwer Academic, Dordrecht, 1995), Chap. 10.
- [124] D. A. Marvin and H. Hoffmann-Berling, , *Z. Naturforschung* **18b**, 884 (1963).

- [125] L. A. Day, C. J. Marzec, S. A. Reisberg, and A. Casadevall, *DNA packing in Filamentous Bacteriophages*, *Ann. Rev. Biophys. Chem.* **17**, 509 (1988).
- [126] T. Maeda and S. Fujime, *Dynamic Light-Scattering Study of Suspensions of fd Virus. Application of a Theory of the Light-Scattering Spectrum of Weakly Bending Filaments*, *Macromolecules* **18**, 2430 (1985).
- [127] K. Beck and R. M. Duenki, *Flexibility of Bacteriophage M13: Comparison of Hydrodynamic Measurements with Electron Microscopy*, *J. of Struct. Biol.* **105**, 22 (1990).
- [128] J. Wilhelm and E. Frey, *Radial Distribution Function of Semiflexible Polymers*, *Phys. Rev. Lett.* **77**, 2581 (1996).
- [129] J. Newman, H. L. Swinney, and L. A. Day, *Hydrodynamic Properties and Structure of fd Virus*, *J. of Mol. Biol.* **116**, 593 (606).
- [130] L. Song, U. Kim, J. Wilcoxon, and M. Schurr, *Dynamic Light Scattering from Weakly Bending Rods: Estimation of the Dynamic Bending Rigidity of the M13 Virus*, *Biopolymers* **31**, 547 (1991).
- [131] M. Doi and S. F. Edwards, *The Theory of Polymer Dynamics* (Oxford, Oxford, 1986).

- [132] K. Kroy and E. Frey, *Dynamic Scattering from Solutions of Semiflexible Polymers*. Phys. Rev. E **55**, 3092 (1997).
- [133] T. B. Liverpool and A. C. Maggs, *Dynamic Scattering from Semiflexible Polymers*. Macromolecules **34**, 6064 (2001).
- [134] A. Augustin. *Dynamic Light Scattering Study of the Filamentous Phages fd and Pf1*, Ph.D. thesis, Technischen Universitat Munchen, 1999.
- [135] A. R. Khokhlov and A. N. Semenov, *Liquid-Crystalline Ordering in the Solution of Partially Flexible Macromolecules*, Physica A **112A**, 605 (1982).
- [136] Z.-Y. Chen, *Nematic Ordering in Semiflexible Polymer Chains*. Macromolecules **26**, 3419 (1993).
- [137] E. Loh, E. Ralston, and V. N. Schumaker, *Quasielastic Light Scattering from Solutions of Filamentous Viruses I. Experimental*, Biopolymers **18**, 2549 (1979).
- [138] Y. Mao, M. E. Cates, and H. N. W. Lekkerkerker, *Theory of the depletion force due to rodlike polymers*, Phys. Rev. Lett. **75**, 4548 (1995).
- [139] G. H. Koenderink, G. A. Vliegenthart, S. G. J. M. Kluijtmans, A. van Blaaderen, A. P. Philipse, and H. N. W. Lekkerkerker. *Depletion-Induced Crystallization in Colloidal Rod-Sphere Mixtures*, Langmuir **15**, 4693 (1999).

- [140] C. Bechinger, D. Rudhardt, P. Leiderer, R. Roth, and S. Dietrich, *Understanding Depletion Forces beyond Entropy*, Phys. Rev. Lett. **83**, 3960 (1999).
- [141] J. C. Crocker, J. A. Matteo, A. D. Dinsmore, and A. G. Yodh, *Entropic Attraction and Repulsion in Binary Colloids Probed with a Line Optical Tweezer*, Phys. Rev. Lett. **82**, 4352 (1999).
- [142] A. Dinsmore, A. G. Yodh, and D. J. Pine, *Phase Diagrams of nearly-hard-sphere binary colloids*, Phys. Rev. E. **52**, 4045 (1995).
- [143] P. D. Kaplan, J. L. Rourke, A. G. Yodh, and D. J. Pine, *Entropically driven Phase Separation in Binary Colloidal Mixtures*, Phys. Rev. Lett. **72**, 582 (1994).
- [144] A. D. Dinsmore and A. G. Yodh, *Entropic Confinement of Colloidal Spheres in Corners on Silicon Substrates*, Langmuir **15**, 314 (1999).
- [145] A. D. Dinsmore, A. G. Yodh, and D. J. Pine, *Entropic Control of Particle Motion Using Passive Surface Microstructures*, Nature **383**, 239 (1996).
- [146] A. D. Dinsmore, J. C. Crocker, and A. G. Yodh, *Self-assembly of Colloidal Crystals*. Curr. Opin. Colloid Interface Sci. **3**, 5 (1998).
- [147] E. Leib and D. Mattis, *Mathematical Physics in One Dimension* (Academic Press. New York, 1966).

- [148] M. Heni and H. Löwen, *Precrystallization of Fluids Induced by Patterned Substrates*, *J. Phys.:Cond. Mat.* **13**, 4675 (2001).
- [149] H. Yamakawa, *Modern Theory of Polymer Solutions* (Harper & Row, New York, 1971).
- [150] O. Kratky and G. Porod, *Röntgenuntersuchung Gelöster Fadenmoleküle*, *G. Recl. Trav. Chim.* **68**, 1106 (1949).